Supporting Information for

Privileged Metal Cluster Complexes

Shiquan Lin,[1,3#] Dan Li,[2#] Dandan Zhang,[2] Lijun Geng,[1] Yuhan Jia,[1] Weizhe Wang,[1] Longjiu Cheng,[2] Shiv N. Khanna,[4] and Zhixun Luo[1,3*]*

[1]Beijing National Laboratory for Molecular Sciences (BNLMS), State Key Laboratory for Structural Chemistry of Unstable and Stable Species, Institute of Chemistry, Chinese Academy of Sciences, Beijing, China 100190
[2]Department of Chemistry, Anhui University, Hefei, China 230601
[3]School of Chemistry, University of Chinese Academy of Sciences, Beijing, China 100049
[4]Department of Physics, Virginia Commonwealth University, Richmond, USA VA 23284-2000
*Correspondence: clj@ustc.edu (L.C.); zxluo@iccas.ac.cn (Z.L.).
[#]These authors contributed equally to this work.

Contents

S1. The reactions of $Pt_n^{\pm}$ with NO and CO

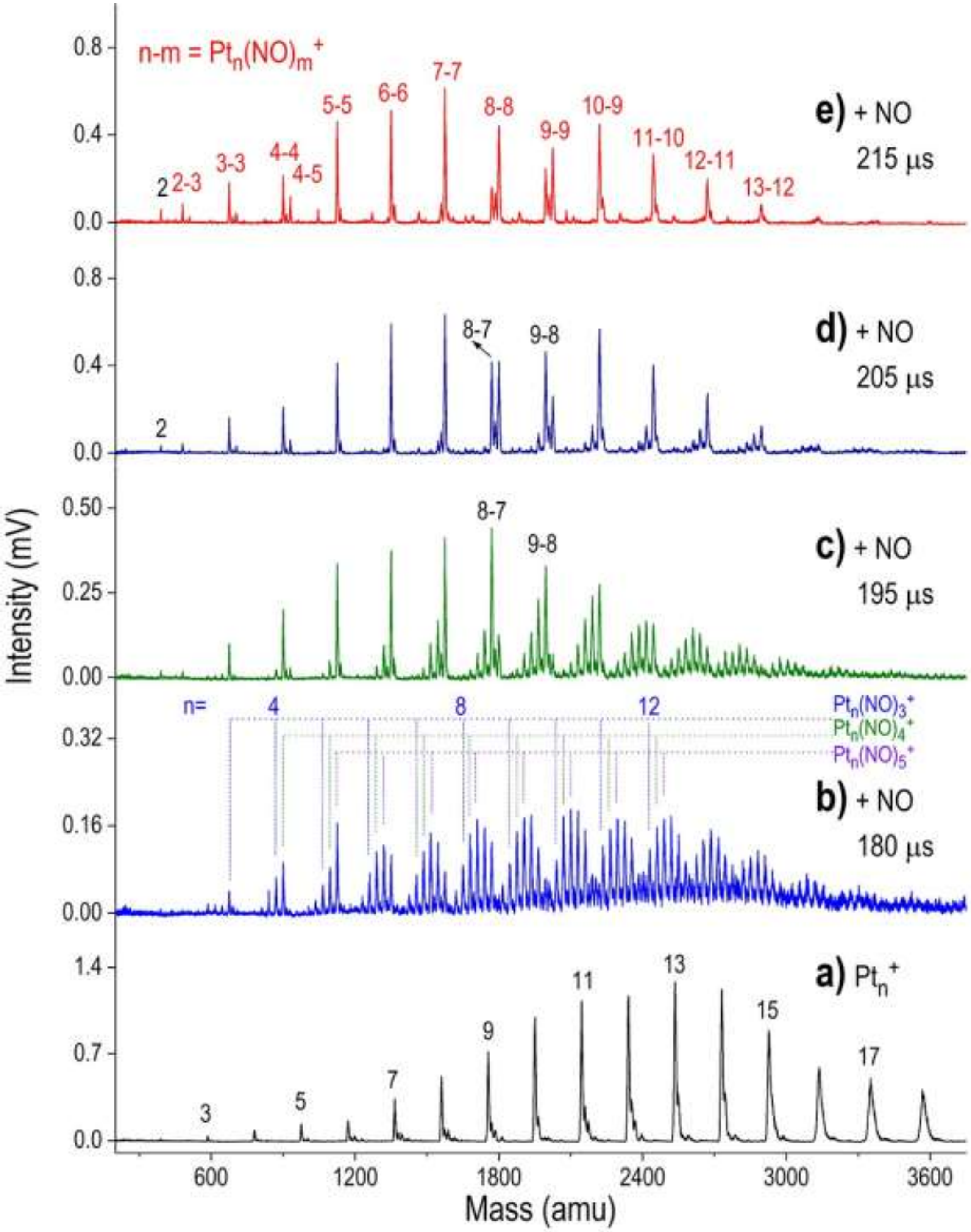

Fig. S1 Cationic Pt_n^+ clusters reacting with NO. Mass spectra of the nascent Pt_n^+ clusters (a) and after reaction with 5% NO/He (b−e), with different doses controlled by a 10-Hz pulsed valve.

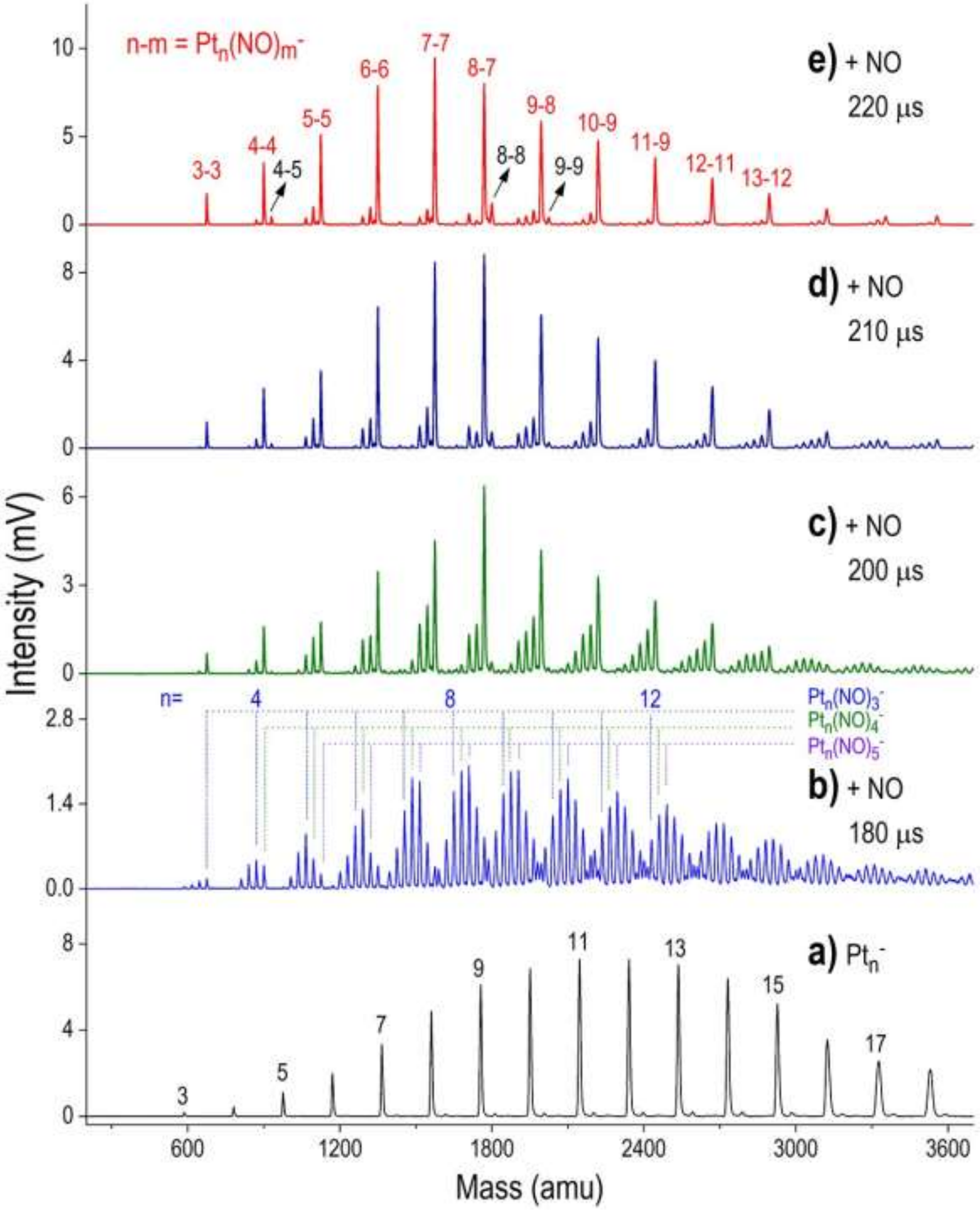

Fig. S2 Anionic Pt_n^- clusters reacting with NO. Mass spectra of the nascent Pt_n^- clusters (a) and after reaction with 5% NO/He (b−e) , with different doses controlled by a 10-Hz pulsed valve.

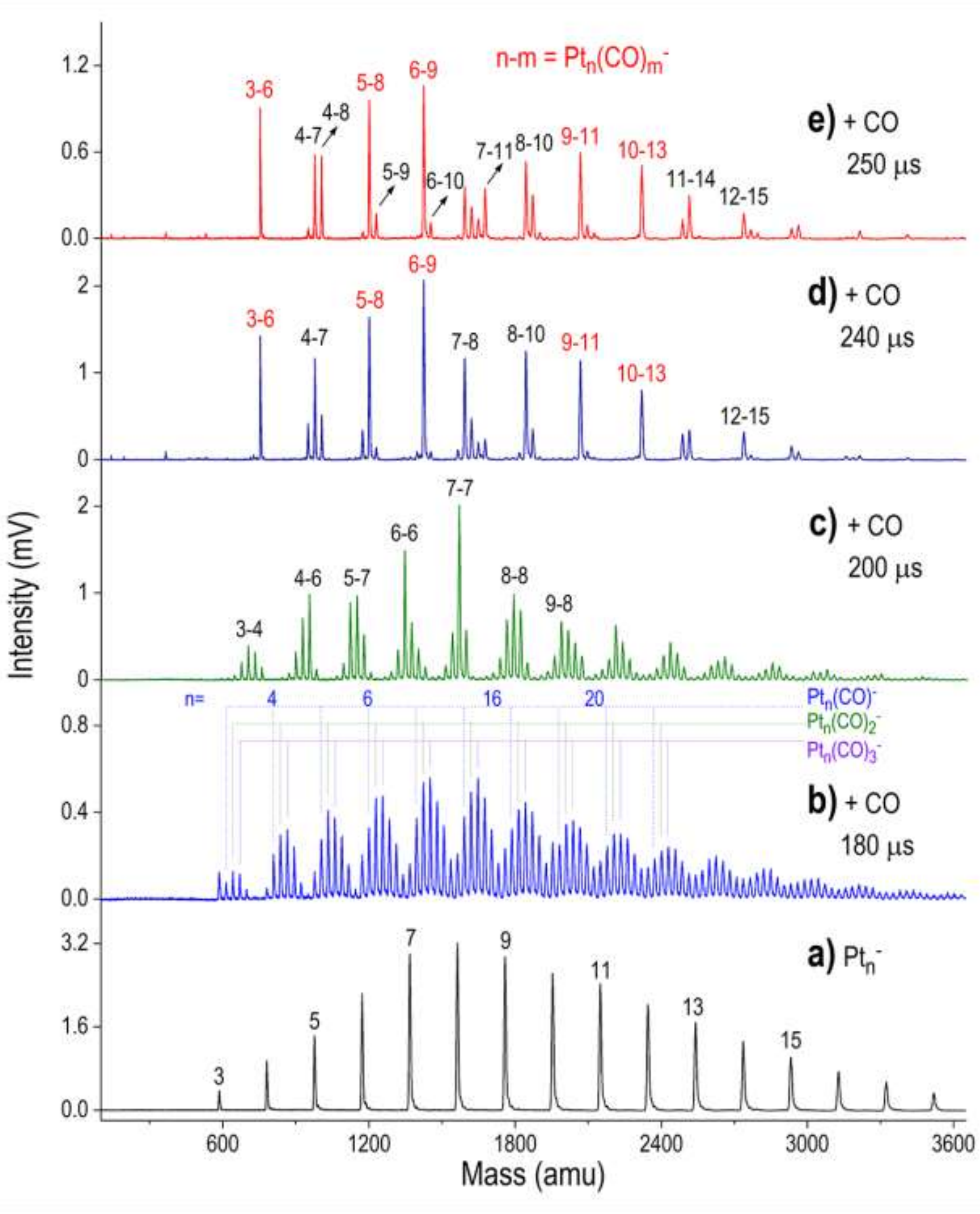

Fig. S3 Anionic Pt$_n^-$ clusters reacting with CO. Mass spectra of the nascent Pt$_n^-$ clusters (a) and after reaction with 15% CO/He (b−e), with different doses controlled by a 10-Hz pulsed valve.

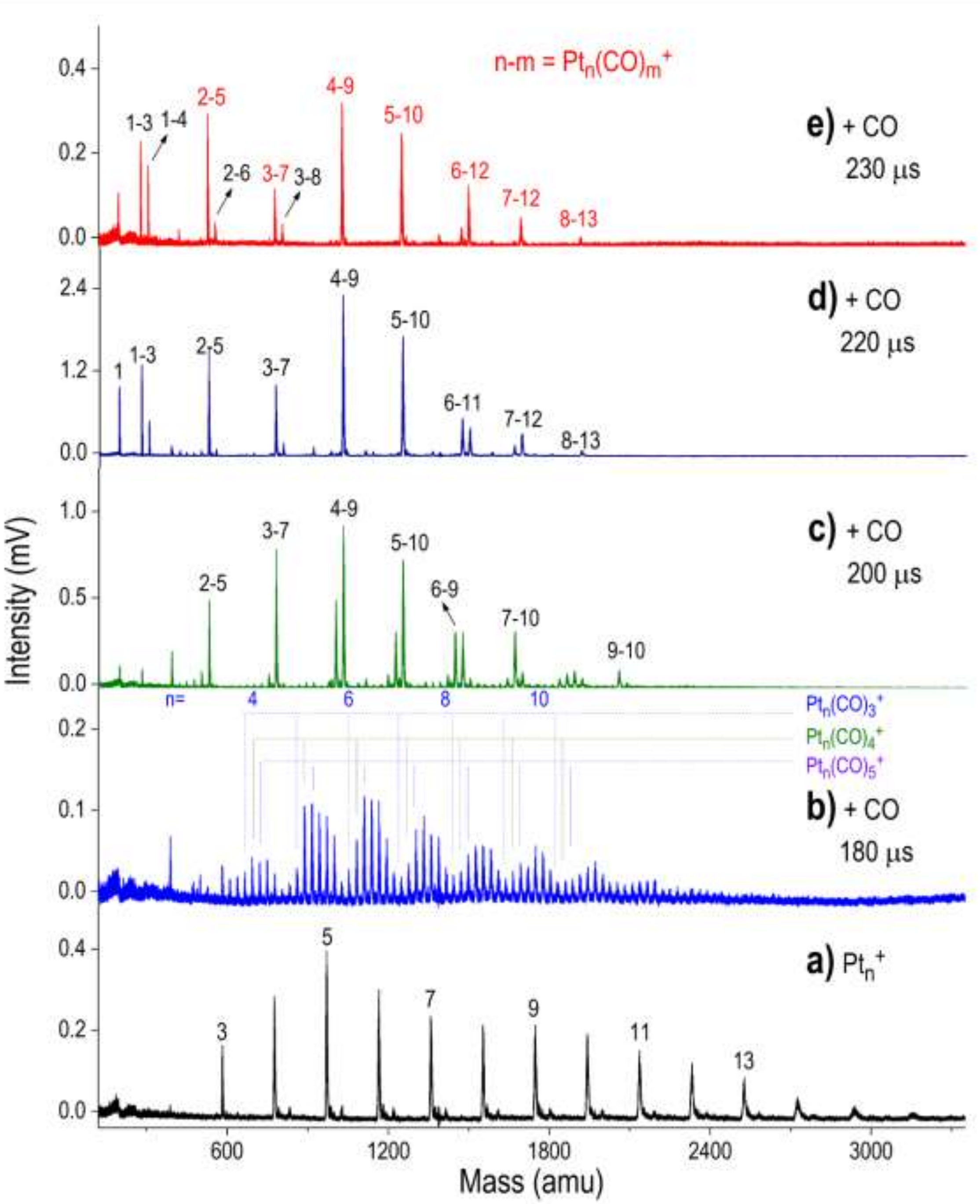

Fig. S4 Small Pt_n^+ clusters reacting with CO. Mass spectra of the nascent Pt_n^+ (n=1−15) clusters (a) and after reaction with 15% CO/He (b-e), with different doses controlled by a 10 Hz pulsed valve.

Although the pure metal clusters of $Pt_n^{\pm}$ and $Rh_n^{\pm}$ of even smaller size distributions (which challenge the preparation due to incidental contamination) exhibit a relatively less mass abundance in our preparation conditions, they also lead to the formation of predominant cluster complexes pertaining to super coordination.

S2. The reactions of $Rh_n^{\pm}$ with CO and NO

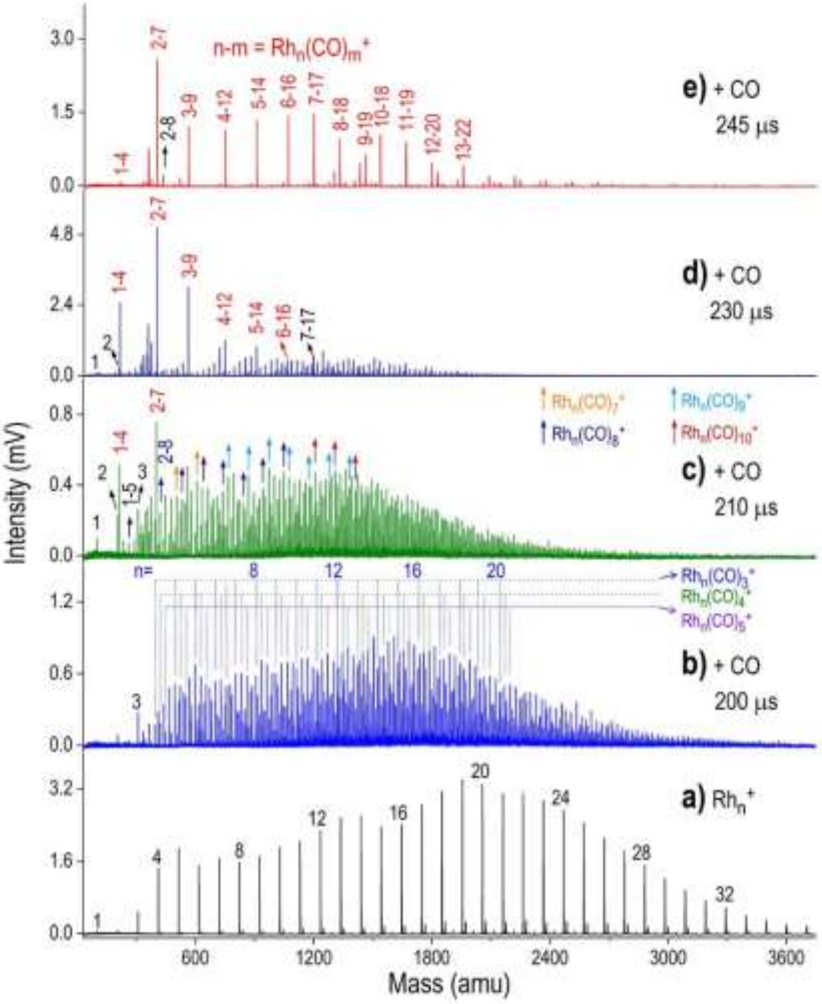

Fig. S5 Cationic Rh$_n$$^+$ clusters reacting with CO. Mass spectra of the nascent Rh$_n$$^+$ clusters (a) and after reaction with 5% CO/He (b−e), with different doses controlled by a 10-Hz pulsed valve.

Fig. S5 presents the mass spectra of pure Rh$_n$$^+$ clusters in the absence and presence of CO reactant gas (5% in He). The pure Rh$_n$$^+$ clusters were produced using laser ablation of a rhodium disk target. As a typical ligand, CO can swiftly react with Rh clusters to produce a series of cluster complexes, such as Rh$_n$CO$^+$, Rh$_n$(CO)$_2$$^+$ and Rh$_n$(CO)$_3$$^+$, corroborating prior research findings [1-7]. In the presence of sufficient CO reactant, all the Rh$_n$$^+$ clusters exhibit remarkable reaction selectivity to form a predominant cluster complex for each. Further increase of CO doses did not form complexes of a larger coordination number, indicating saturation effect of the CO coordination on the Rh$_n$$^+$ clusters. This saturation phenomenon was reliably seen in repeated experiments of CO in reacting with the small sized Rh$_n$$^+$ clusters (Fig. S6). The detection of Rh(CO)$_4$$^+$, Rh$_3(CO)_9$$^+$, Rh$_4(CO)_{12}$$^+$, and Rh$_5(CO)_{14}$$^+$ agrees with previously identified carbonyl complexes.[8-15]

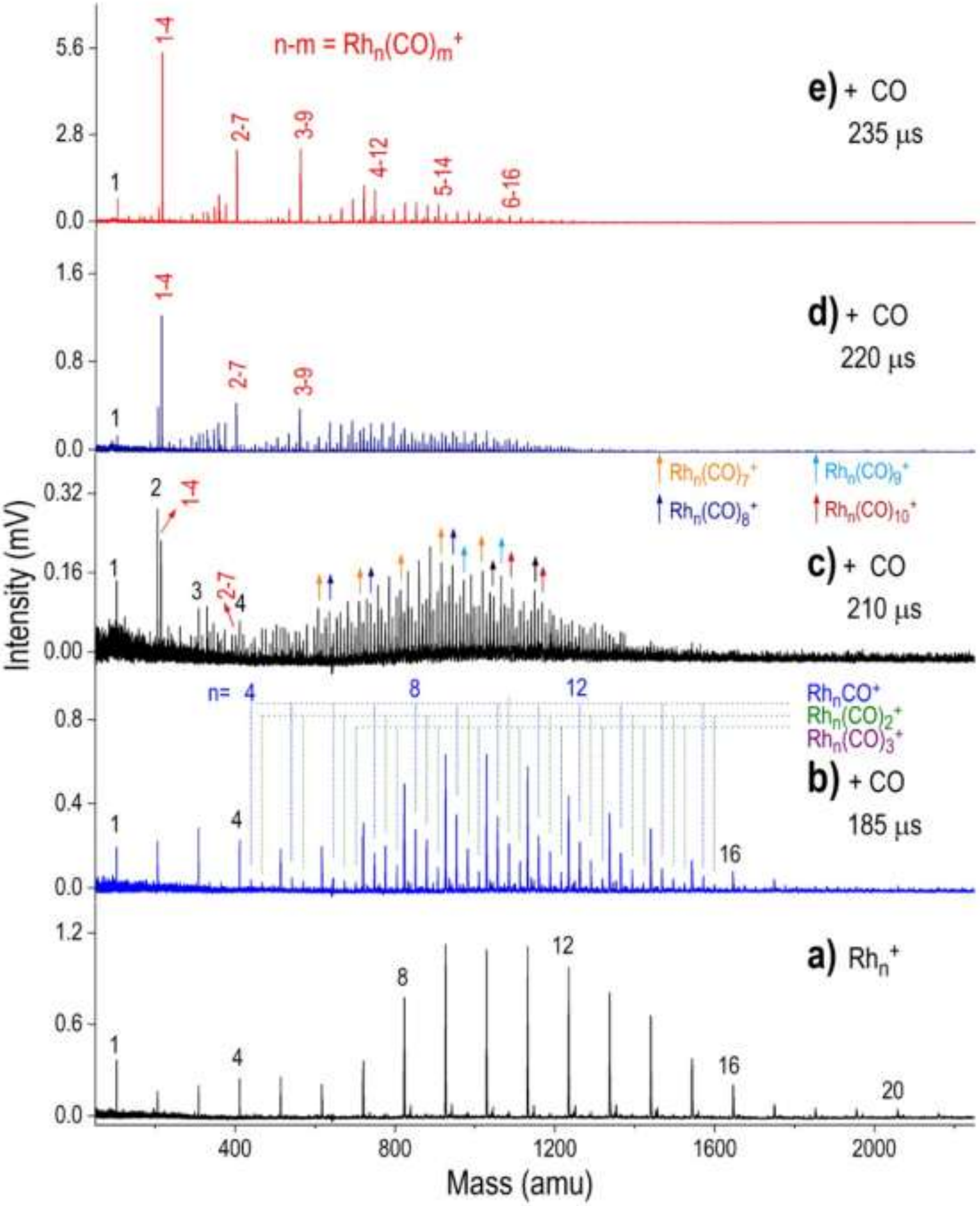

Fig. S6 Small Rh$_n^+$ reacting with CO. Mass spectra of the nascent Rh$_n^+$ (n=1−20) clusters (a) and after reaction with 5% CO/He (b−e), with different doses controlled by a 10-Hz pulsed valve.

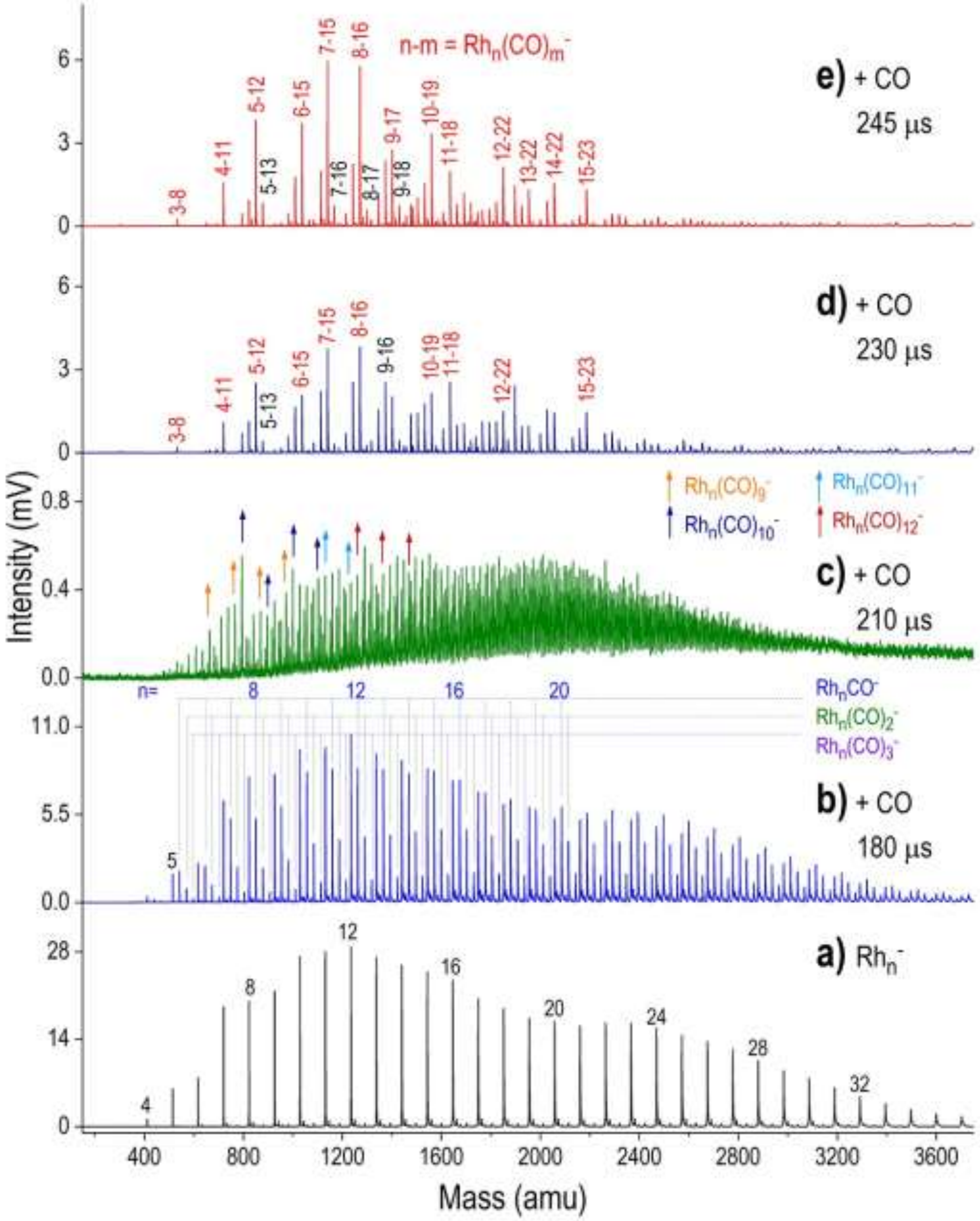

Fig. S7 Anionic Rh_n^- clusters reacting with CO. Mass spectra of the nascent Rh_n^- (n=4−35) clusters (a) and after reaction with 5% CO/He (b−e) , with different doses controlled by a 10-Hz pulsed valve.

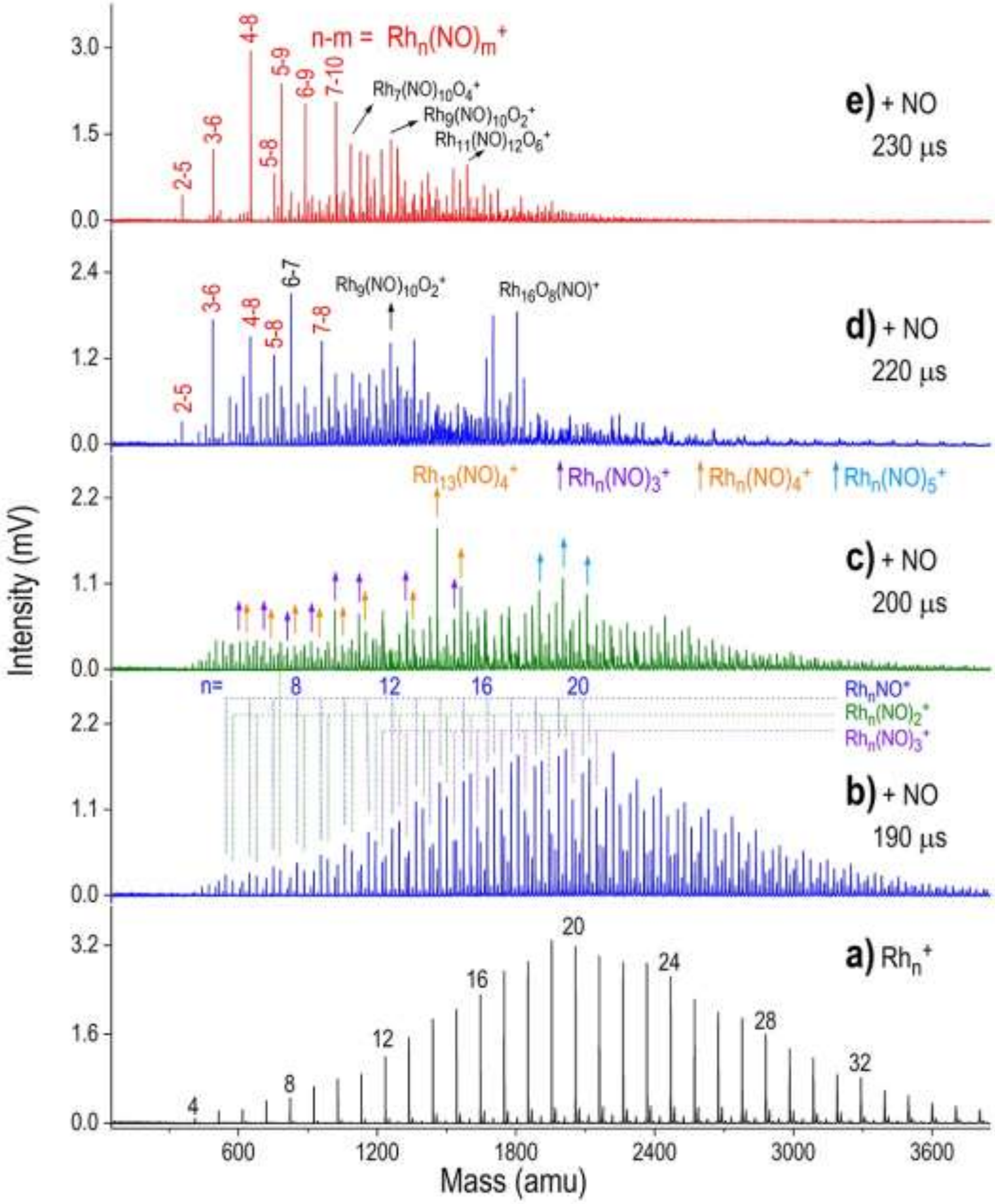

Fig. S8 Cationic Rh_n^+ clusters reacting with NO. Mass spectra of the nascent Rh_n^+ clusters (a) and after reaction with 5% NO/He (b−e), with different doses controlled by a 10-Hz pulsed valve.

Similar reactions were observed when the Rh_n^+ clusters were exposed to NO reactants (5% in He), as shown in Fig. S8. Mass spectrometry analysis reveals that NO rapidly interacts with these Rh_n^+ clusters, leading to the successive formation of $Rh_n(NO)^+$, $Rh_n(NO)_2^+$, and $Rh_n(NO)_3^+$. By increasing the doses of the NO reactants, significant products such as $Rh_2(NO)_5^+$, $Rh_3(NO)_6^+$, $Rh_4(NO)_8^+$, $Rh_5(NO)_9^+$, $Rh_6(NO)_9^+$, $Rh_7(NO)_{10}^+$, were identified, highlighting the high selectivity in forming complexes of saturable coordination.

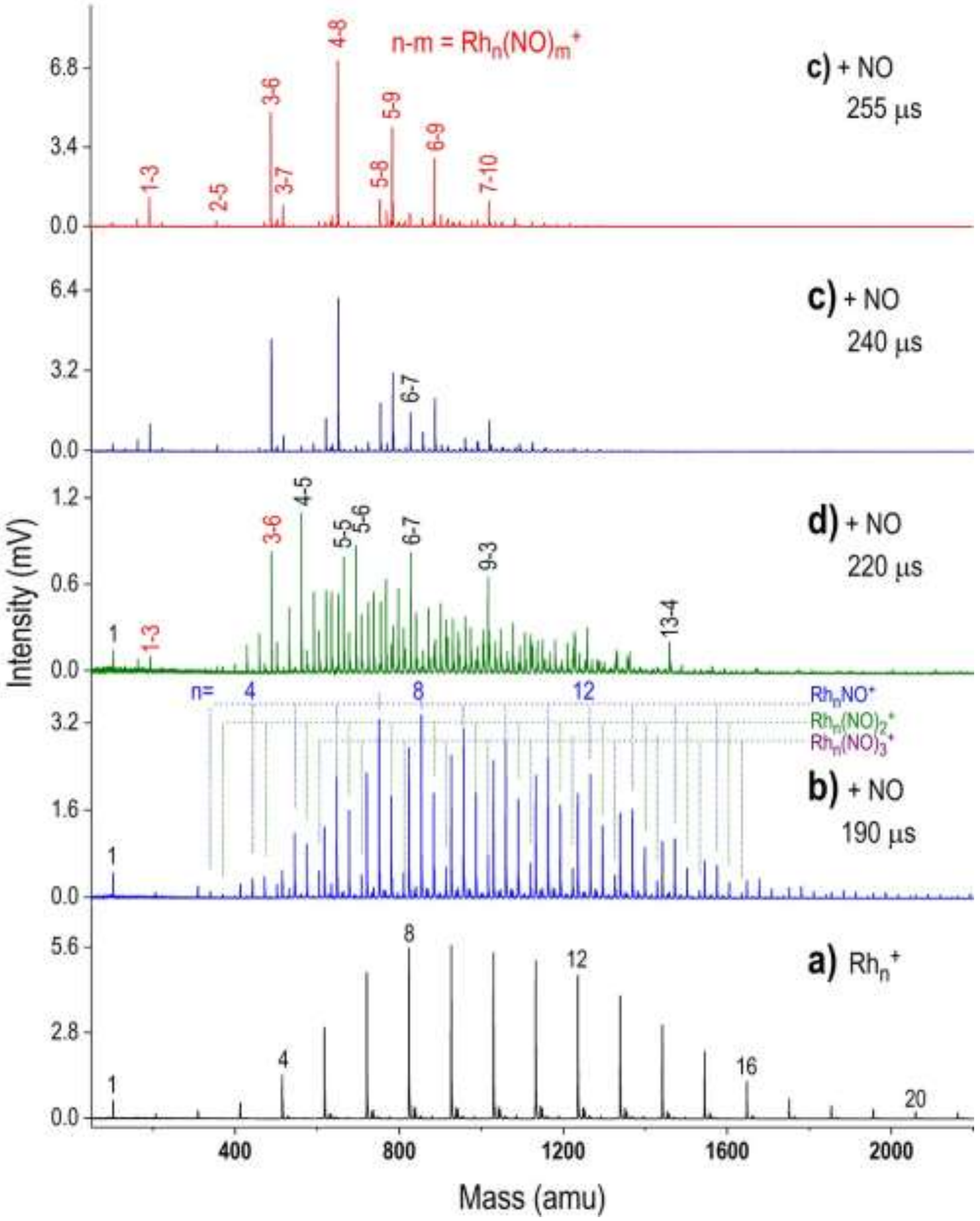

Fig. S9 Small Rh$_n^+$ reacting with NO. Mass spectra of the nascent Rh$_n^+$ (n=1−20) clusters (a) and after reaction with 5% NO/He (b-e), with different doses controlled by a 10 Hz pulsed valve.

Additionally, the reactions of anionic Rh$_n^-$ (n = 4−35) clusters were also investigated, yielding analogous super coordination products. However, the anionic clusters exhibited higher reactivity in metal-nonmetal electron-transfer reactions, with potential NO decomposition under suitable conditions [16]. It is also noteworthy that a different peak may be detected under altered experimental conditions, indicative of dynamic equilibrium of delocalized and localized electrons.

S3. Geometric structures of $Pt_n(NO)_m^+$

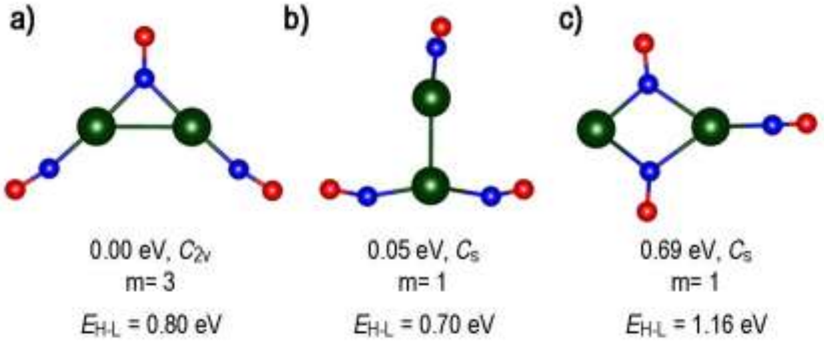

Fig. S10 Low-lying isomers of $Pt_2(NO)_3^+$ with relative energies corrected by zero-point vibrations. Also labeled, are symmetry, spin multiplicity (m) and HOMO-LUMO gap ($E_{H\text{-}L}$).

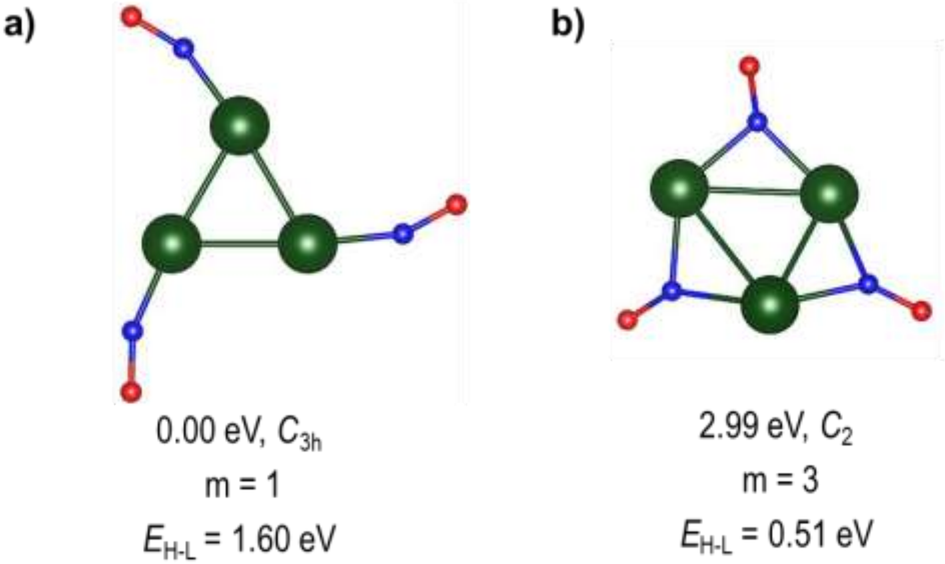

Fig. S11 Low-lying isomers of $Pt_3(NO)_3^+$ with relative energies corrected by zero-point vibrations. Also labeled, are symmetry, spin multiplicity (m) and HOMO-LUMO gap ($E_{H\text{-}L}$).

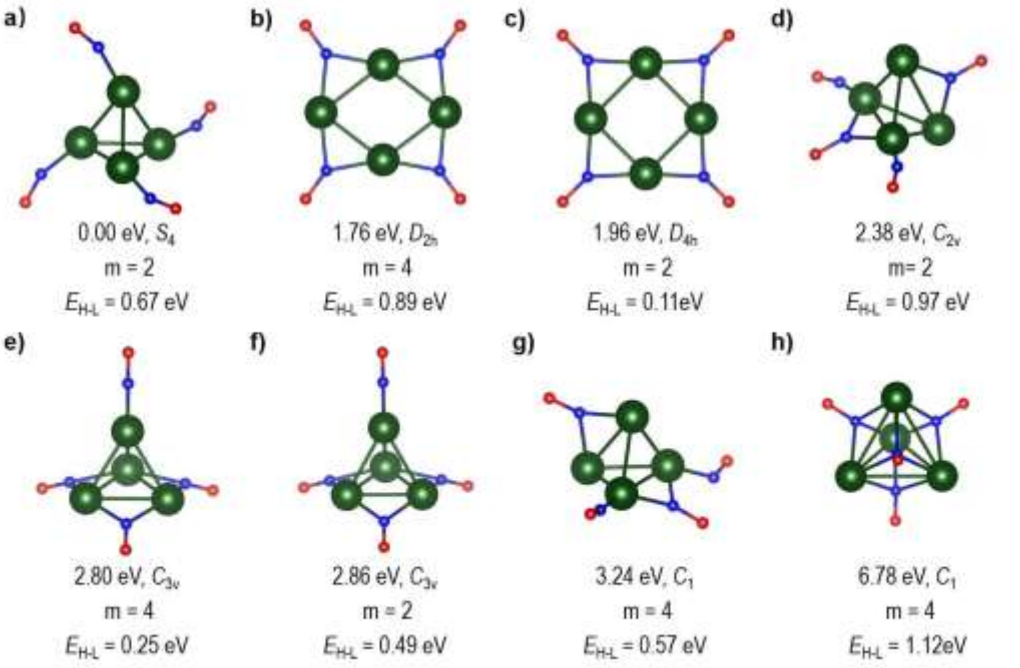

a) 0.00 eV, S_4
m = 2
$E_{\text{H-L}}$ = 0.67 eV

b) 1.76 eV, D_{2h}
m = 4
$E_{\text{H-L}}$ = 0.89 eV

c) 1.96 eV, D_{4h}
m = 2
$E_{\text{H-L}}$ = 0.11eV

d) 2.38 eV, C_{2v}
m= 2
$E_{\text{H-L}}$ = 0.97 eV

e) 2.80 eV, C_{3v}
m = 4
$E_{\text{H-L}}$ = 0.25 eV

f) 2.86 eV, C_{3v}
m = 2
$E_{\text{H-L}}$ = 0.49 eV

g) 3.24 eV, C_1
m = 4
$E_{\text{H-L}}$ = 0.57 eV

h) 6.78 eV, C_1
m = 4
$E_{\text{H-L}}$ = 1.12eV

Fig. S12 Low-lying isomers of $Pt_4(NO)_4^+$ with relative energies corrected by zero-point vibrations. Also labeled, are symmetry, spin multiplicity (m) and HOMO-LUMO gap ($E_{\text{H-L}}$).

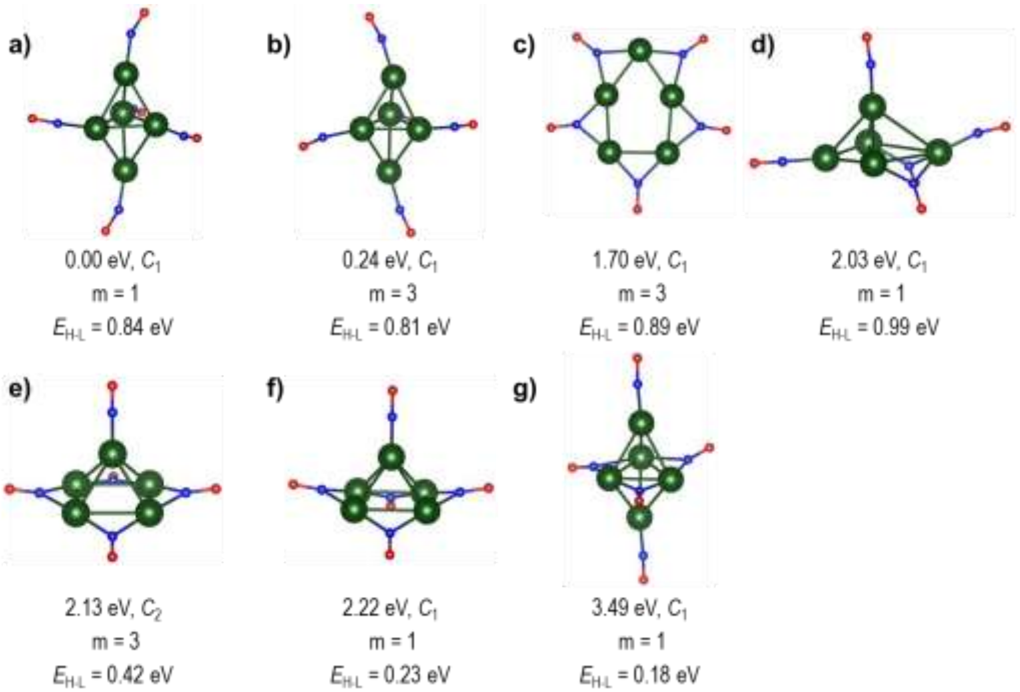

a) 0.00 eV, C_1
m = 1
$E_{\text{H-L}}$ = 0.84 eV

b) 0.24 eV, C_1
m = 3
$E_{\text{H-L}}$ = 0.81 eV

c) 1.70 eV, C_1
m = 3
$E_{\text{H-L}}$ = 0.89 eV

d) 2.03 eV, C_1
m = 1
$E_{\text{H-L}}$ = 0.99 eV

e) 2.13 eV, C_2
m = 3
$E_{\text{H-L}}$ = 0.42 eV

f) 2.22 eV, C_1
m = 1
$E_{\text{H-L}}$ = 0.23 eV

g) 3.49 eV, C_1
m = 1
$E_{\text{H-L}}$ = 0.18 eV

Fig. S13 Low-lying isomers of $Pt_5(NO)_5^+$ with relative energies corrected by zero-point vibrations. Also labeled are symmetry, spin multiplicity and HOMO-LUMO energy gap.

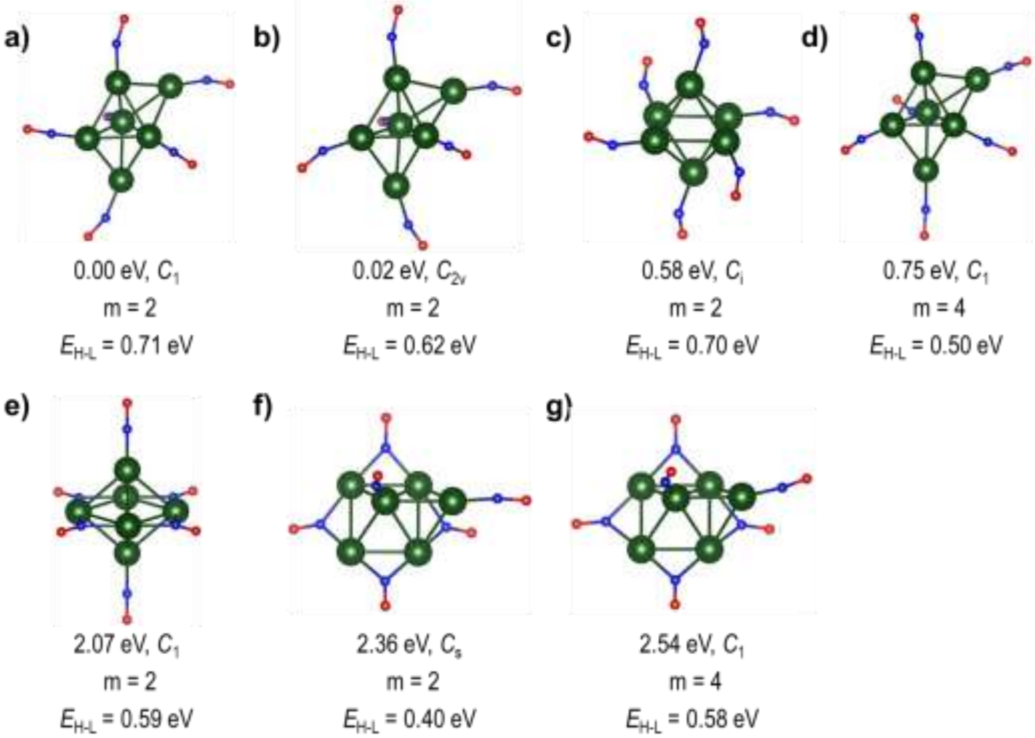

a) 0.00 eV, C_1; m = 2; $E_{\text{H-L}}$ = 0.71 eV

b) 0.02 eV, C_{2v}; m = 2; $E_{\text{H-L}}$ = 0.62 eV

c) 0.58 eV, C_i; m = 2; $E_{\text{H-L}}$ = 0.70 eV

d) 0.75 eV, C_1; m = 4; $E_{\text{H-L}}$ = 0.50 eV

e) 2.07 eV, C_1; m = 2; $E_{\text{H-L}}$ = 0.59 eV

f) 2.36 eV, C_s; m = 2; $E_{\text{H-L}}$ = 0.40 eV

g) 2.54 eV, C_1; m = 4; $E_{\text{H-L}}$ = 0.58 eV

Fig. S14 Low-lying isomers of $Pt_6(NO)_6^+$ with relative energies corrected by zero-point vibrations. Also labeled, are symmetry, spin multiplicity (m) and HOMO-LUMO gap ($E_{\text{H-L}}$).

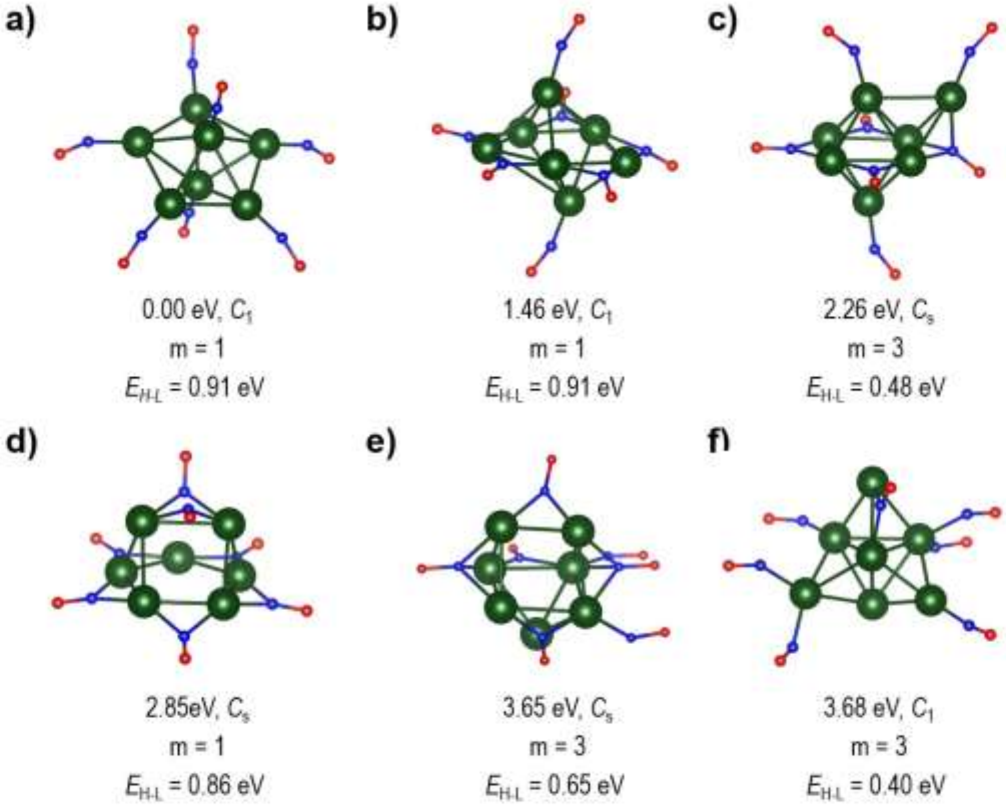

a) 0.00 eV, C_1; m = 1; $E_{H\text{-}L}$ = 0.91 eV

b) 1.46 eV, C_1; m = 1; $E_{\text{H-L}}$ = 0.91 eV

c) 2.26 eV, C_s; m = 3; $E_{\text{H-L}}$ = 0.48 eV

d) 2.85eV, C_s; m = 1; $E_{\text{H-L}}$ = 0.86 eV

e) 3.65 eV, C_s; m = 3; $E_{\text{H-L}}$ = 0.65 eV

f) 3.68 eV, C_1; m = 3; $E_{\text{H-L}}$ = 0.40 eV

Fig. S15 Low-lying isomers of $Pt_7(NO)_7^+$ with relative energies corrected by zero-point vibrations. Also labeled, are symmetry, spin multiplicity (m) and HOMO-LUMO gap ($E_{\text{H-L}}$).

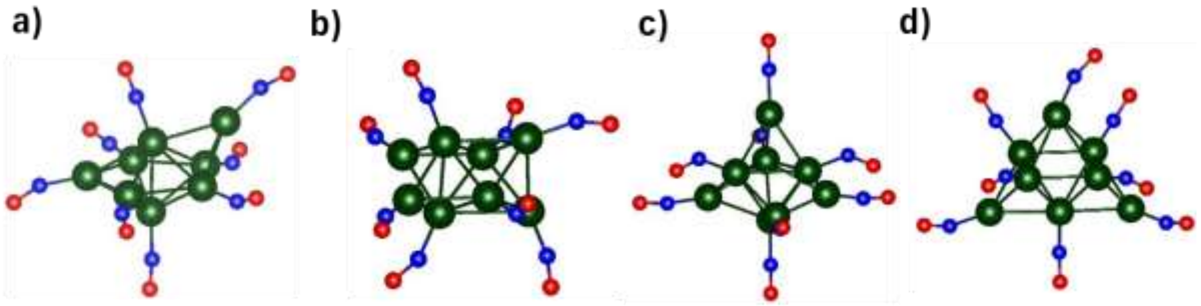

a) 0.00 eV, C_1
m = 2
$E_{H\text{-}L}$ = 0.31 eV

b) 0.43 eV, C_1
m = 2
$E_{H\text{-}L}$ = 0.69 eV

c) 0.54 eV, C_s
m = 2
$E_{H\text{-}L}$ = 0.12 eV

d) 0.55 eV, C_1
m = 2
$E_{H\text{-}L}$ = 0.25 eV

Fig. S16 Low-lying isomers of $Pt_8(NO)_8^+$ with relative energies corrected by zero-point vibrations. Also labeled, are symmetry, spin multiplicity (m) and HOMO-LUMO gap ($E_{H\text{-}L}$).

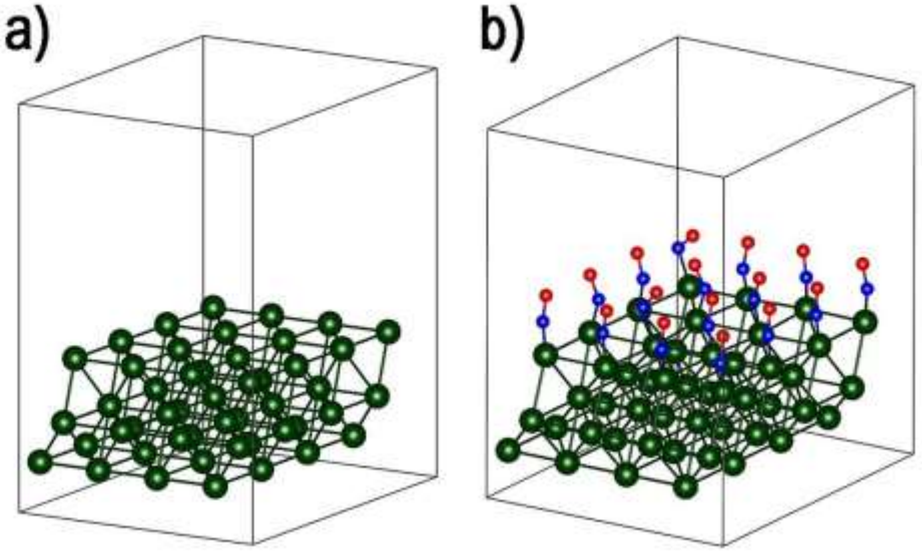

Fig. S17 The optimized Pt(111) surface before (a) and after (b) the adsorption of NO on each Pt atom site.

S4. Geometric structures of $Pt_n(NO)_m^-$

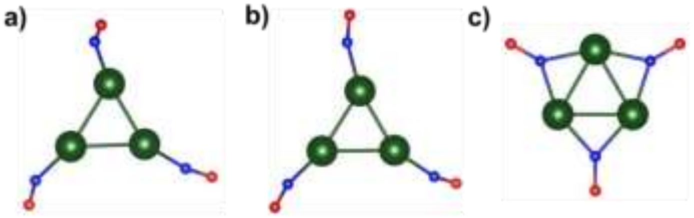

a) 0.00 eV, C_1
m = 1
E_{H-L} = 0.41 eV

b) 0.01 eV, C_1
m = 3
E_{H-L} = 0.74 eV

c) 2.03 eV, C_{3v}
m = 3
E_{H-L} = 0.55 eV

Fig. S18 Low-lying isomers of $Pt_3(NO)_3^-$ with relative energies corrected by zero-point vibrations. Also labeled, are symmetry, spin multiplicity (m) and HOMO-LUMO gap (E_{H-L}).

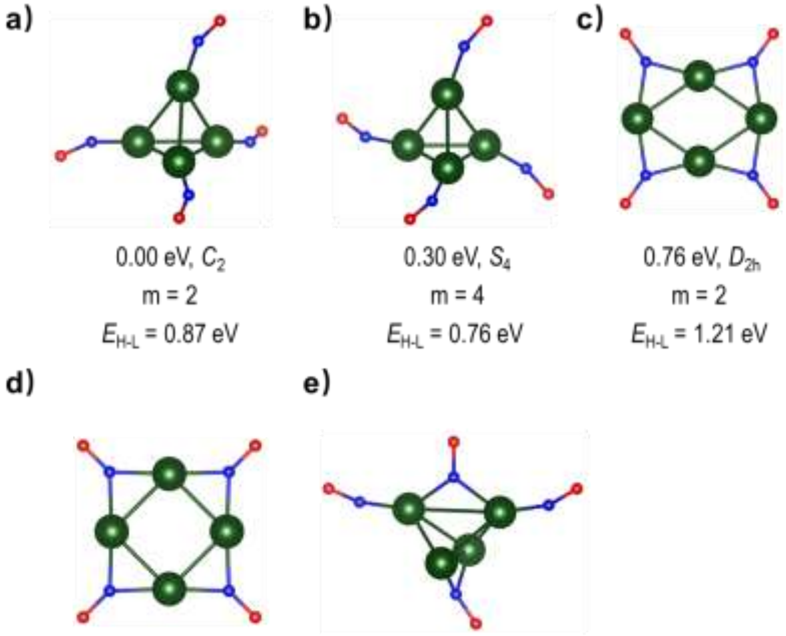

a) 0.00 eV, C_2
m = 2
E_{H-L} = 0.87 eV

b) 0.30 eV, S_4
m = 4
E_{H-L} = 0.76 eV

c) 0.76 eV, D_{2h}
m = 2
E_{H-L} = 1.21 eV

d) 0.96 eV, D_{4h}
m = 4
E_{H-L} = 1.36 eV

e) 2.39 eV, C_s
m = 2
E_{H-L} = 0.55 eV

Fig. S19 Low-lying isomers of $Pt_4(NO)_4^-$ with relative energies corrected by zero-point vibrations. Also labeled, are symmetry, spin multiplicity (m) and HOMO-LUMO gap (E_{H-L}).

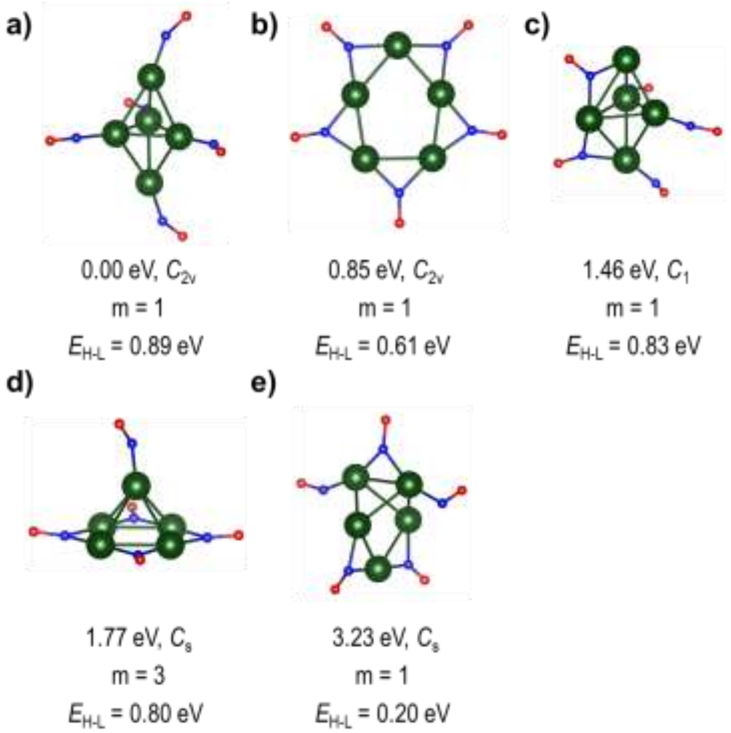

a) 0.00 eV, C_{2v} m = 1 $E_{\text{H-L}}$ = 0.89 eV

b) 0.85 eV, C_{2v} m = 1 $E_{\text{H-L}}$ = 0.61 eV

c) 1.46 eV, C_1 m = 1 $E_{\text{H-L}}$ = 0.83 eV

d) 1.77 eV, C_s m = 3 $E_{\text{H-L}}$ = 0.80 eV

e) 3.23 eV, C_s m = 1 $E_{\text{H-L}}$ = 0.20 eV

Fig. S20 Low-lying isomers of $Pt_5(NO)_5^-$ with relative energies corrected by zero-point vibrations. Also labeled, are symmetry, spin multiplicity (m) and HOMO-LUMO gap ($E_{\text{H-L}}$).

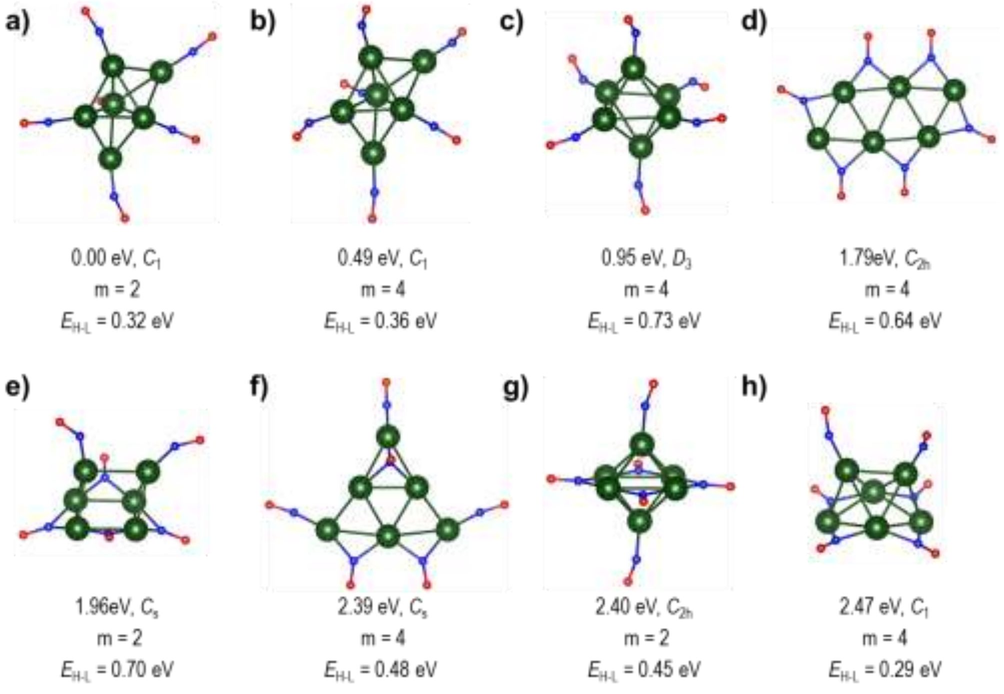

a) 0.00 eV, C_1 m = 2 $E_{\text{H-L}}$ = 0.32 eV

b) 0.49 eV, C_1 m = 4 $E_{\text{H-L}}$ = 0.36 eV

c) 0.95 eV, D_3 m = 4 $E_{\text{H-L}}$ = 0.73 eV

d) 1.79eV, C_{2h} m = 4 $E_{\text{H-L}}$ = 0.64 eV

e) 1.96eV, C_s m = 2 $E_{\text{H-L}}$ = 0.70 eV

f) 2.39 eV, C_s m = 4 $E_{\text{H-L}}$ = 0.48 eV

g) 2.40 eV, C_{2h} m = 2 $E_{\text{H-L}}$ = 0.45 eV

h) 2.47 eV, C_1 m = 4 $E_{\text{H-L}}$ = 0.29 eV

Fig. S21 Low-lying isomers of $Pt_6(NO)_6^-$ with relative energies corrected by zero-point vibrations. Also labeled, are symmetry, spin multiplicity (m) and HOMO-LUMO gap ($E_{\text{H-L}}$).

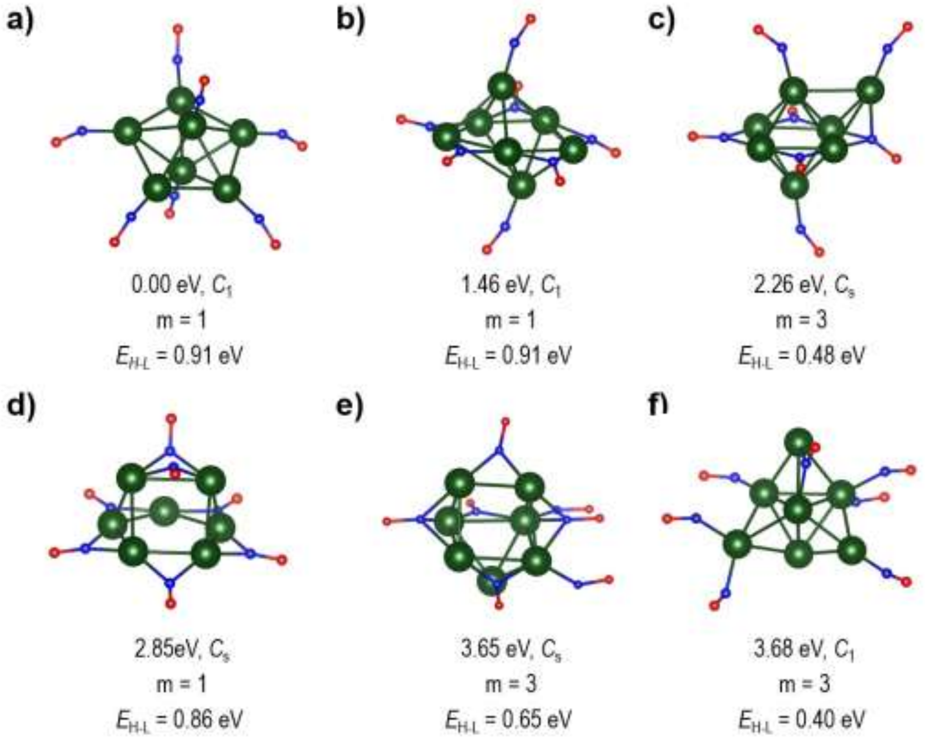

Fig. S22 Low-lying isomers of $Pt_7(NO)_7^-$ with relative energies corrected by zero-point vibrations. Also labeled, are symmetry, spin multiplicity (m) and HOMO-LUMO gap ($E_{H\text{-}L}$).

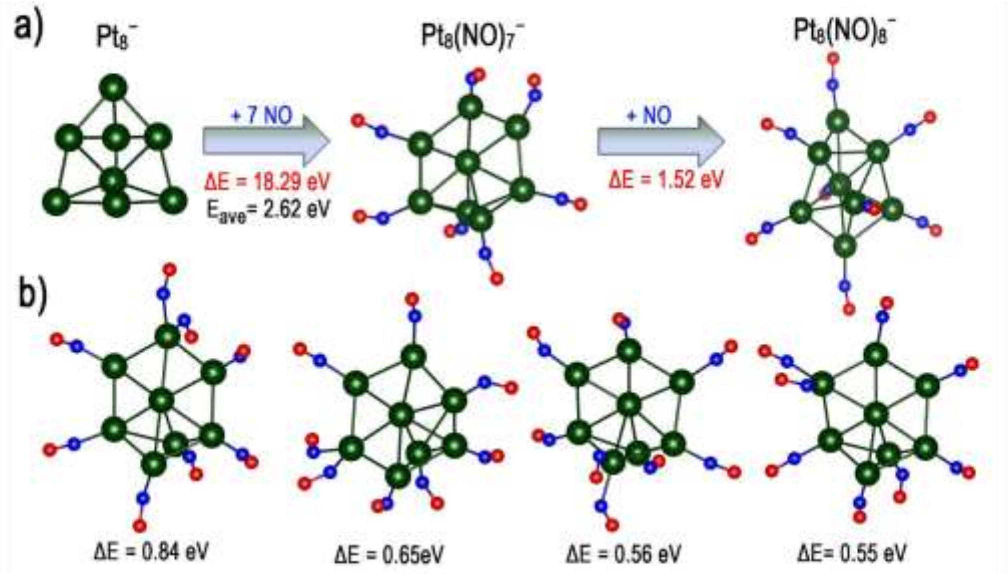

Fig. S23 The energy gain of NO-adsorption on the lowest-energy Pt_8^-, with relative energies corrected by zero-point vibrations. (a) The seven NO molecules bring forth core-shell structure to $Pt_8(NO)_7^-$ with significant energy drop, but the eighth NO could induce a cage Pt_8 in forming the lowest energy $Pt_8(NO)_8^-$. (b) Low-lying isomers of $Pt_8(NO)_8^-$, indicating a dynamically unfavorable process of $Pt_8(NO)_7^-$ to $Pt_8(NO)_8^-$.

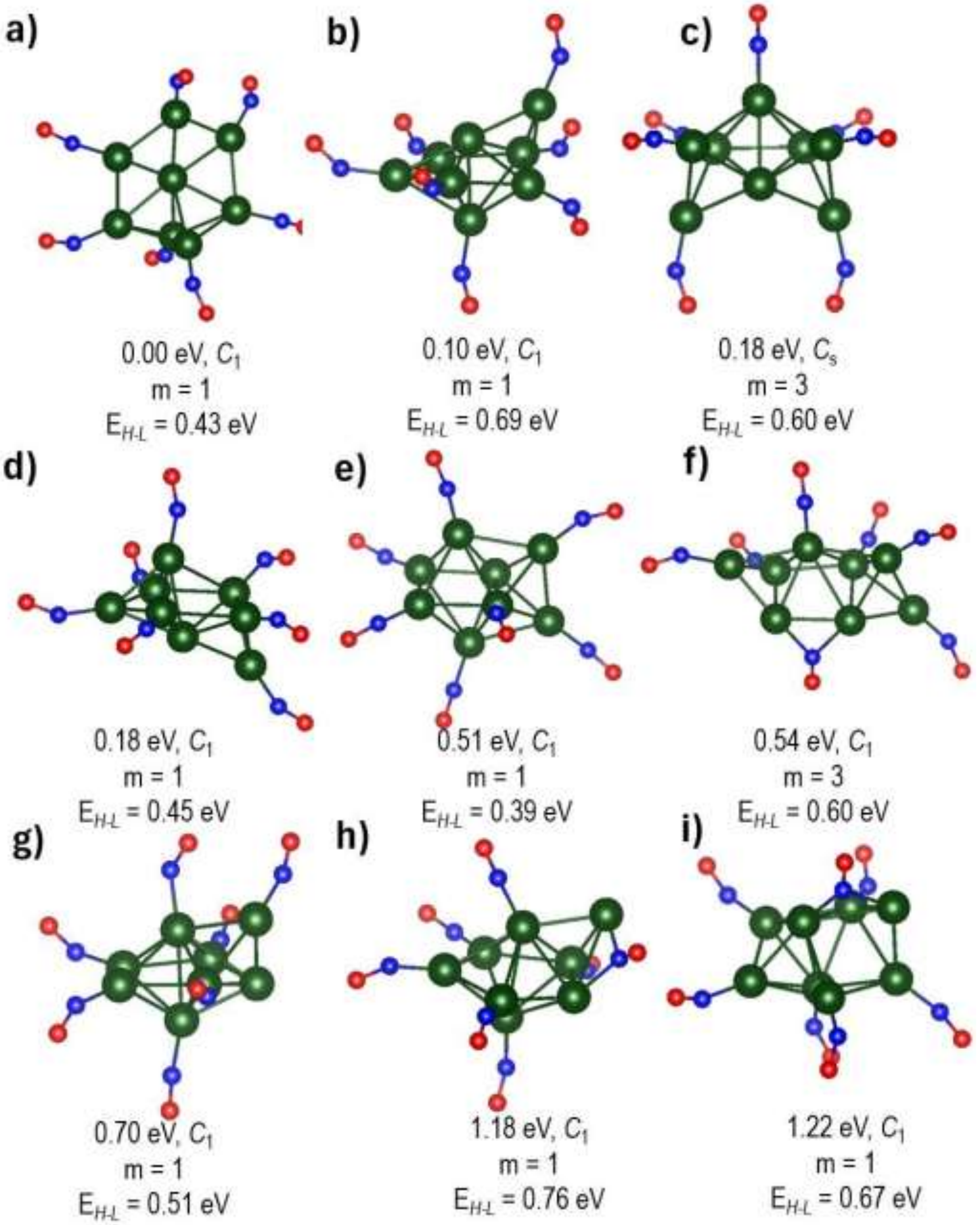

a) 0.00 eV, C_1
m = 1
$E_{H\text{-}L}$ = 0.43 eV

b) 0.10 eV, C_1
m = 1
$E_{H\text{-}L}$ = 0.69 eV

c) 0.18 eV, C_s
m = 3
$E_{H\text{-}L}$ = 0.60 eV

d) 0.18 eV, C_1
m = 1
$E_{H\text{-}L}$ = 0.45 eV

e) 0.51 eV, C_1
m = 1
$E_{H\text{-}L}$ = 0.39 eV

f) 0.54 eV, C_1
m = 3
$E_{H\text{-}L}$ = 0.60 eV

g) 0.70 eV, C_1
m = 1
$E_{H\text{-}L}$ = 0.51 eV

h) 1.18 eV, C_1
m = 1
$E_{H\text{-}L}$ = 0.76 eV

i) 1.22 eV, C_1
m = 1
$E_{H\text{-}L}$ = 0.67 eV

Fig. S24 Low-lying isomers of $Pt_8(NO)_7^-$ with relative energies corrected by zero-point vibrations. Also labeled, are symmetry, spin multiplicity (m) and HOMO-LUMO gap ($E_{\text{H-L}}$).

S5. AdNDP analysis of $Pt_n(NO)_m^+$

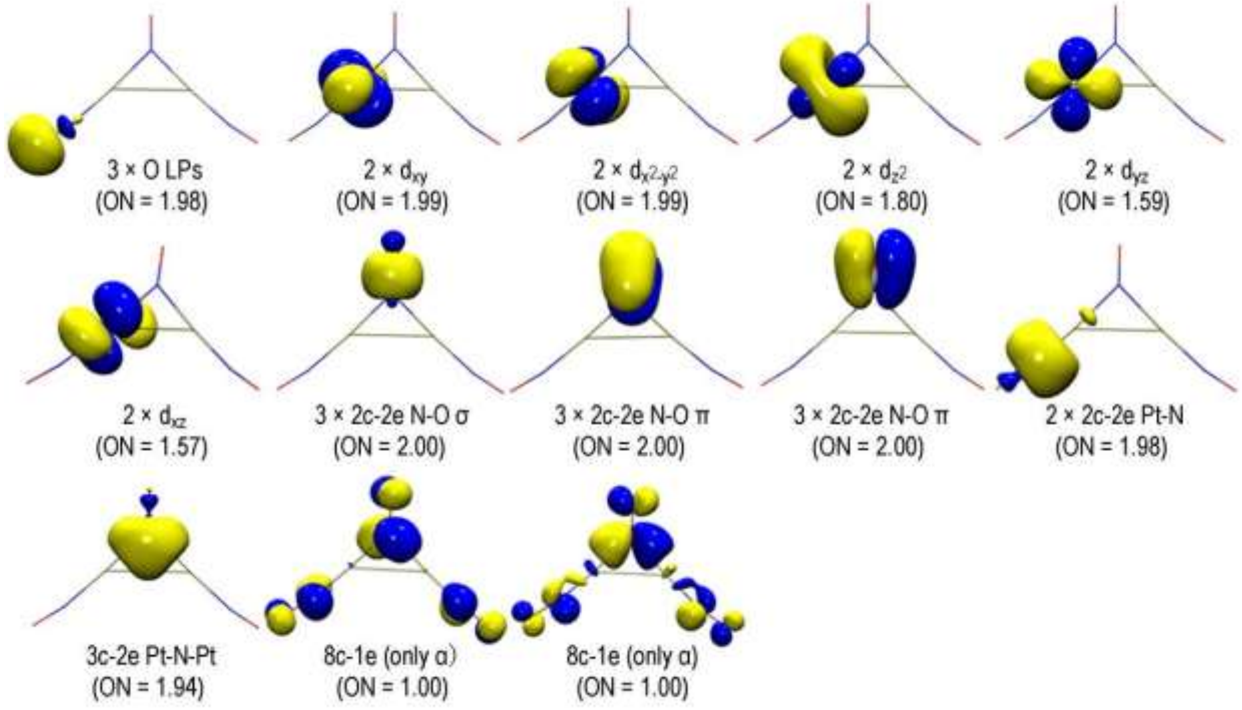

3 × O LPs (ON = 1.98)

2 × d_{xy} (ON = 1.99)

2 × $d_{x^2-y^2}$ (ON = 1.99)

2 × d_{z^2} (ON = 1.80)

2 × d_{yz} (ON = 1.59)

2 × d_{xz} (ON = 1.57)

3 × 2c-2e N-O σ (ON = 2.00)

3 × 2c-2e N-O π (ON = 2.00)

3 × 2c-2e N-O π (ON = 2.00)

2 × 2c-2e Pt-N (ON = 1.98)

3c-2e Pt-N-Pt (ON = 1.94)

8c-1e (only α) (ON = 1.00)

8c-1e (only α) (ON = 1.00)

Fig. S25 AdNDP analysis of Pt$_2$(NO)$_3^+$. Only one of the same type of orbitals is given for clarity. ON denotes the occupancy number (|e|). The isovalues are set to 0.05 for all.

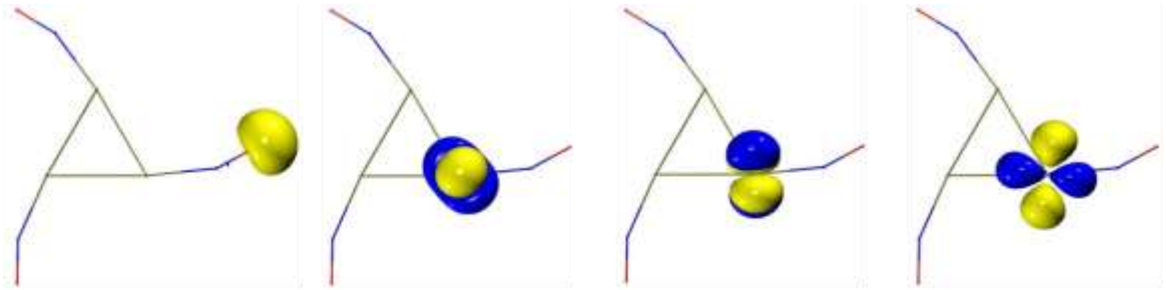

3 × O LPs (ON = 1.98)

3 × d_{z2} (ON = 1.99)

3 × d_{yz} (ON = 1.94)

3 × d_{x2-y2} (ON = 1.84)

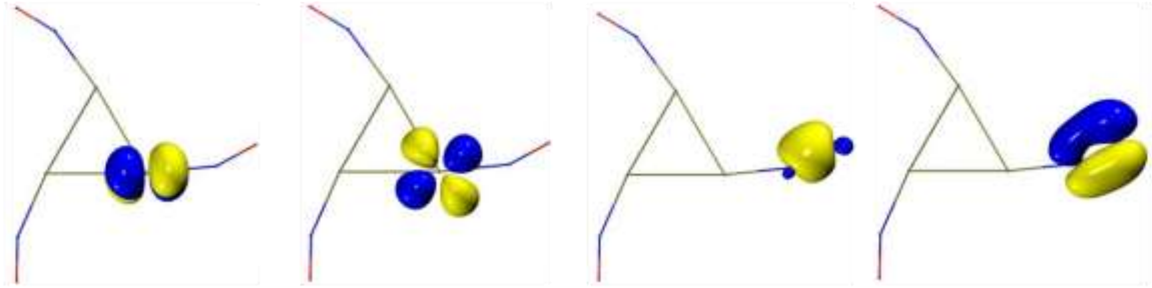

3 × d_{xz} (ON = 1.59)

3 × d_{xy} (ON = 1.58)

3 × 2c-2e N-O σ (ON = 2.00)

3 × 2c-2e N-O π (ON = 2.00)

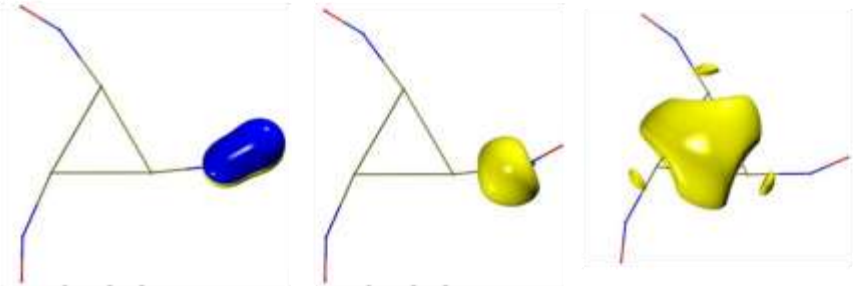

3 × 2c-2e N-O π (ON = 2.00)

3 × 2c-2e Pt-N (ON = 1.96)

3c-2e (ON = 1.62)

Fig. S26 AdNDP analysis of $Pt_3(NO)_3^+$. Only one of the same type of orbitals is given for clarity. ON denotes the occupancy number (|e|). The isovalues are set to 0.05 for all.

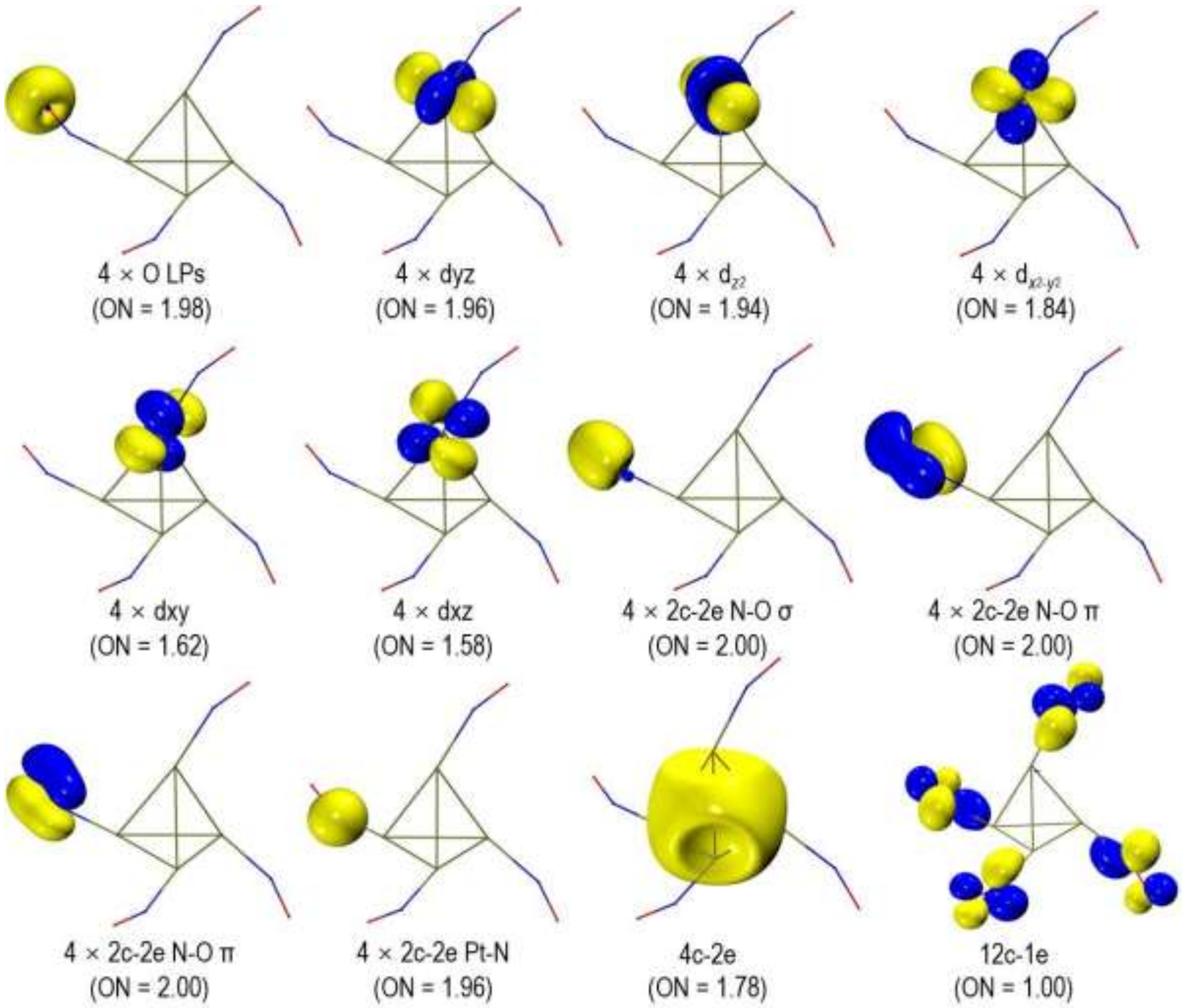

4 × O LPs (ON = 1.98)

4 × dyz (ON = 1.96)

4 × d_{z^2} (ON = 1.94)

4 × $d_{x^2-y^2}$ (ON = 1.84)

4 × dxy (ON = 1.62)

4 × dxz (ON = 1.58)

4 × 2c-2e N-O σ (ON = 2.00)

4 × 2c-2e N-O π (ON = 2.00)

4 × 2c-2e N-O π (ON = 2.00)

4 × 2c-2e Pt-N (ON = 1.96)

4c-2e (ON = 1.78)

12c-1e (ON = 1.00)

Fig. S27 AdNDP analysis of $Pt_4(NO)_4^+$. Only one of the same type of orbitals is given for clarity. ON denotes the occupancy number (|e|). The isovalues are set to 0.05 for all.

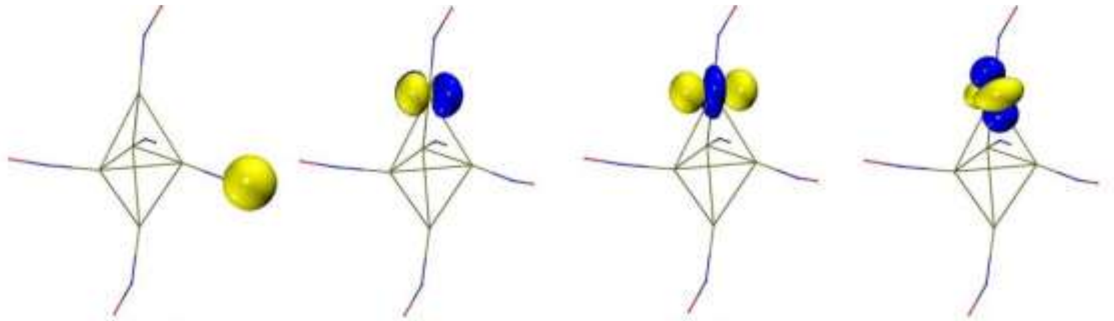

5 × O LPs (ON = 1.97-1.98)

$5 \times d_{xz}$ (ON = 1.95-1.97)

$5 \times d_{z^2}$ (ON = 1.92-1.95)

$5 \times d_{x^2\text{-}y^2}$ (ON = 1.80-1.91)

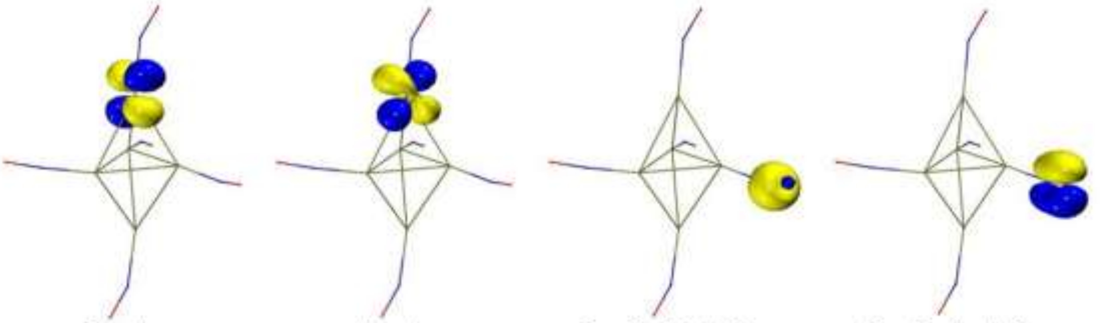

$5 \times d_{xy}$ (ON = 1.58-1.64)

$5 \times d_{yz}$ (ON = 1.56-1.63)

5 × 2c-2e N-O σ (ON = 2.00)

5 × 2c-2e N-O π (ON = 2.00)

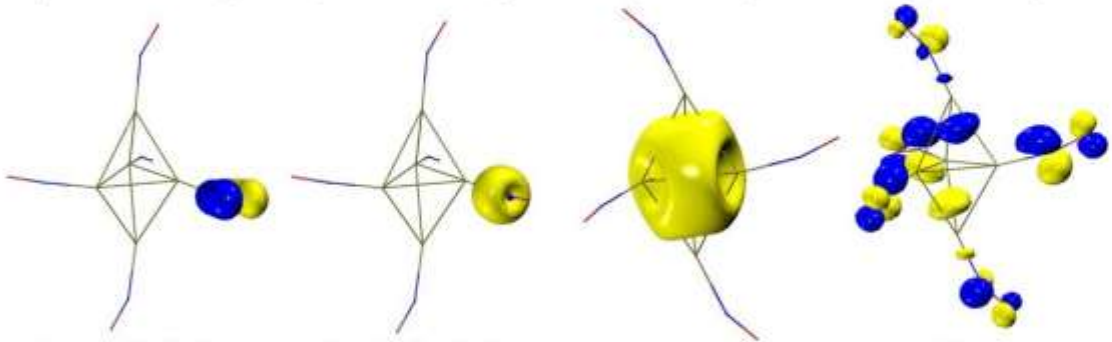

5 × 2c-2e N-O π (ON = 2.00)

5 × 2c-2e Pt-N (ON = 1.95-1.96)

5c-2e (ON = 1.87)

15c-2e (ON = 1.71)

Fig. S28 AdNDP analysis of $Pt_5(NO)_5^+$, with only one of the same type of orbitals being displayed ON denotes the occupancy number (|e|). The isovalues are set to 0.05 for all.

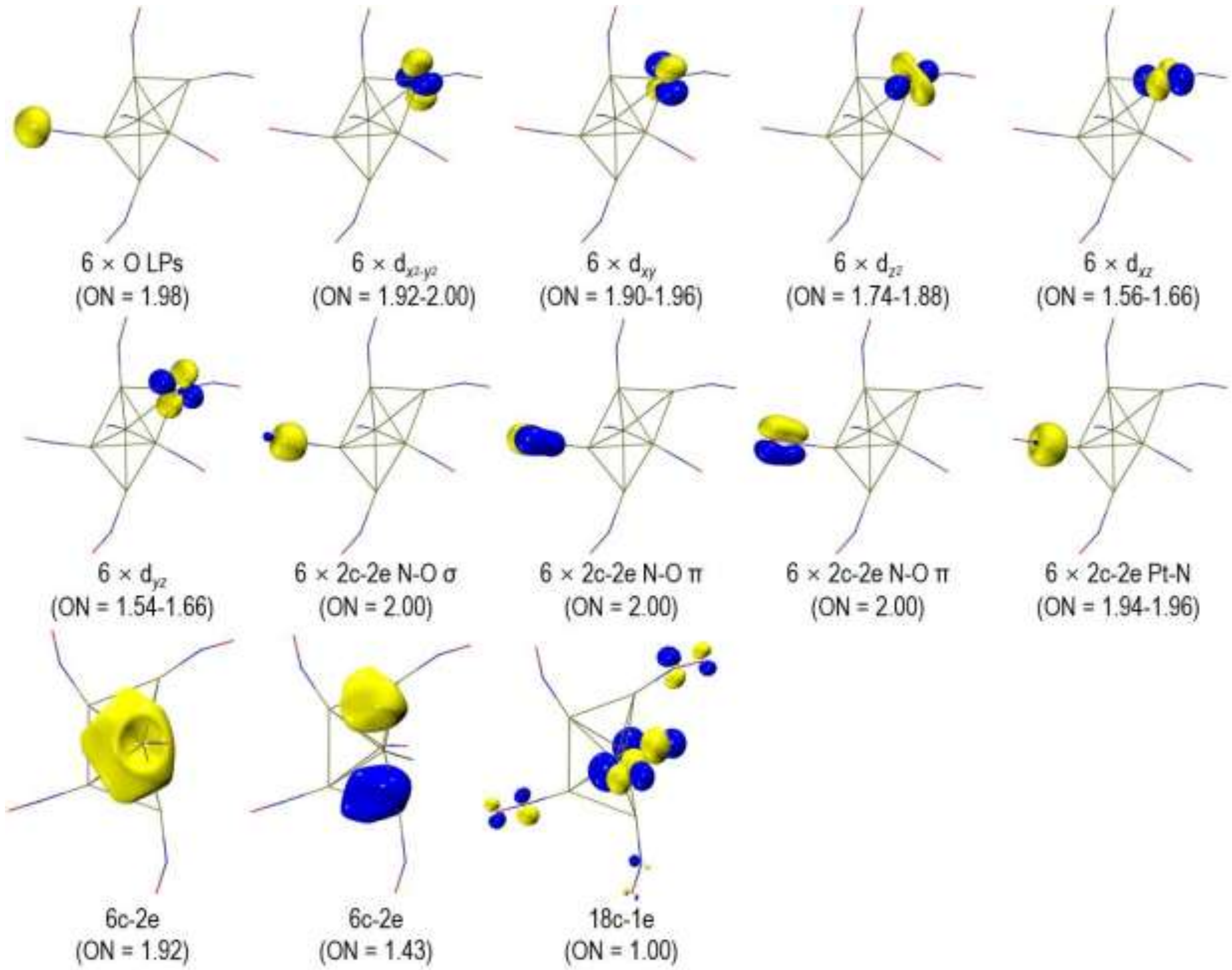

6 × O LPs (ON = 1.98)

6 × $d_{x2\text{-}y2}$ (ON = 1.92-2.00)

6 × d_{xy} (ON = 1.90-1.96)

6 × d_{z2} (ON = 1.74-1.88)

6 × d_{xz} (ON = 1.56-1.66)

6 × d_{yz} (ON = 1.54-1.66)

6 × 2c-2e N-O σ (ON = 2.00)

6 × 2c-2e N-O π (ON = 2.00)

6 × 2c-2e N-O π (ON = 2.00)

6 × 2c-2e Pt-N (ON = 1.94-1.96)

6c-2e (ON = 1.92)

6c-2e (ON = 1.43)

18c-1e (ON = 1.00)

Fig. S29 AdNDP analysis of $Pt_6(NO)_6^+$, with only one of the same type of orbitals being displayed. ON denotes the occupancy number (|e|). The isovalues are set to 0.05 for all.

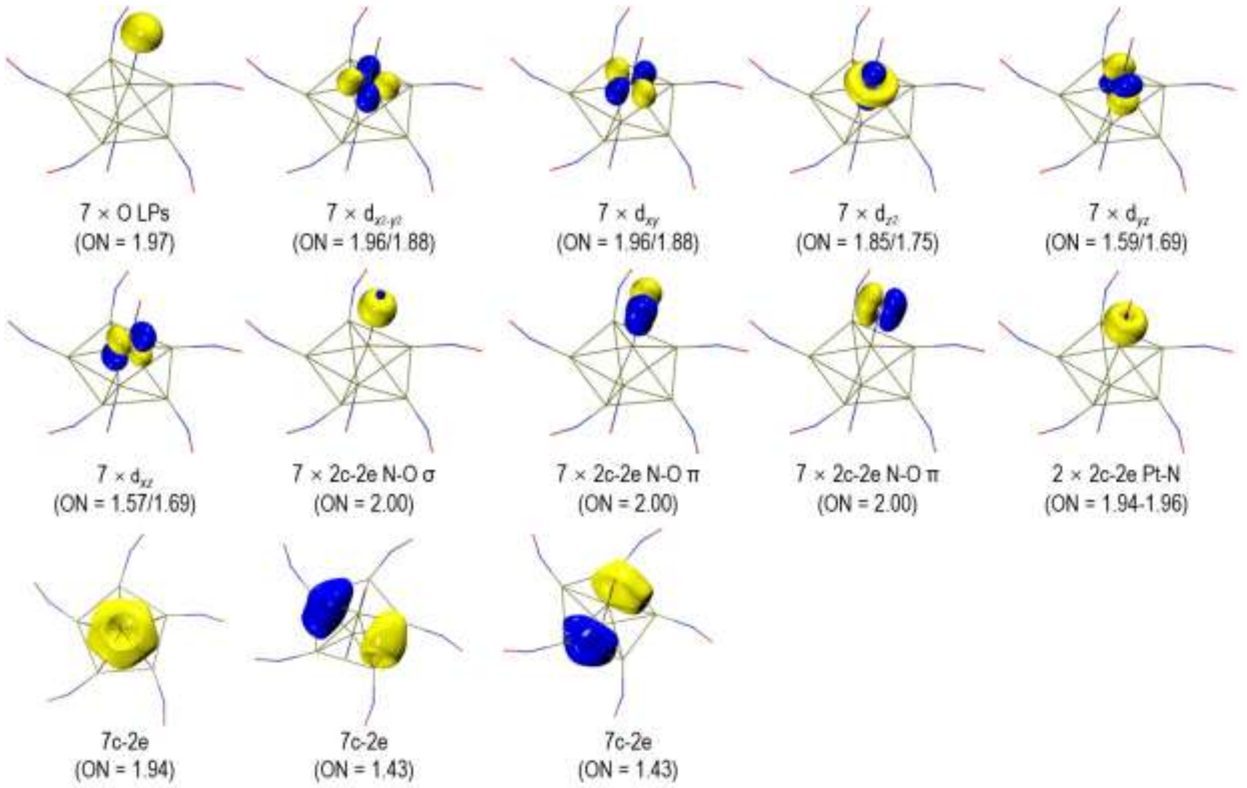

7 × O LPs (ON = 1.97)

7 × $d_{x^2-y^2}$ (ON = 1.96/1.88)

7 × d_{xy} (ON = 1.96/1.88)

7 × d_{z^2} (ON = 1.85/1.75)

7 × d_{yz} (ON = 1.59/1.69)

7 × d_{xz} (ON = 1.57/1.69)

7 × 2c-2e N-O σ (ON = 2.00)

7 × 2c-2e N-O π (ON = 2.00)

7 × 2c-2e N-O π (ON = 2.00)

2 × 2c-2e Pt-N (ON = 1.94-1.96)

7c-2e (ON = 1.94)

7c-2e (ON = 1.43)

7c-2e (ON = 1.43)

Fig. S30 AdNDP analysis of $Pt_7(NO)_7^+$. Only one of the same type of orbitals is given for clarity. ON denotes the occupancy number (|e|). The isovalues are set to 0.05 for all.

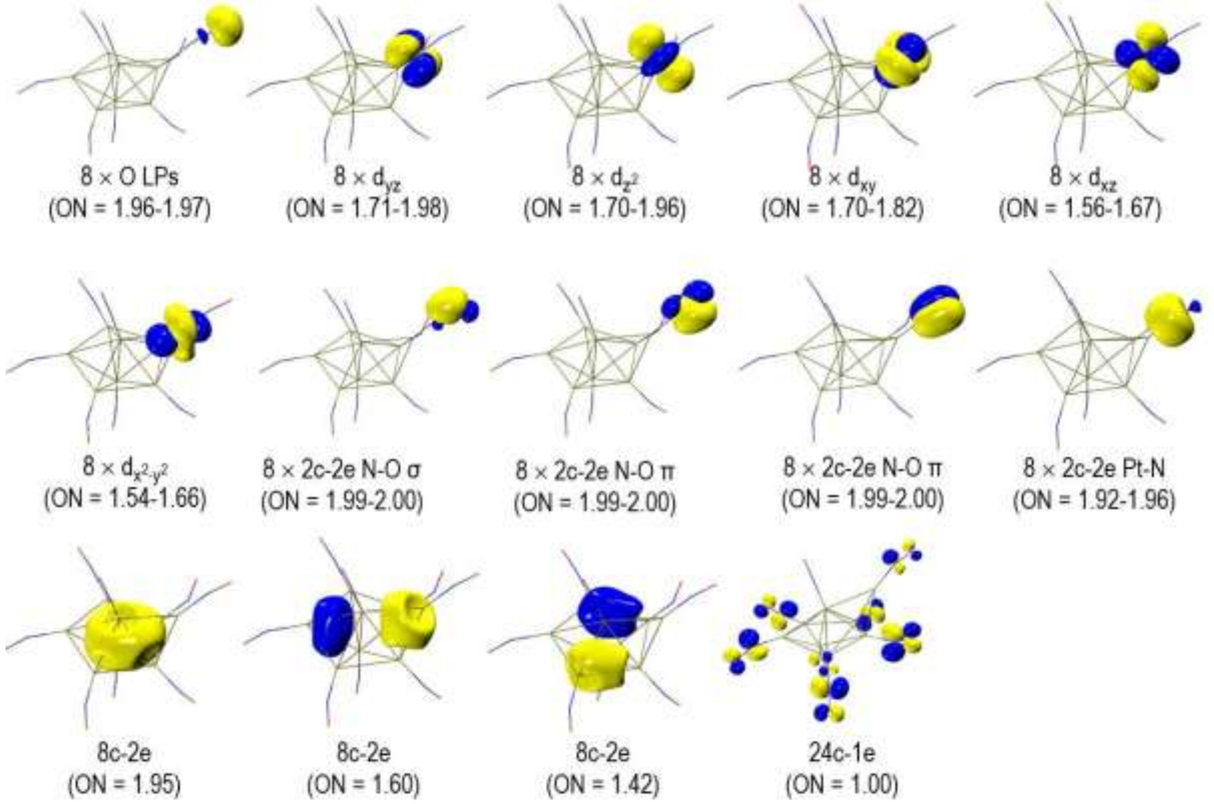

8 × O LPs (ON = 1.96-1.97)

8 × d_{yz} (ON = 1.71-1.98)

8 × d_{z^2} (ON = 1.70-1.96)

8 × d_{xy} (ON = 1.70-1.82)

8 × d_{xz} (ON = 1.56-1.67)

8 × $d_{x^2-y^2}$ (ON = 1.54-1.66)

8 × 2c-2e N-O σ (ON = 1.99-2.00)

8 × 2c-2e N-O π (ON = 1.99-2.00)

8 × 2c-2e N-O π (ON = 1.99-2.00)

8 × 2c-2e Pt-N (ON = 1.92-1.96)

8c-2e (ON = 1.95)

8c-2e (ON = 1.60)

8c-2e (ON = 1.42)

24c-1e (ON = 1.00)

Fig. S31 AdNDP analysis of $Pt_8(NO)_8^+$. Only one of the same type of orbitals is given for clarity. ON denotes the occupancy number (|e|). The isovalues are set to 0.05 for all.

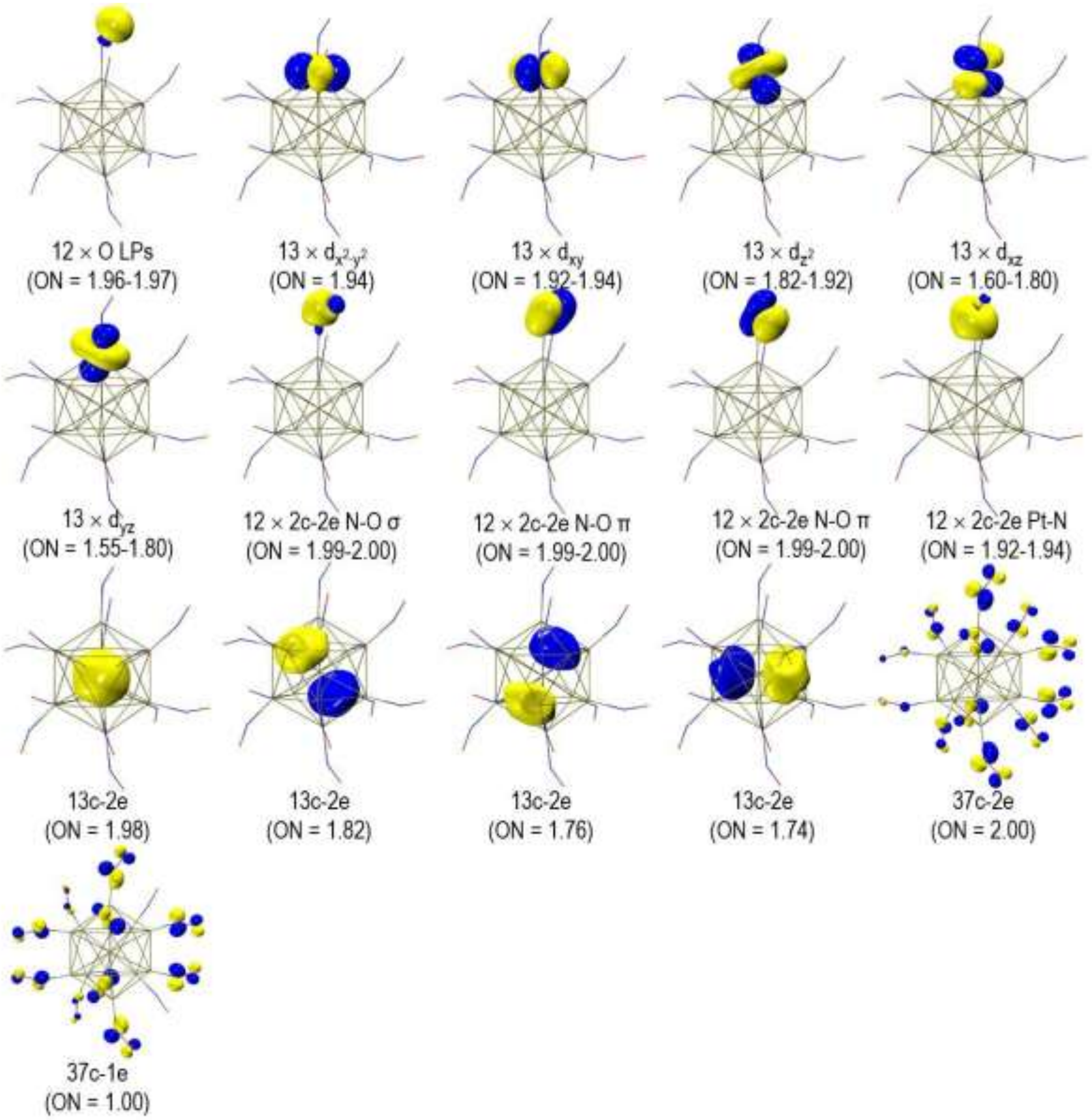

Fig. S32 AdNDP analysis of $Pt_{13}(NO)_{12}^+$. Only one of the same type of orbitals is given for clarity. ON denotes the occupancy number (|e|). The isovalues are set to 0.05 for all.

S6. AdNDP analysis of the $Pt_n(NO)_m^-$

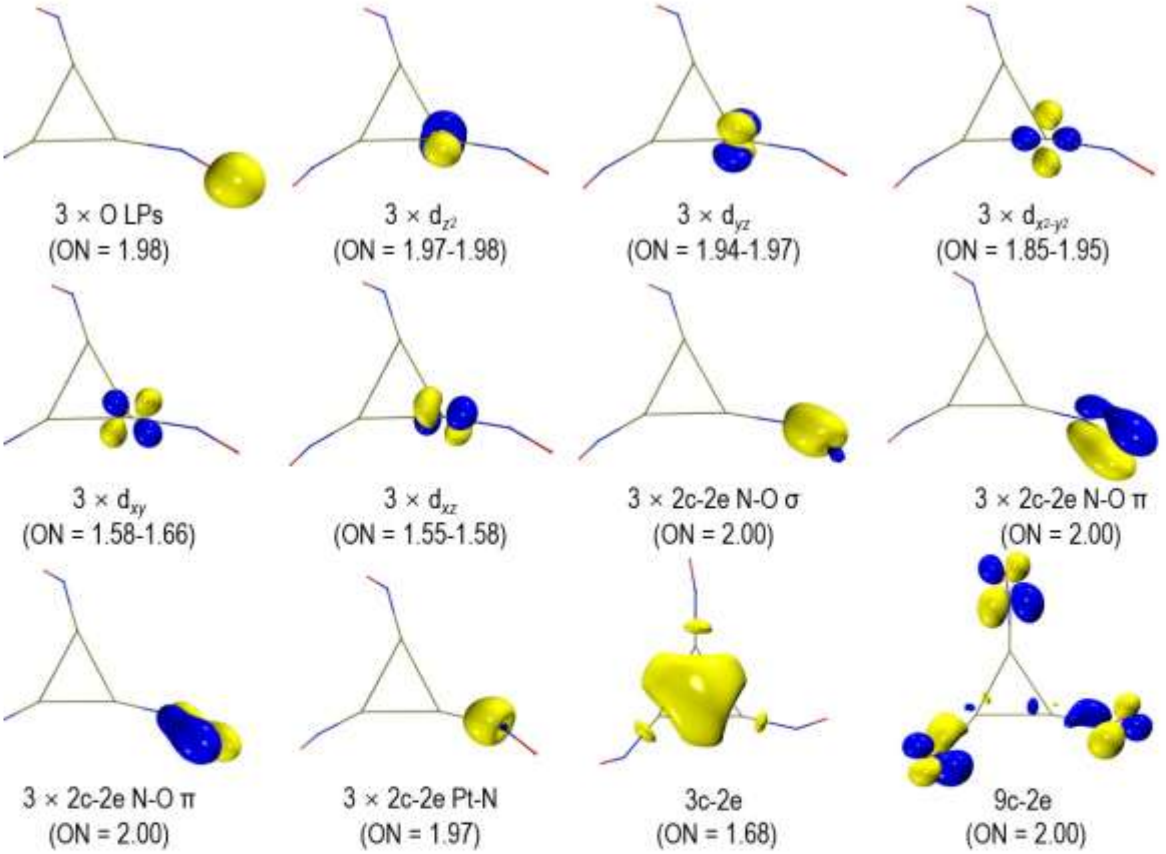

Fig. S33 AdNDP analysis of $Pt_3(NO)_3^-$. Only one of the same type of orbitals is given for clarity. ON denotes the occupancy number (|e|). The isovalues are set to 0.05 for all.

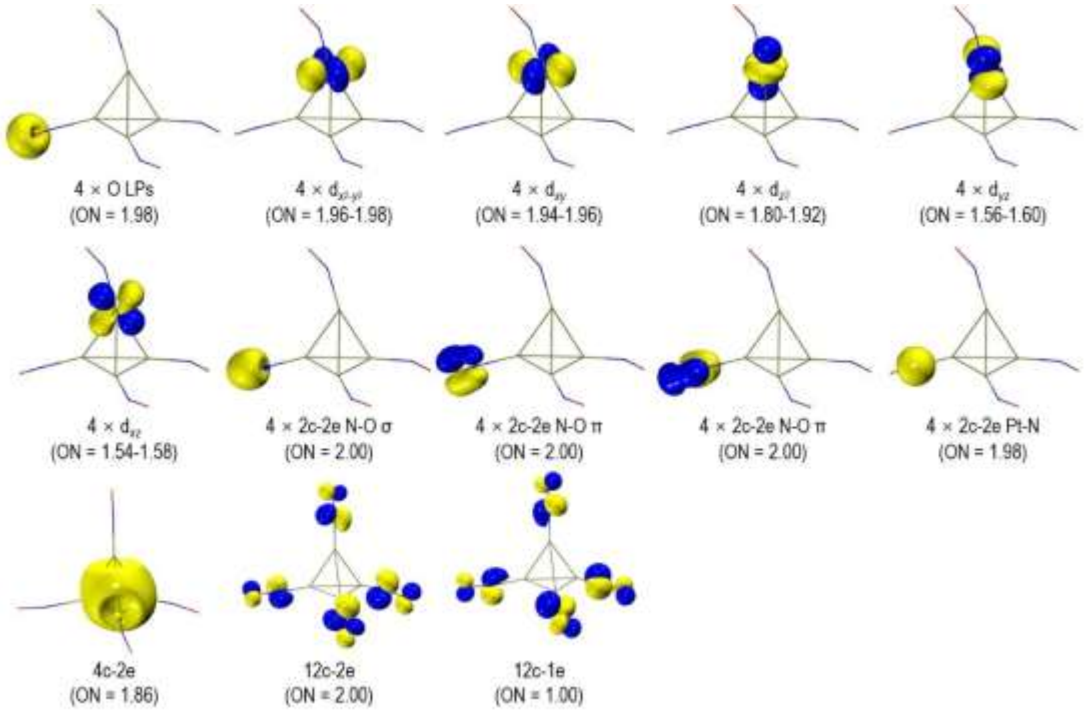

Fig. S34 AdNDP analysis of $Pt_4(NO)_4^-$. Only one of the same type of orbitals is given for clarity. ON denotes the occupancy number (|e|). The isovalues are set to 0.05 for all.

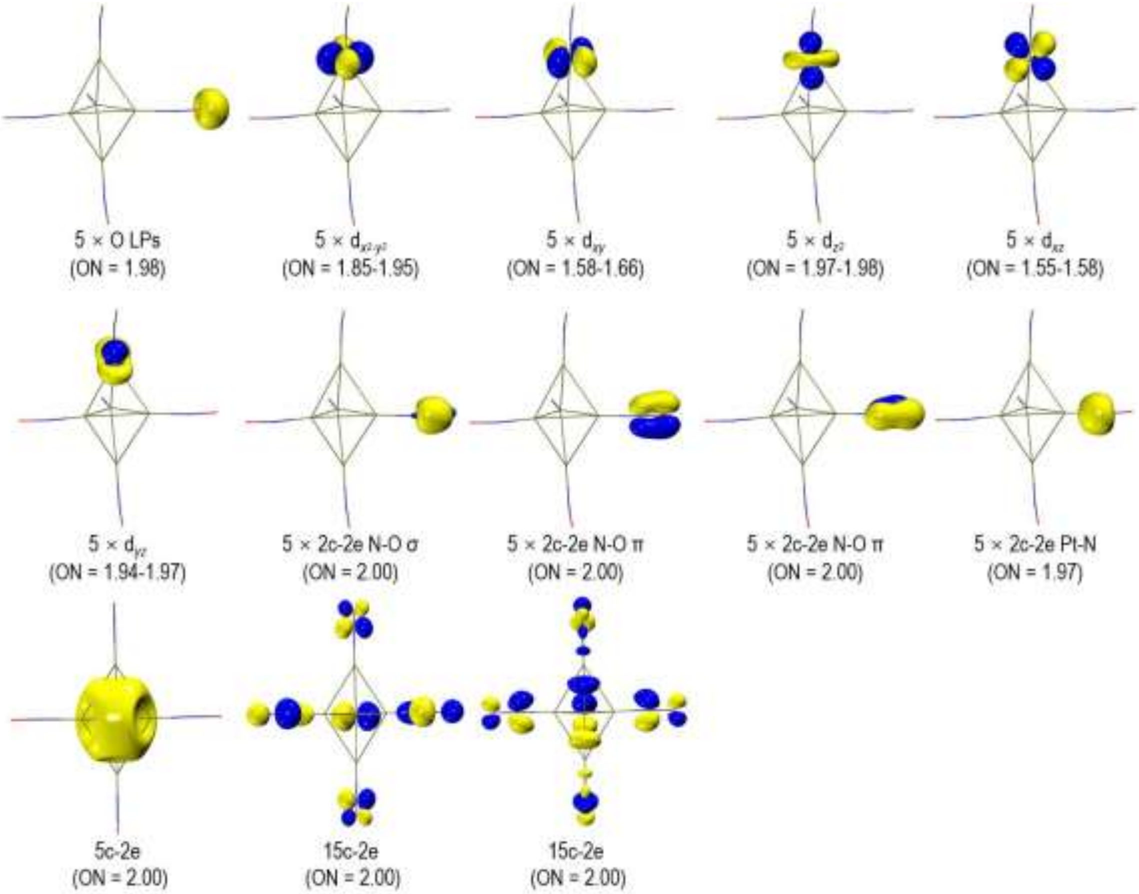

5 × O LPs (ON = 1.98)

5 × $d_{x^2-y^2}$ (ON = 1.85-1.95)

5 × d_{xy} (ON = 1.58-1.66)

5 × d_{z^2} (ON = 1.97-1.98)

5 × d_{xz} (ON = 1.55-1.58)

5 × d_{yz} (ON = 1.94-1.97)

5 × 2c-2e N-O σ (ON = 2.00)

5 × 2c-2e N-O π (ON = 2.00)

5 × 2c-2e N-O π (ON = 2.00)

5 × 2c-2e Pt-N (ON = 1.97)

5c-2e (ON = 2.00)

15c-2e (ON = 2.00)

15c-2e (ON = 2.00)

Fig. S35 AdNDP analysis of $Pt_5(NO)_5^-$. Only one of the same type of orbitals is given for clarity. ON denotes the occupancy number (|e|). The isovalues are set to 0.05 for all.

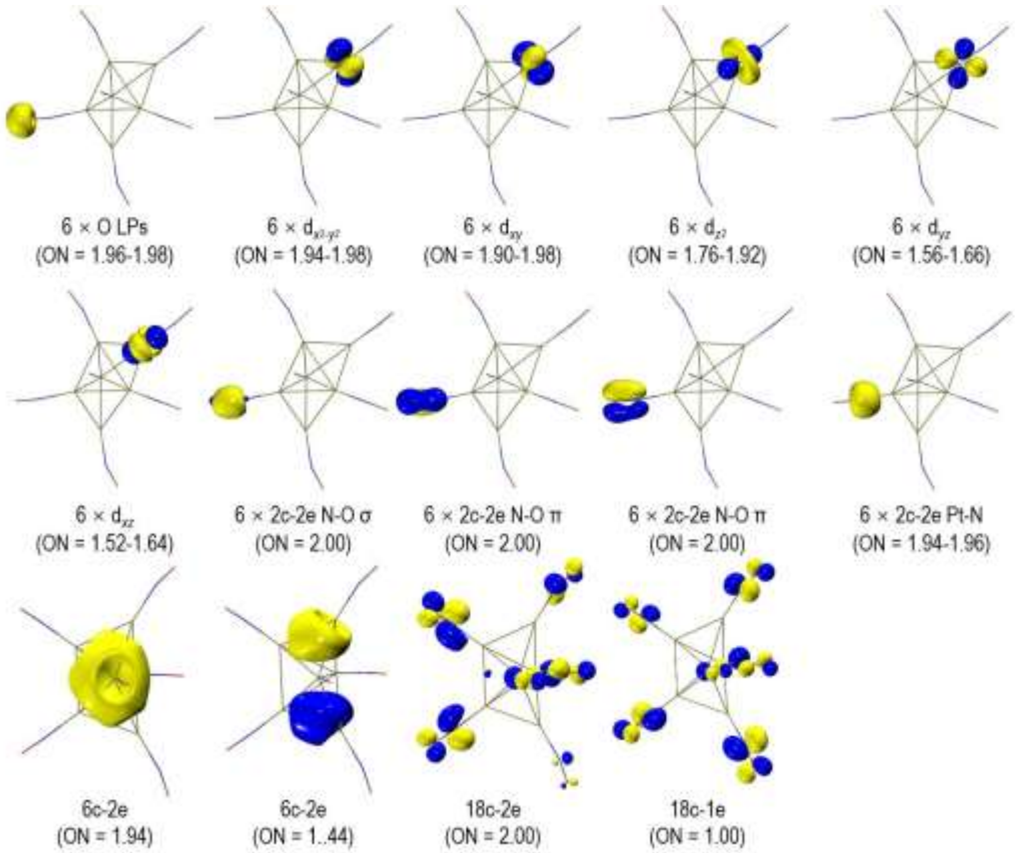

Fig. S36 AdNDP analysis of $Pt_6(NO)_6^-$. Only one of the same type of orbitals is given for clarity. ON denotes the occupancy number (|e|). The isovalues are set to 0.05 for all.

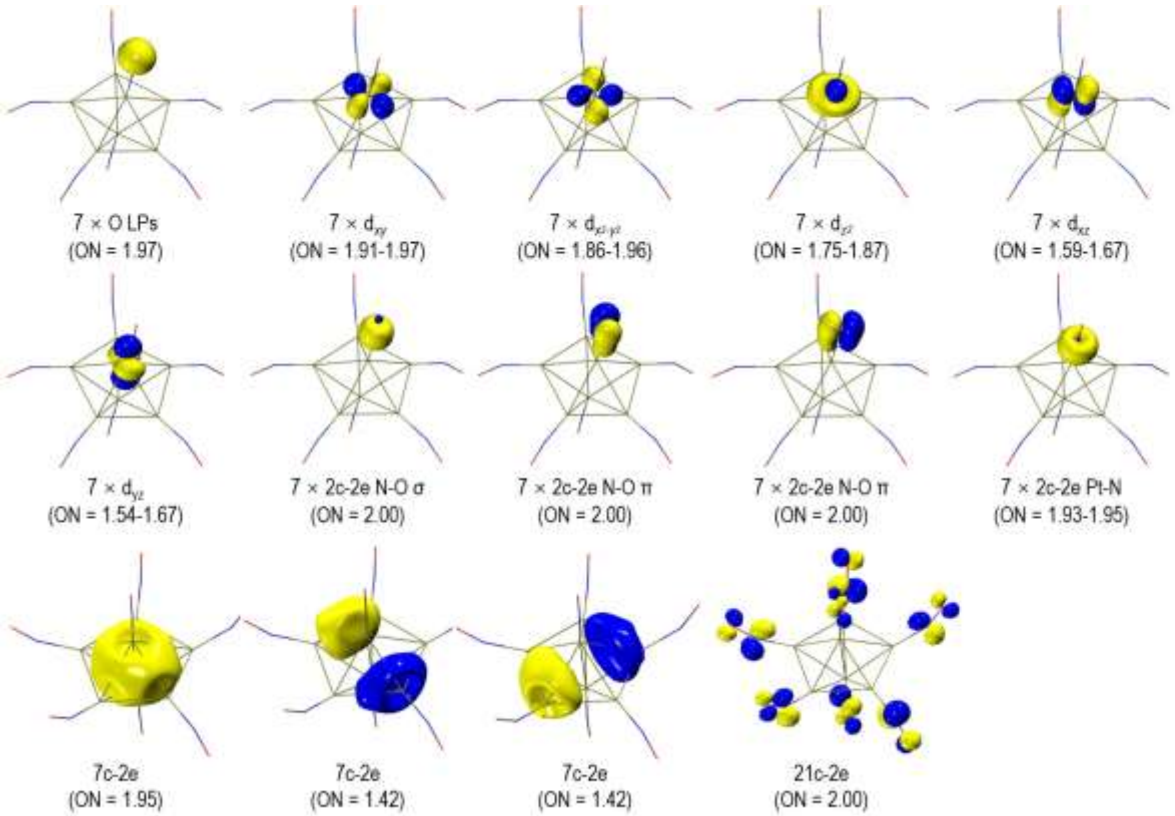

Fig. S37 AdNDP analysis of Pt$_7$(NO)$_7^-$. Only one of the same type of orbitals is given for clarity. ON denotes the occupancy number (|e|). The isovalues are set to 0.05 for all.

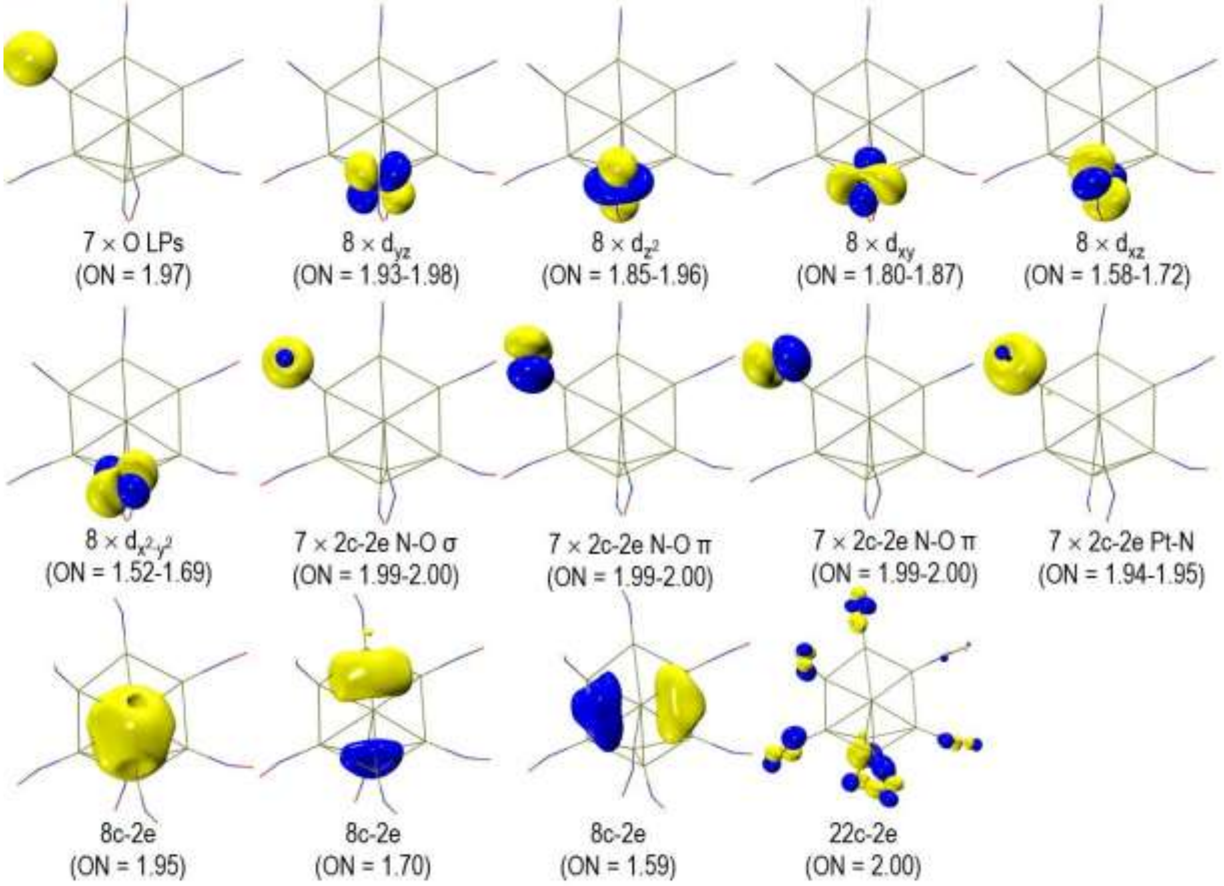

7 × O LPs (ON = 1.97)

8 × d_{yz} (ON = 1.93-1.98)

8 × d_{z^2} (ON = 1.85-1.96)

8 × d_{xy} (ON = 1.80-1.87)

8 × d_{xz} (ON = 1.58-1.72)

8 × $d_{x^2-y^2}$ (ON = 1.52-1.69)

7 × 2c-2e N-O σ (ON = 1.99-2.00)

7 × 2c-2e N-O π (ON = 1.99-2.00)

7 × 2c-2e N-O π (ON = 1.99-2.00)

7 × 2c-2e Pt-N (ON = 1.94-1.95)

8c-2e (ON = 1.95)

8c-2e (ON = 1.70)

8c-2e (ON = 1.59)

22c-2e (ON = 2.00)

Fig. S38 AdNDP analysis of Pt$_8$(NO)$_7^-$. Only one of the same type of orbitals is given for clarity. ON denotes the occupancy number (|e|). The isovalues are set to 0.05 for all.

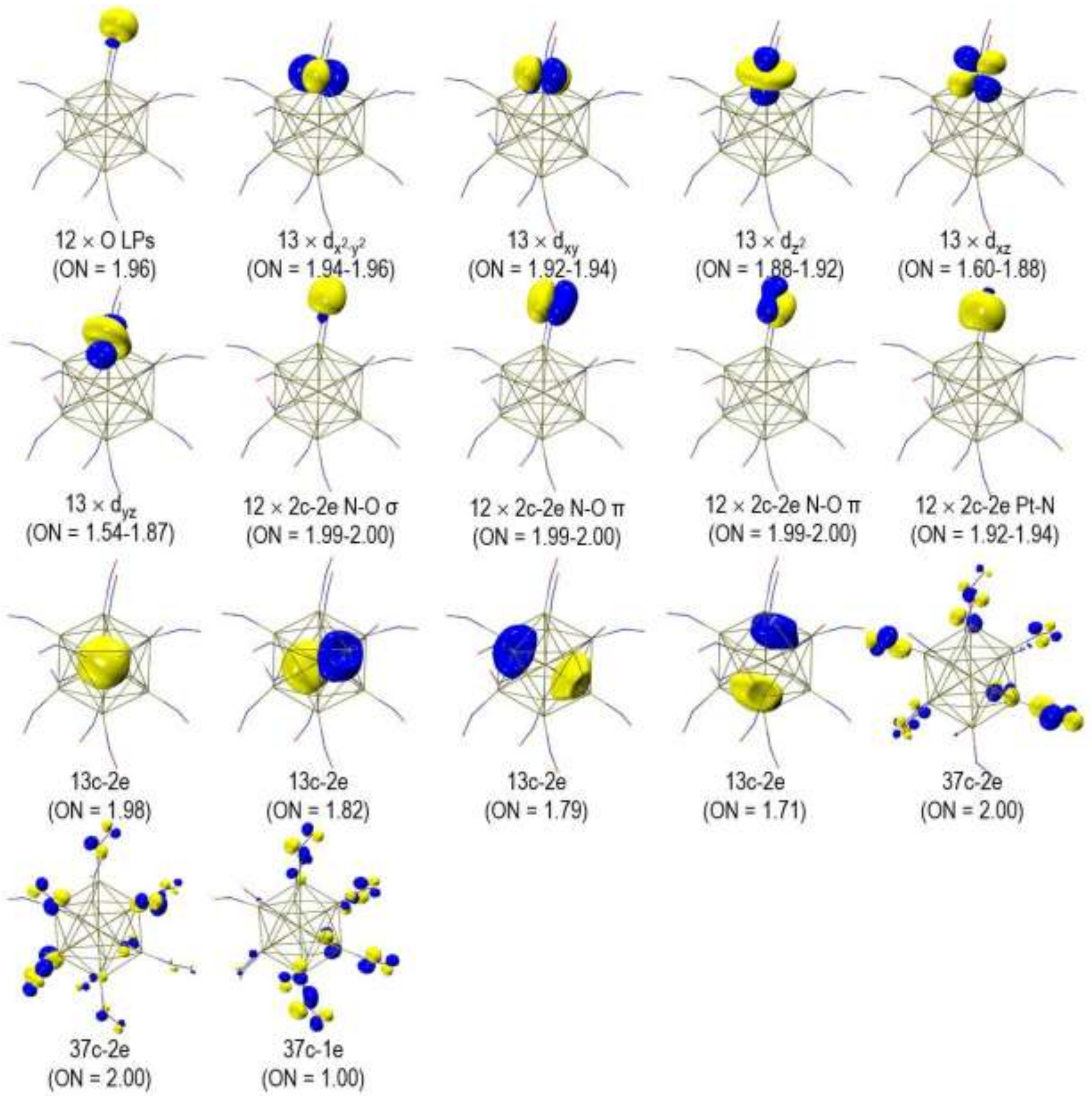

12 × O LPs (ON = 1.96)

13 × $d_{x^2-y^2}$ (ON = 1.94-1.96)

13 × d_{xy} (ON = 1.92-1.94)

13 × d_{z^2} (ON = 1.88-1.92)

13 × d_{xz} (ON = 1.60-1.88)

13 × d_{yz} (ON = 1.54-1.87)

12 × 2c-2e N-O σ (ON = 1.99-2.00)

12 × 2c-2e N-O π (ON = 1.99-2.00)

12 × 2c-2e N-O π (ON = 1.99-2.00)

12 × 2c-2e Pt-N (ON = 1.92-1.94)

13c-2e (ON = 1.98)

13c-2e (ON = 1.82)

13c-2e (ON = 1.79)

13c-2e (ON = 1.71)

37c-2e (ON = 2.00)

37c-2e (ON = 2.00)

37c-1e (ON = 1.00)

Fig. S39 AdNDP analysis of $Pt_{13}(NO)_{12}^{-}$. Only one of the same type of orbitals is given for clarity. ON denotes the occupancy number (|e|). The isovalues are set to 0.05 for all.

S7. DOS and molecular orbitals of the $Pt_n(NO)_m^{\pm}$

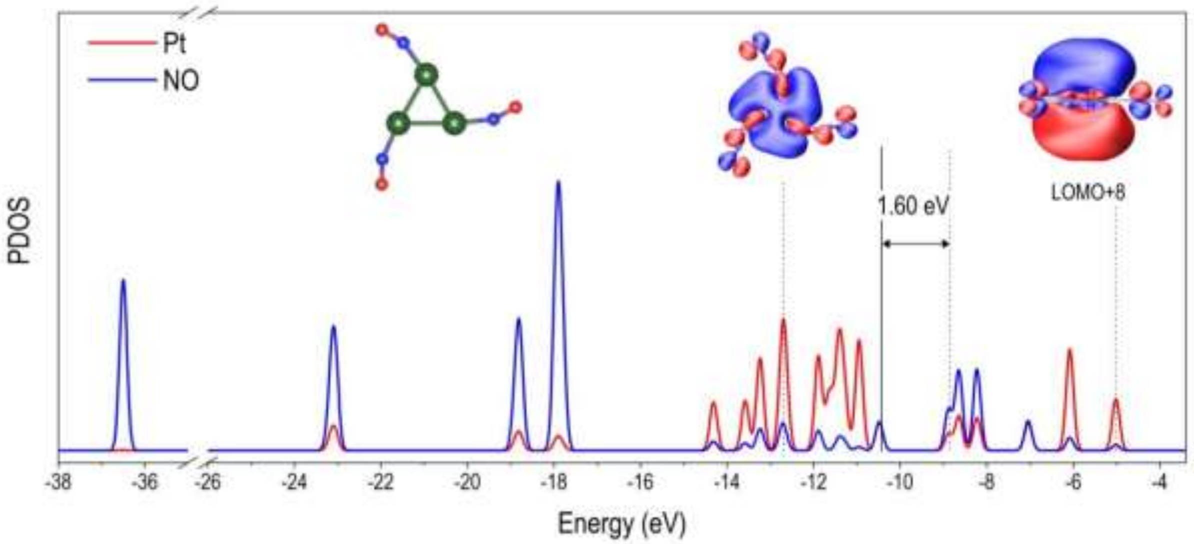

Fig. S40 Partial density of states and selected canonical molecular orbitals of $Pt_3(NO)_3^+$. The red and blue curves correspond to PDOS of Pt and NO respectively. The isovalues for orbitals are set to 0.02. Also labelled, is the HOMOLUMO gap.

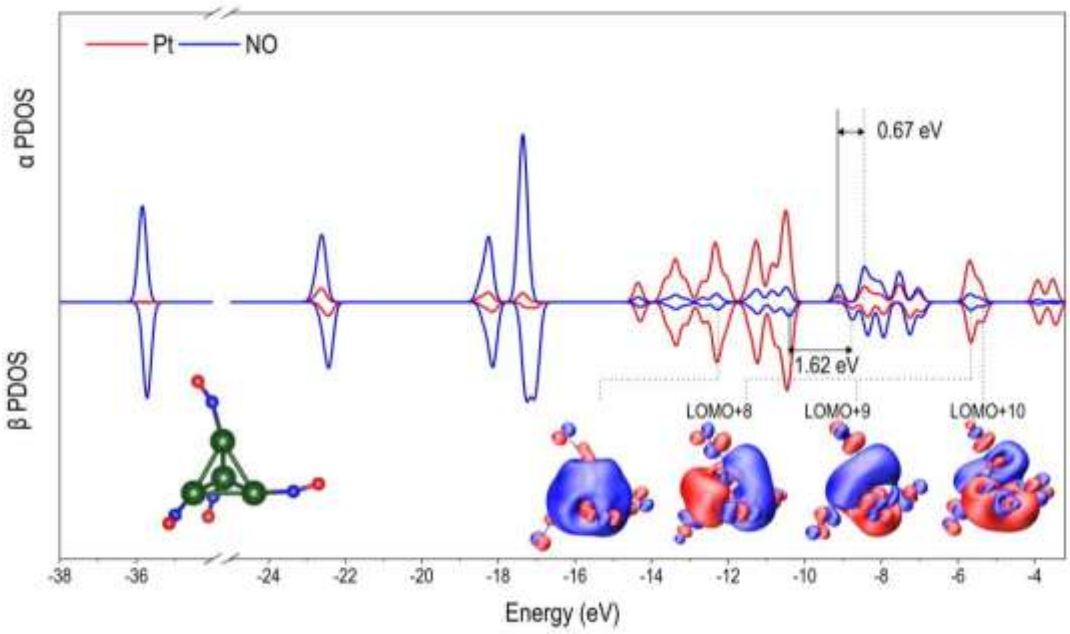

Fig. S41 Partial density of states and selected canonical molecular orbitals of $Pt_4(NO)_4^+$. The red and blue curves correspond to PDOS of Pt and NO respectively. The isovalues for orbitals are set to 0.02. Also labelled, is the HOMOLUMO gap.

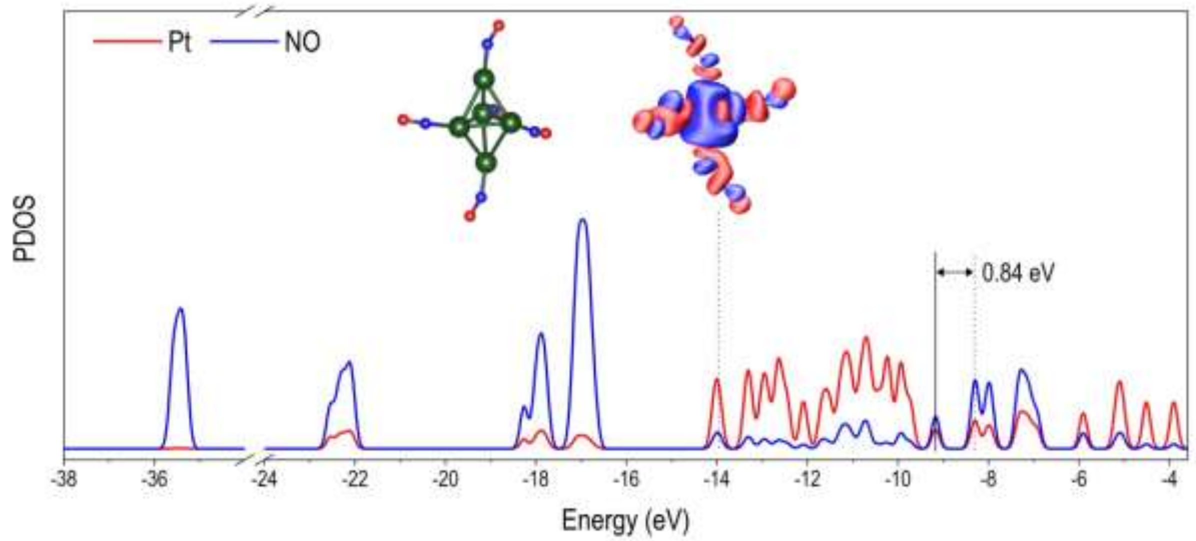

Fig. S42 Partial density of states and selected canonical molecular orbitals of $Pt_5(NO)_5^+$. The red and blue curves correspond to PDOS of Pt and NO respectively. The isovalues for orbitals are set to 0.02. Also labelled, is the HOMOLUMO gap.

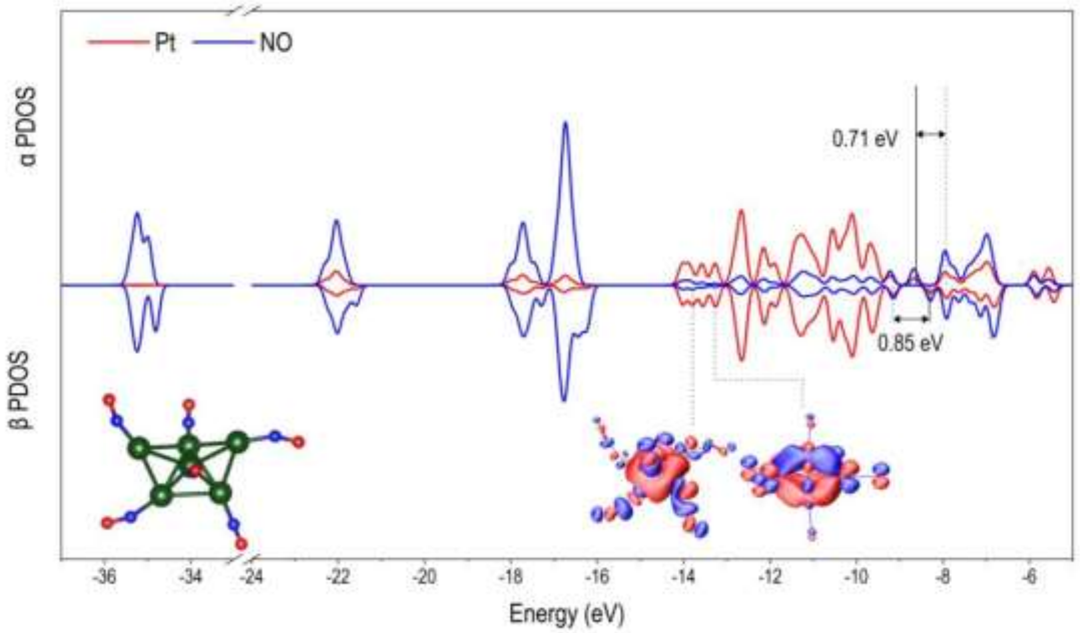

Fig. S43 Partial density of states and selected canonical molecular orbitals of $Pt_6(NO)_6^+$. The red and blue curves correspond to PDOS of Pt and NO respectively. The isovalues for orbitals are set to 0.02. Also labelled, is the HOMOLUMO gap.

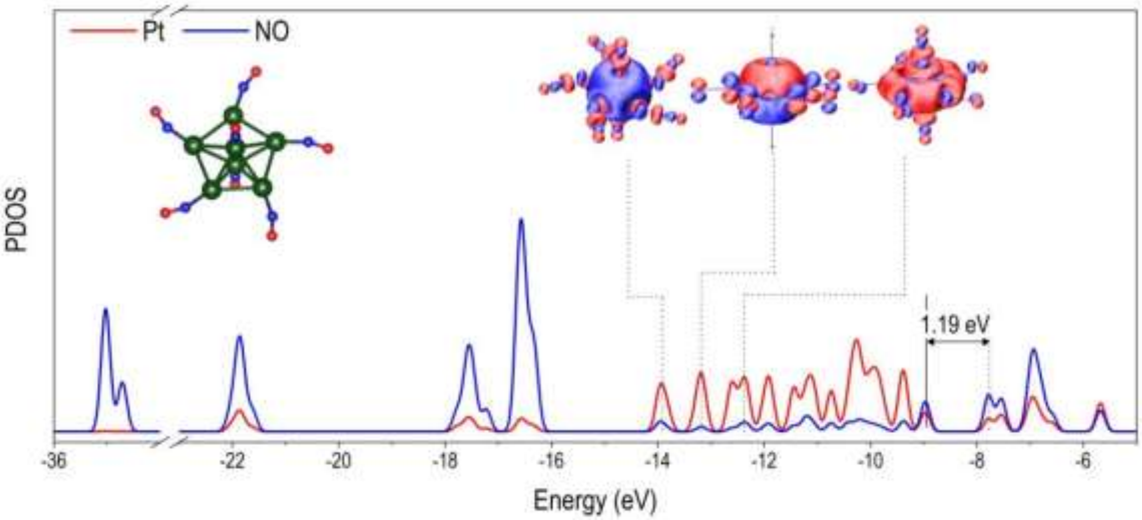

Fig. S44 Partial density of states and selected canonical molecular orbitals of $Pt_7(NO)_7^+$. The red and blue curves correspond to PDOS of Pt and NO respectively. The isovalues for orbitals are set to 0.02. Also labelled, is the HOMOLUMO gap.

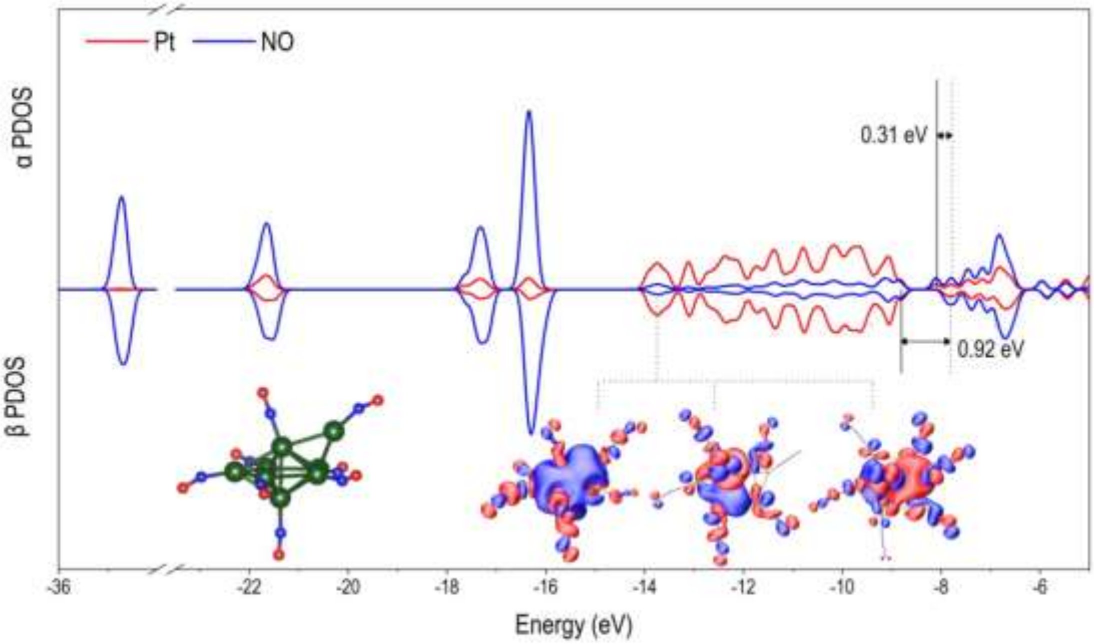

Fig. S45 Partial density of states and selected canonical molecular orbitals of $Pt_8(NO)_8^+$. The red and blue curves correspond to PDOS of Pt and NO respectively. The isovalues for orbitals are set to 0.02. Also labelled, is the HOMOLUMO gap.

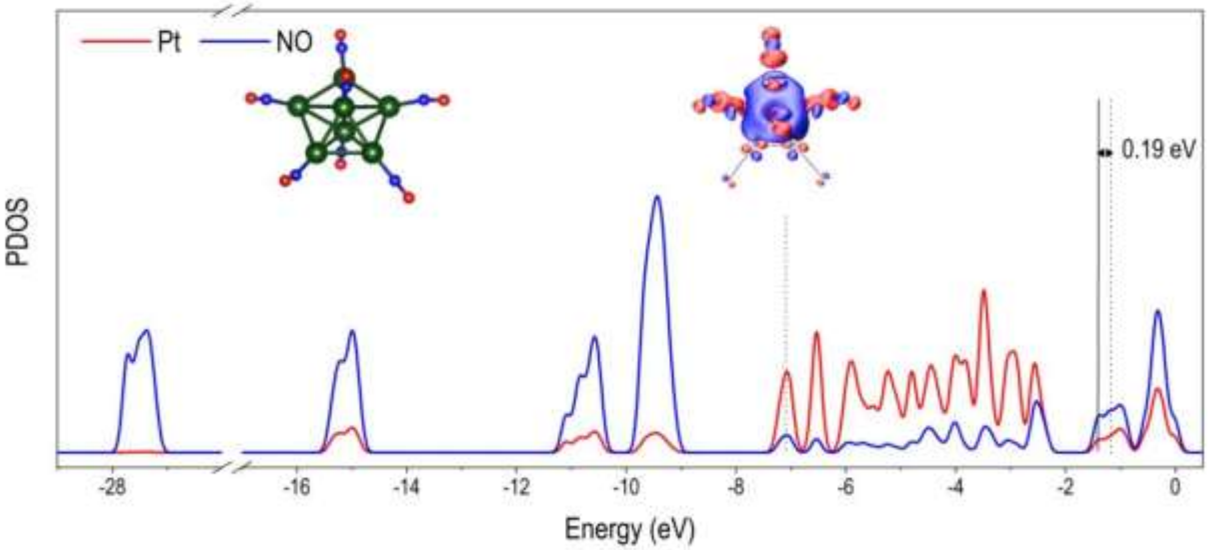

Fig. S46 Partial density of states and selected canonical molecular orbitals of $Pt_7(NO)_7^-$. The red and blue curves correspond to PDOS of Pt and NO respectively. The isovalues for orbitals are set to 0.02. Also labelled, is the HOMOLUMO gap.

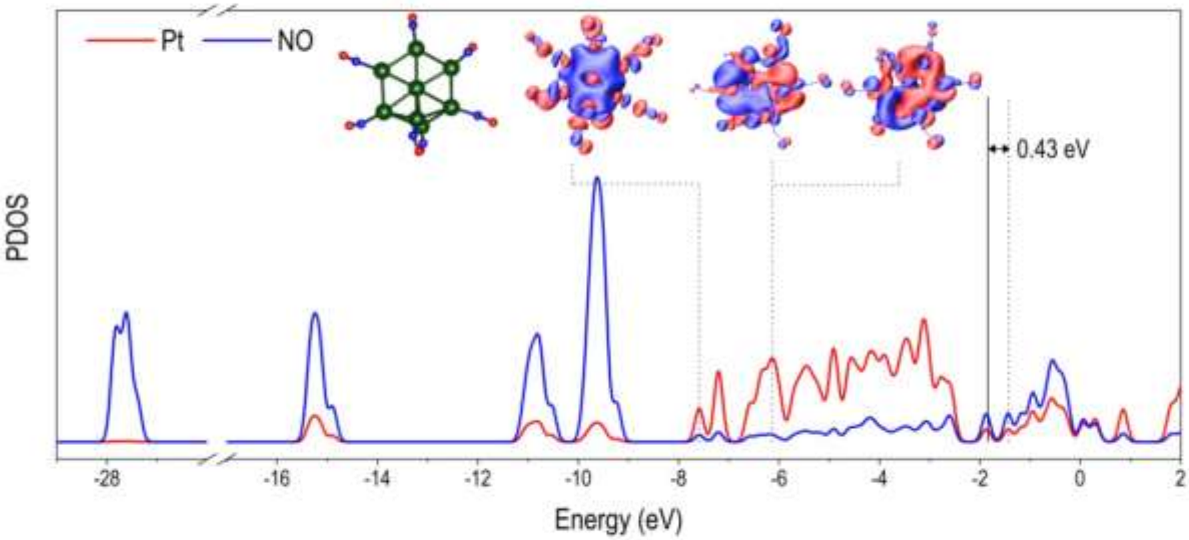

Fig. S47 Partial density of states and selected canonical molecular orbitals of $Pt_8(NO)_7^-$. The red and blue curves correspond to PDOS of Pt and NO respectively. The isovalues for orbitals are set to 0.02. Also labelled, is the HOMOLUMO gap.

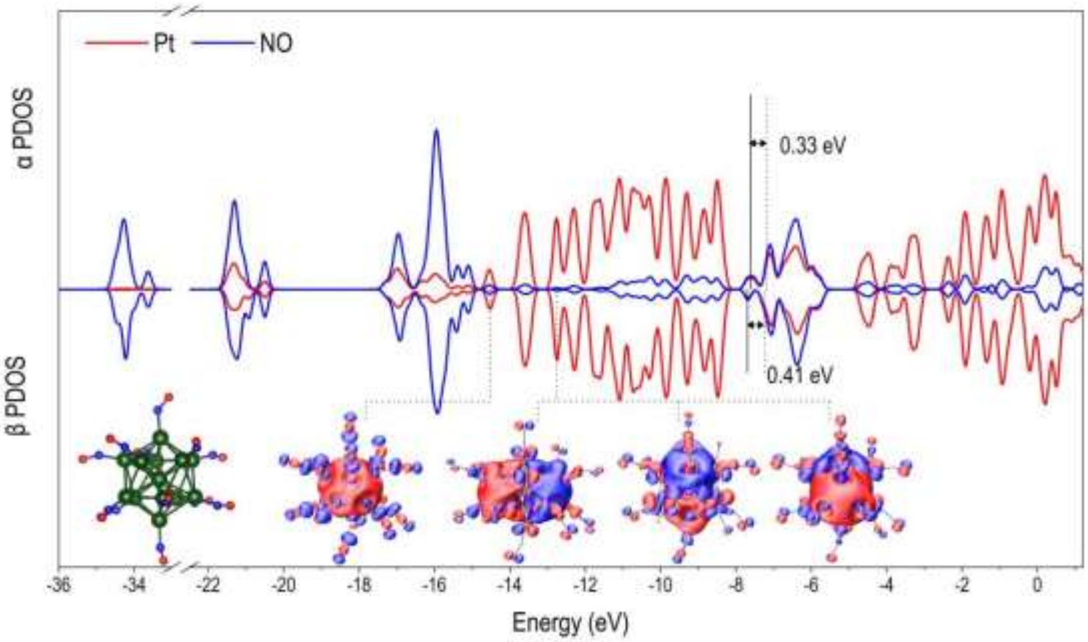

Fig. S48 Partial density of states and selected canonical molecular orbitals of $Pt_{13}(NO)_{12}^{+}$. The red and blue curves correspond to PDOS of Pt and NO respectively. The isovalues for orbitals are set to 0.02. Also labelled, is the HOMOLUMO gap.

S8. Geometric structures of $Rh_n(NO)_m^+$

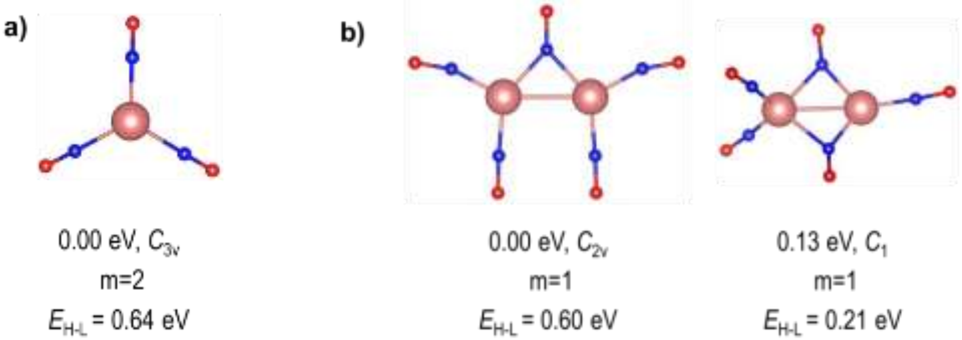

Fig. S49 Low-lying isomers of $Rh(NO)_3^+$ (a) and $Rh_2(NO)_5^+$ (b) with relative energies corrected by zero-point vibrations. Also labeled, are symmetry, spin multiplicity (m) and HOMO-LUMO gap (E_{H-L}).

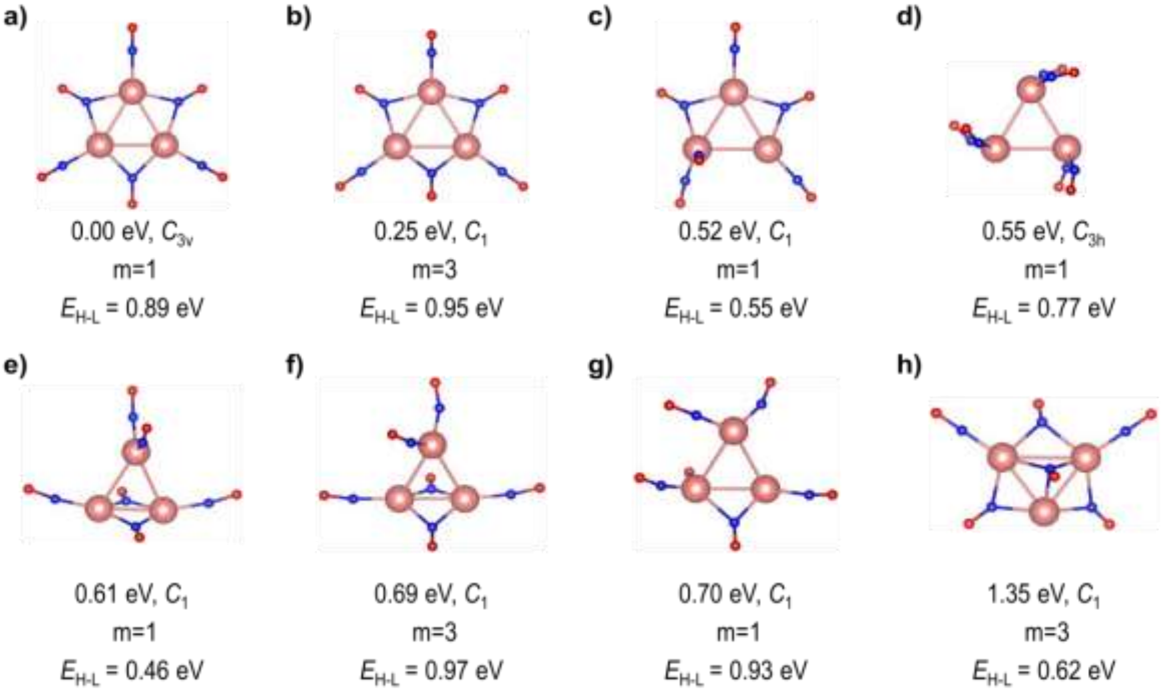

a) 0.00 eV, C_{3v}
m=1
$E_{\text{H-L}}$ = 0.89 eV

b) 0.25 eV, C_1
m=3
$E_{\text{H-L}}$ = 0.95 eV

c) 0.52 eV, C_1
m=1
$E_{\text{H-L}}$ = 0.55 eV

d) 0.55 eV, C_{3h}
m=1
$E_{\text{H-L}}$ = 0.77 eV

e) 0.61 eV, C_1
m=1
$E_{\text{H-L}}$ = 0.46 eV

f) 0.69 eV, C_1
m=3
$E_{\text{H-L}}$ = 0.97 eV

g) 0.70 eV, C_1
m=1
$E_{\text{H-L}}$ = 0.93 eV

h) 1.35 eV, C_1
m=3
$E_{\text{H-L}}$ = 0.62 eV

Fig. S50 Low-lying isomers of $Rh_3(NO)_6^+$ with relative energies corrected by zero-point vibrations. Also labeled, are symmetry, spin multiplicity (m) and HOMO-LUMO gap ($E_{\text{H-L}}$).

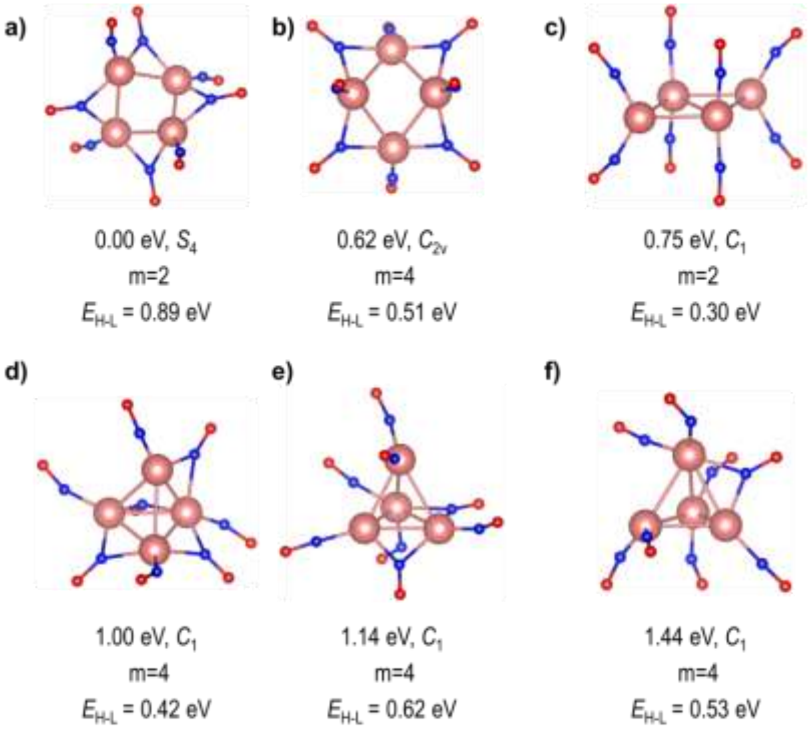

a) 0.00 eV, S_4
m=2
$E_{\text{H-L}}$ = 0.89 eV

b) 0.62 eV, C_{2v}
m=4
$E_{\text{H-L}}$ = 0.51 eV

c) 0.75 eV, C_1
m=2
$E_{\text{H-L}}$ = 0.30 eV

d) 1.00 eV, C_1
m=4
$E_{\text{H-L}}$ = 0.42 eV

e) 1.14 eV, C_1
m=4
$E_{\text{H-L}}$ = 0.62 eV

f) 1.44 eV, C_1
m=4
$E_{\text{H-L}}$ = 0.53 eV

Fig. S51 Low-lying isomers of $Rh_4(NO)_8^+$ with relative energies corrected by zero-point vibrations. Also labeled, are symmetry, spin multiplicity (m) and HOMO-LUMO gap ($E_{\text{H-L}}$).

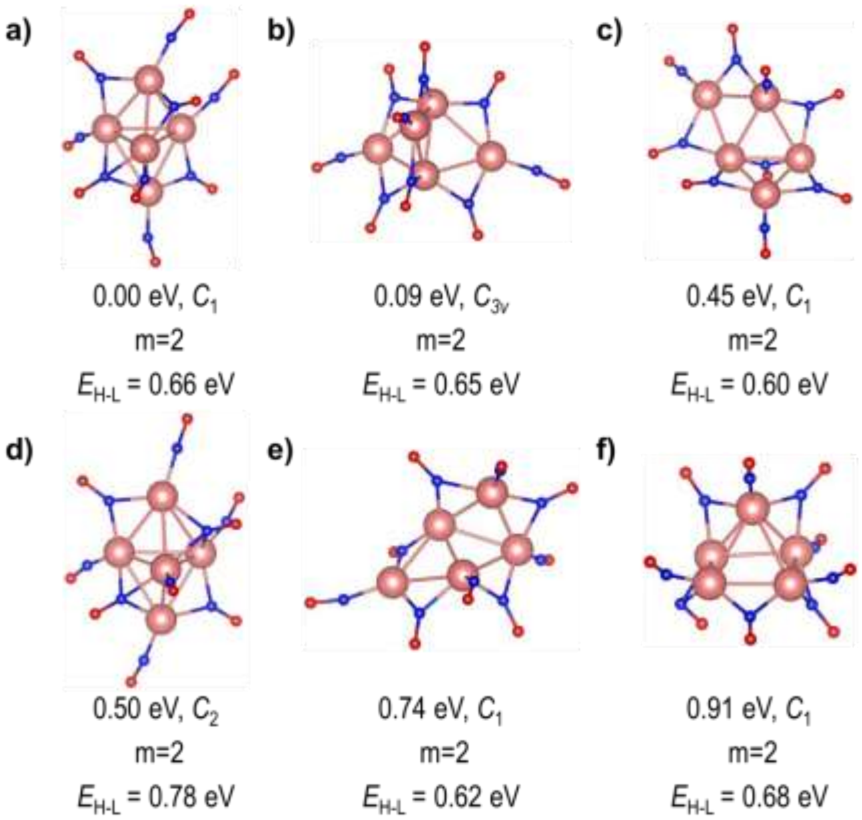

a) 0.00 eV, C_1, m=2, $E_{\text{H-L}}$ = 0.66 eV

b) 0.09 eV, C_{3v}, m=2, $E_{\text{H-L}}$ = 0.65 eV

c) 0.45 eV, C_1, m=2, $E_{\text{H-L}}$ = 0.60 eV

d) 0.50 eV, C_2, m=2, $E_{\text{H-L}}$ = 0.78 eV

e) 0.74 eV, C_1, m=2, $E_{\text{H-L}}$ = 0.62 eV

f) 0.91 eV, C_1, m=2, $E_{\text{H-L}}$ = 0.68 eV

Fig. S52 Low-lying isomers of $Rh_5(NO)_9^+$ with relative energies corrected by zero-point vibrations. Also labeled, are symmetry, spin multiplicity (m) and HOMO-LUMO gap ($E_{\text{H-L}}$).

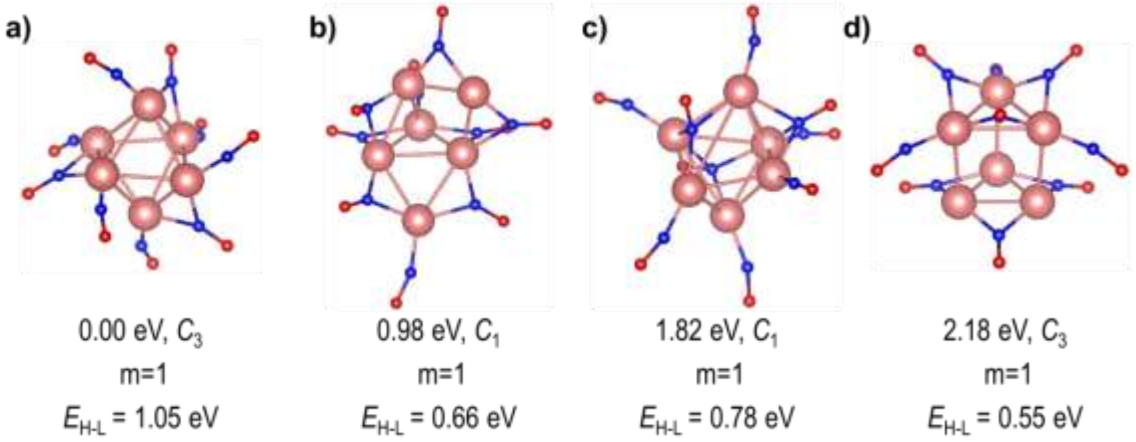

a) 0.00 eV, C_3, m=1, $E_{\text{H-L}}$ = 1.05 eV

b) 0.98 eV, C_1, m=1, $E_{\text{H-L}}$ = 0.66 eV

c) 1.82 eV, C_1, m=1, $E_{\text{H-L}}$ = 0.78 eV

d) 2.18 eV, C_3, m=1, $E_{\text{H-L}}$ = 0.55 eV

Fig. S53 Low-lying isomers of $Rh_6(NO)_9^+$ with relative energies corrected by zero-point vibrations. Also labeled, are symmetry, spin multiplicity (m) and HOMO-LUMO gap ($E_{\text{H-L}}$).

S9. AdNDP analysis of $Rh_n(NO)_m^+$

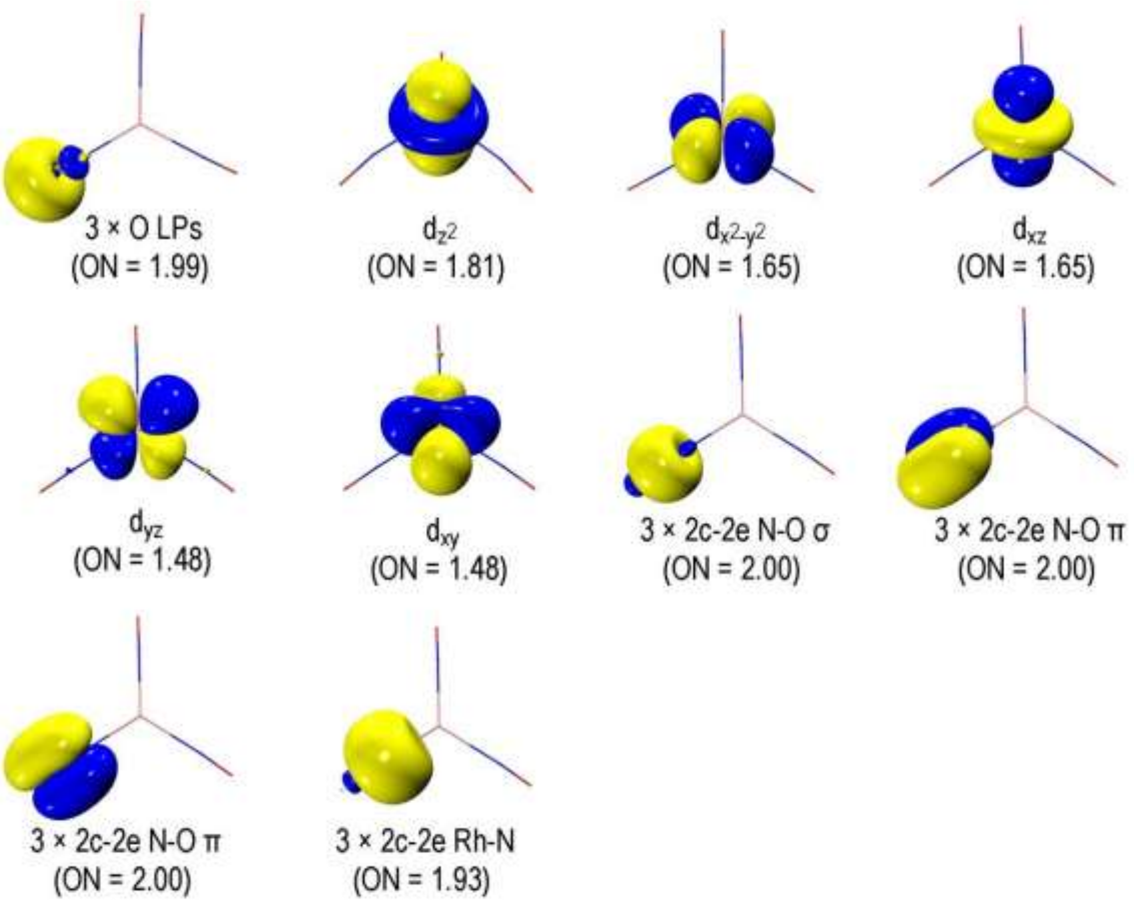

Fig. S54 AdNDP analysis of $Rh(NO)_3^{2+}$. Only one of the same type of orbitals is given for clarity. ON denotes the occupancy number (|e|). The isovalues are set to 0.05 for all.

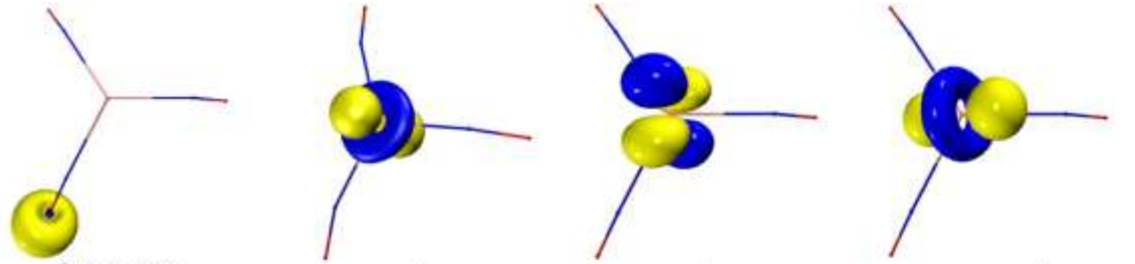

3 × O LPs (ON = 1.98)

d_{yz} (ON = 1.94)

$d_{x^2-y^2}$ (ON = 1.58-1.68)

d_{z^2} (ON = 1.58-1.68)

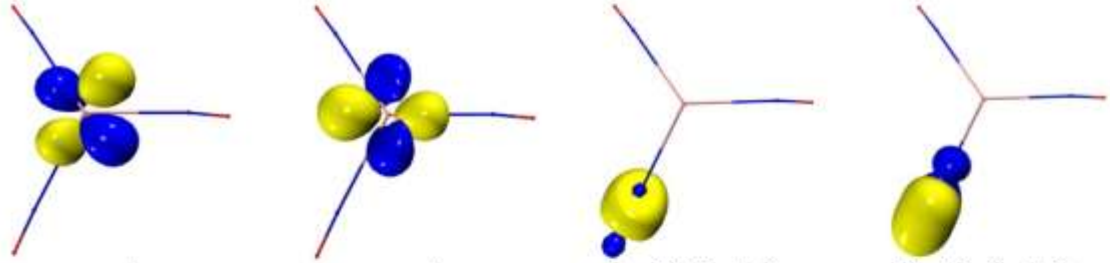

d_{xz} (ON = 1.40-1.48)

d_{xy} (ON = 1.40-1.48)

3 × 2c-2e N-O σ (ON = 2.00)

3 × 2c-2e N-O π (ON = 2.00)

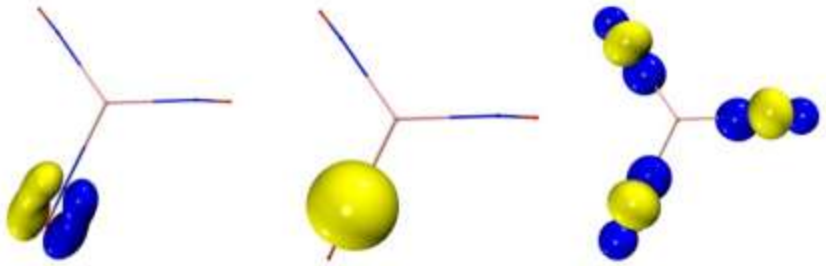

3 × 2c-2e N-O π (ON = 2.00)

3 × 2c-2e Rh-N σ (ON = 1.94)

7c-1e (ON = 2.00)

Fig. S55 AdNDP analysis of Rh(NO)$_3^+$. Only one of the same type of orbitals is given for clarity. ON denotes the occupancy number (|e|). The isovalues are set to 0.05 for all.

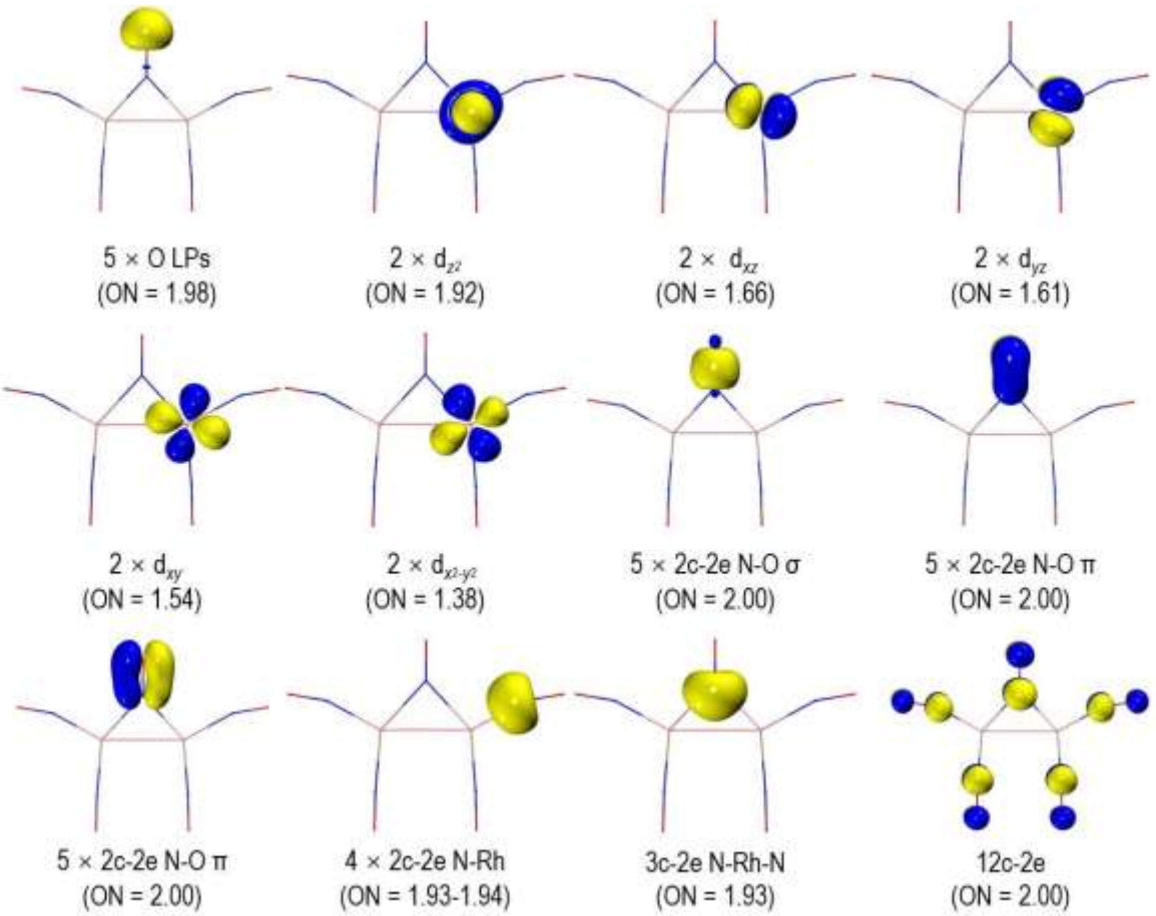

5 × O LPs (ON = 1.98)

2 × d_{z^2} (ON = 1.92)

2 × d_{xz} (ON = 1.66)

2 × d_{yz} (ON = 1.61)

2 × d_{xy} (ON = 1.54)

2 × $d_{x^2-y^2}$ (ON = 1.38)

5 × 2c-2e N-O σ (ON = 2.00)

5 × 2c-2e N-O π (ON = 2.00)

5 × 2c-2e N-O π (ON = 2.00)

4 × 2c-2e N-Rh (ON = 1.93-1.94)

3c-2e N-Rh-N (ON = 1.93)

12c-2e (ON = 2.00)

Fig. S56 AdNDP analysis of $Rh_2(NO)_5^+$. Only one of the same type of orbitals is given for clarity. ON denotes the occupancy number (|e|). The isovalues are set to 0.05 for all.

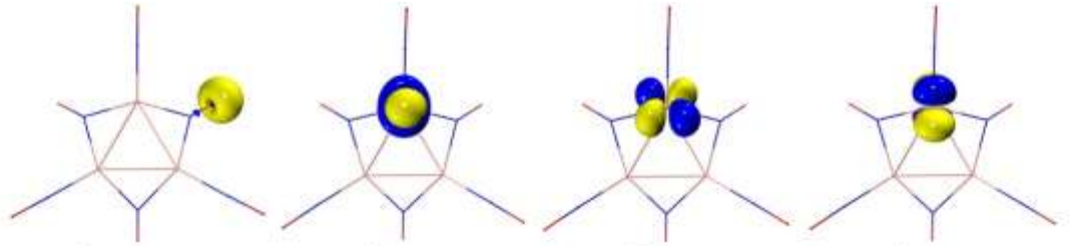

6 × O LPs (ON = 1.98)

$3 \times d_{z^2}$ (ON = 1.94)

$3 \times d_{xz}$ (ON = 1.67)

$3 \times d_{yz}$ (ON = 1.61)

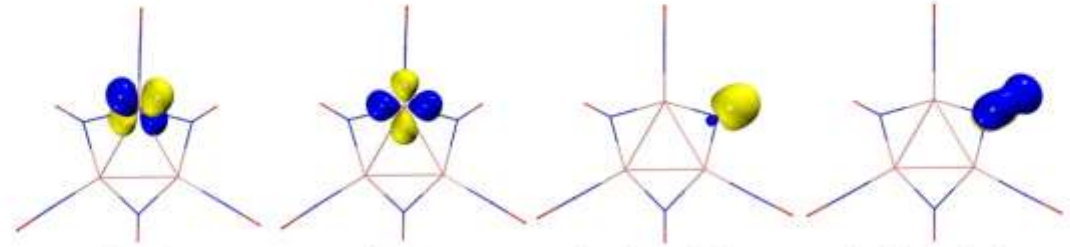

$3 \times d_{xy}$ (ON = 1.56)

$3 \times d_{x^2-y^2}$ (ON = 1.36)

6 × 2c-2e N-O σ (ON = 2.00)

6 × 2c-2e N-O π (ON = 2.00)

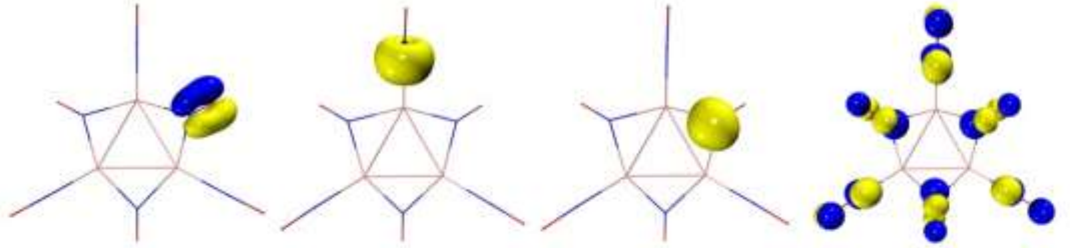

6 × 2c-2e N-O π (ON = 2.00)

3 × 2c-2e N-Rh (ON = 1.94)

3 × 3c-2e (ON = 1.93)

15c-2e (ON = 2.00)

Fig. S57 AdNDP analysis of $Rh_3(NO)_6^+$. Only one of the same type of orbitals is given for clarity. ON denotes the occupancy number (|e|). The isovalues are set to 0.05 for all.

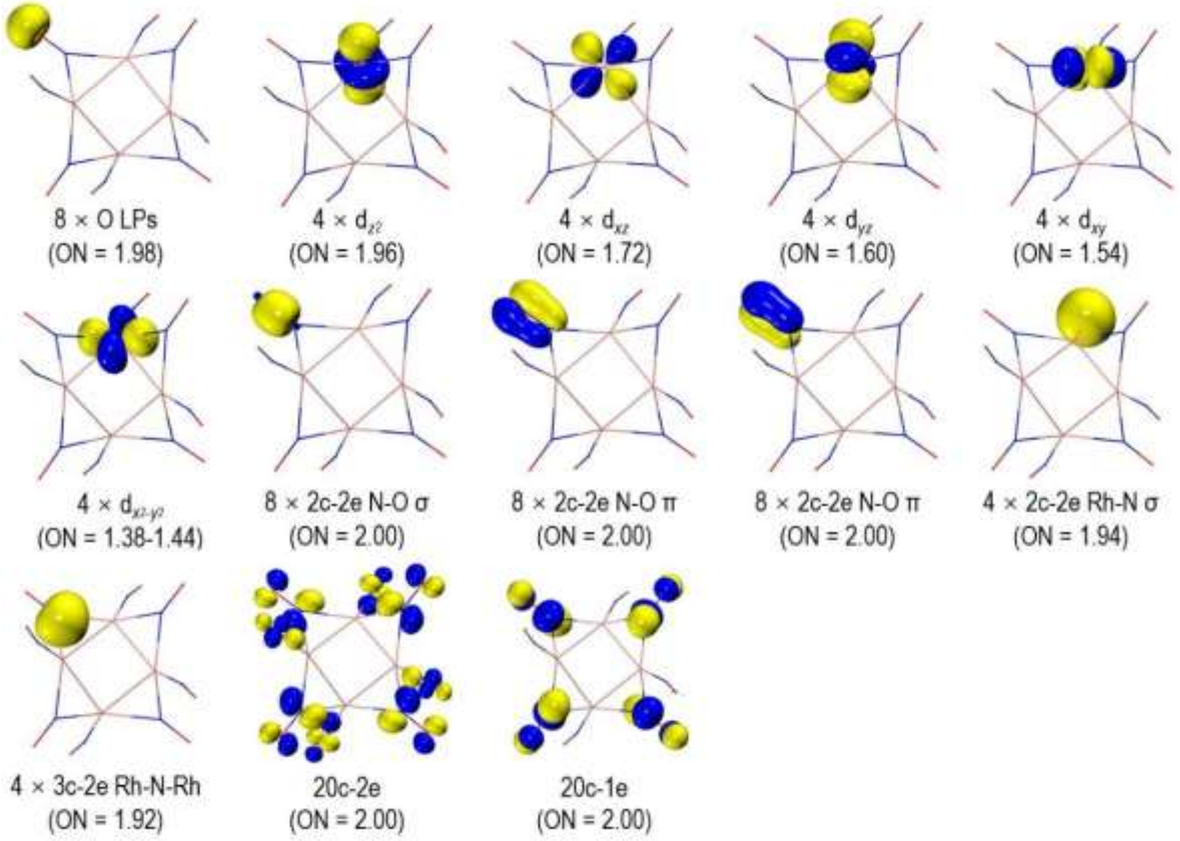

8 × O LPs (ON = 1.98)

4 × d_{z^2} (ON = 1.96)

4 × d_{xz} (ON = 1.72)

4 × d_{yz} (ON = 1.60)

4 × d_{xy} (ON = 1.54)

4 × $d_{x^2-y^2}$ (ON = 1.38-1.44)

8 × 2c-2e N-O σ (ON = 2.00)

8 × 2c-2e N-O π (ON = 2.00)

8 × 2c-2e N-O π (ON = 2.00)

4 × 2c-2e Rh-N σ (ON = 1.94)

4 × 3c-2e Rh-N-Rh (ON = 1.92)

20c-2e (ON = 2.00)

20c-1e (ON = 2.00)

Fig. S58 AdNDP analysis of $Rh_4(NO)_8^+$. Only one of the same type of orbitals is given for clarity. ON denotes the occupancy number (|e|). The isovalues are set to 0.05 for all.

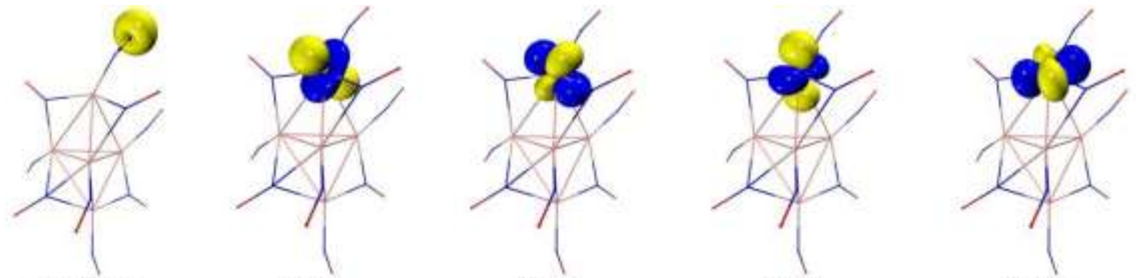

9 × O LPs (ON = 1.98)

5 × d_{z^2} (ON = 1.86-1.92)

5 × d_{xz} (ON = 1.68-1.88)

5 × d_{yz} (ON = 1.56-1.62)

5 × d_{xy} (ON = 1.52-1.58)

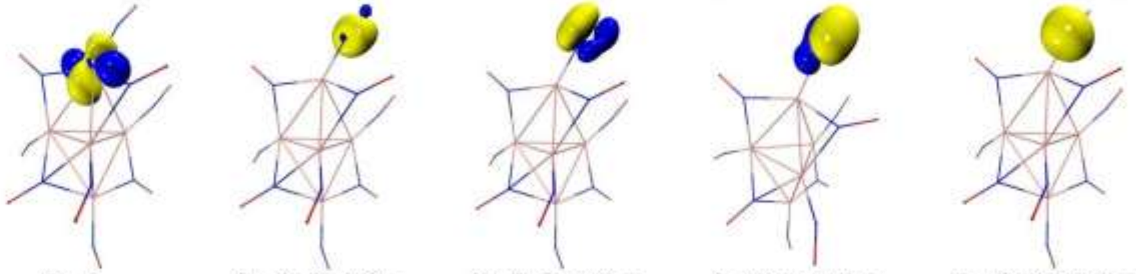

5 × $d_{x^2-y^2}$ (ON = 1.34-1.42)

9 × 2c-2e N-O σ (ON = 2.00)

9 × 2c-2e N-O π (ON = 2.00)

9 × 2c-2e N-O π (ON = 2.00)

5 × 2c-2e Rh-N σ (ON = 1.92-1.94)

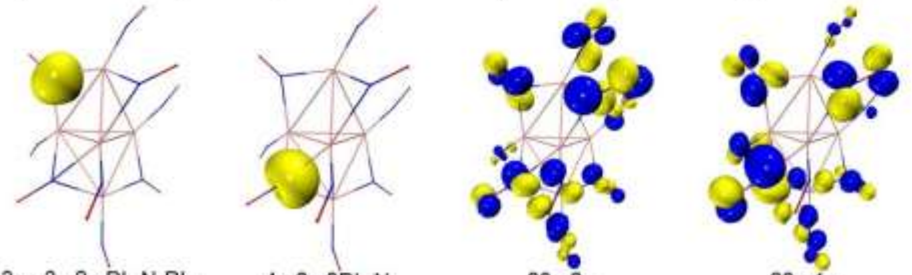

3 × 3c-2e Rh-N-Rh (ON = 1.90)

4c-2e 3Rh-N (ON = 1.92)

23c-2e (ON = 2.00)

23c-1e (ON = 2.00)

Fig. S59 AdNDP analysis of $Rh_5(NO)_9^+$. Only one of the same type of orbitals is given for clarity. ON denotes the occupancy number (|e|). The isovalues are set to 0.05 for all.

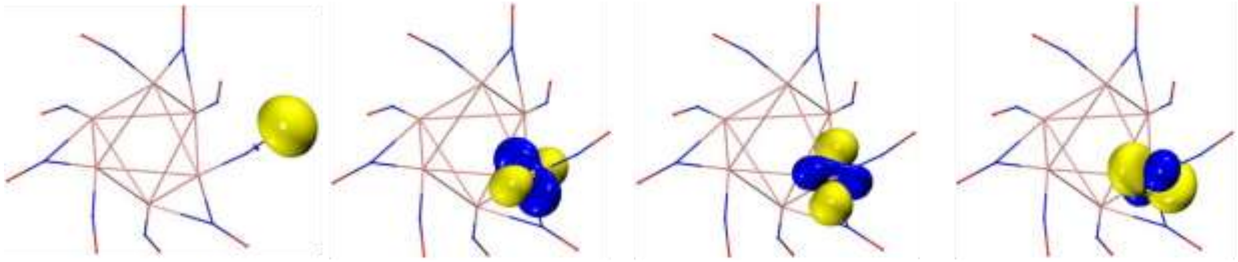

9 × O LPs (ON = 1.97-1.98)

$6 \times d_{xz}$ (ON = 1.82-1.85)

$6 \times d_{z^2}$ (ON = 1.71-1.77)

$6 \times d_{x^2-y^2}$ (ON = 1.62-1.64)

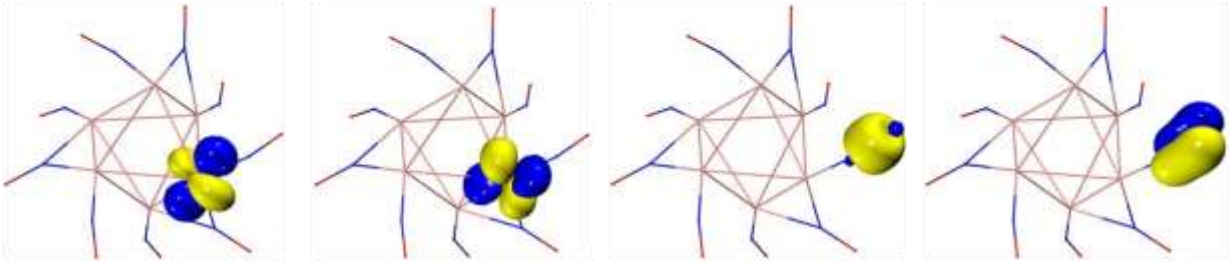

$6 \times d_{yz}$ (ON = 1.57-1.59)

$6 \times d_{xy}$ (ON = 1.40-1.45)

9 × 2c-2e N-O σ (ON = 2.00)

9 × 2c-2e N-O π (ON = 2.00)

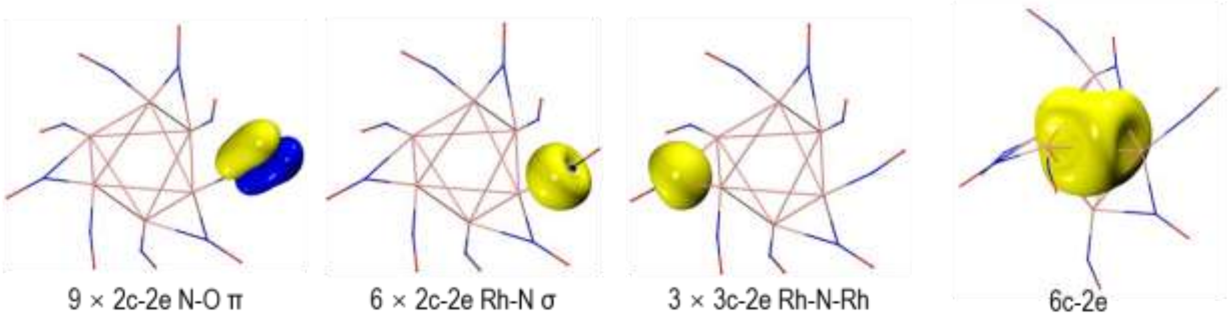

9 × 2c-2e N-O π (ON = 2.00)

6 × 2c-2e Rh-N σ (ON = 1.91-1.93)

3 × 3c-2e Rh-N-Rh (ON = 1.90)

6c-2e (ON = 1.58)

Fig. S60 AdNDP analysis of $Rh_6(NO)_9^+$. Only one of the same type of orbitals is given for clarity. ON denotes the occupancy number (|e|). The isovalues are set to 0.05 for all.

In $Rh_n(NO)_m^+$ clusters, the delocalized orbitals are primarily composed of the anti-bonding π orbitals of the NO molecule, leading to the full occupation of the five d-type lone pairs on the Rh atoms. Unlike the aforementioned small $Rh_n(CO)_m^+$, here in the $Rh_n(NO)_m^+$ clusters the NO ligands demonstrate considerable electron delocalization due to the participation of the half-filled antibonding *π orbitals along the molecule axis. For clusters with $n \leq 5$, $Rh_n(NO)_m^+$ predominantly demonstrates π-electron delocalization with almost negligible participation of the metal. However, for $n \geq 6$, such as $Rh_6(CO)_{16}^+$, the electrons exhibit increased delocalization across the metal atoms, resulting in a unique delocalized electron configuration that signifies superatomic feature and aromaticity. This aligns with the experimental observation, signifying adaptive accommodation of π-electron delocalization and superatomic electron delocalization in such metal cluster complexes.

S10. Geometric structures of Rh$_n$(CO)$_m$$^+$

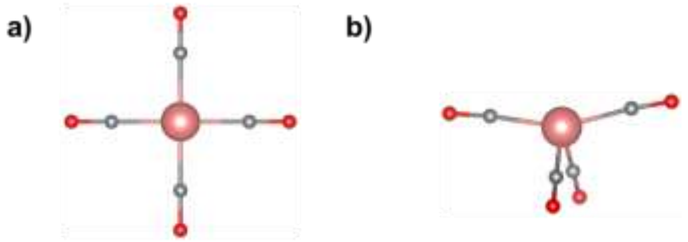

a) 0.00 eV, D_{4h}
m=1
$E_{H\text{-}L}$ = 2.40 eV

b) 1.55 eV, C_{2v}
m=3
$E_{H\text{-}L}$ = 3.53 eV

Fig. S561 Low-lying isomers of $Rh(CO)_4^+$ with relative energies corrected by zero-point vibrations. Also labeled, are symmetry, spin multiplicity (m) and HOMO-LUMO gap ($E_{H\text{-}L}$).

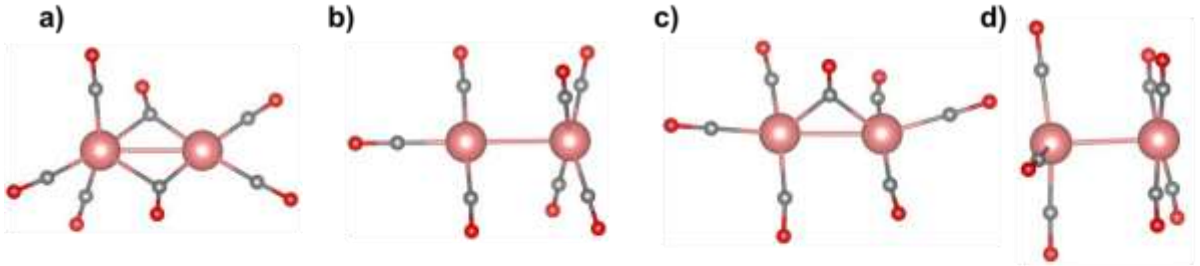

a) 0.00 eV, C_s
m=2
$E_{H\text{-}L}$ = 1.71 eV

b) 0.0022 eV, C_1
m=2
$E_{H\text{-}L}$ = 1.92 eV

c) 0.06 eV, C_2
m=2
$E_{H\text{-}L}$ = 1.45 eV

d) 1.59 eV, C_1
m=4
$E_{H\text{-}L}$ = 1.97 eV

Fig. S62 Low-lying isomers of $Rh_2(CO)_7^+$ with relative energies corrected by zero-point vibrations. Also labeled, are symmetry, spin multiplicity (m) and HOMO-LUMO gap ($E_{H\text{-}L}$).

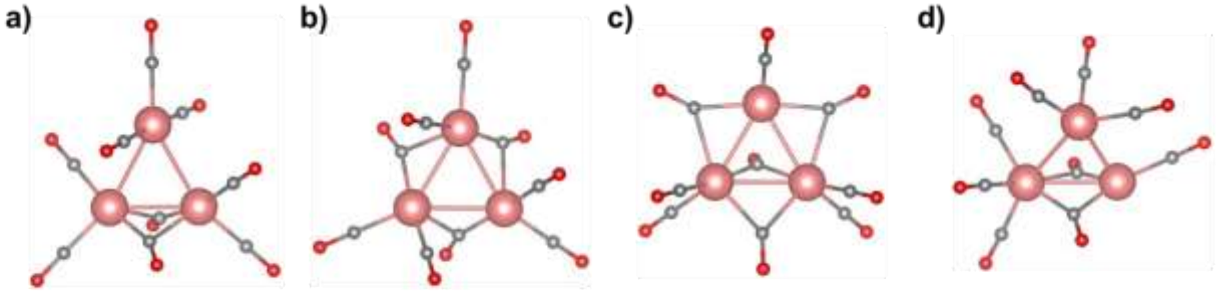

a) 0.00 eV, C_2
m=1
$E_{H\text{-}L}$ = 1.82 eV

b) 0.06 eV, C_3
m=1
$E_{H\text{-}L}$ = 1.97 eV

c) 1.30 eV, C_1
m=3
$E_{H\text{-}L}$ = 2.19 eV

d) 1.60 eV, C_1
m=3
$E_{H\text{-}L}$ = 1.60 eV

Fig. S63 Low-lying isomers of $Rh_3(CO)_9^+$ with relative energies corrected by zero-point vibrations. Also labeled, are symmetry, spin multiplicity (m) and HOMO-LUMO gap ($E_{H\text{-}L}$).

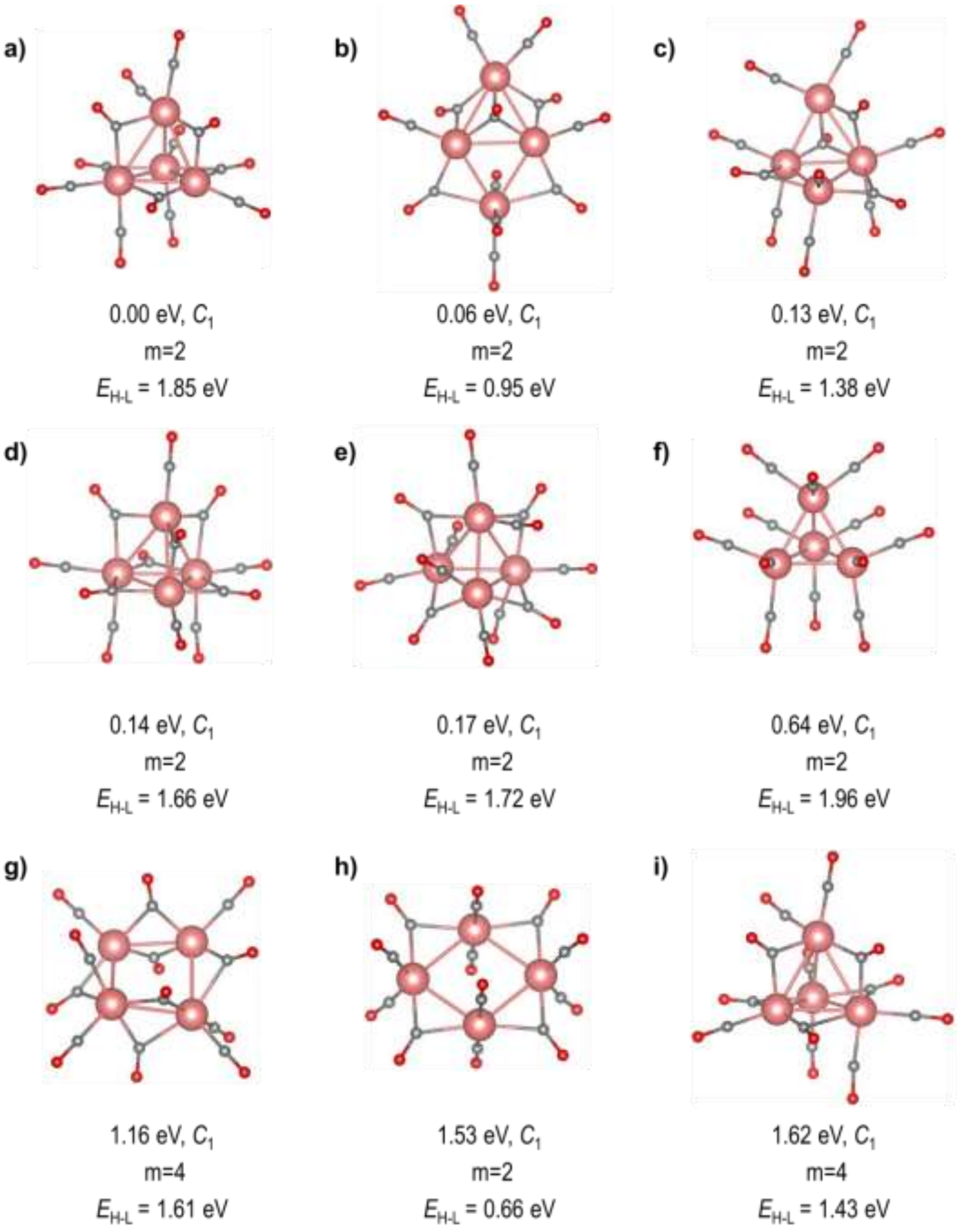

a) 0.00 eV, C_1
m=2
$E_{\text{H-L}}$ = 1.85 eV

b) 0.06 eV, C_1
m=2
$E_{\text{H-L}}$ = 0.95 eV

c) 0.13 eV, C_1
m=2
$E_{\text{H-L}}$ = 1.38 eV

d) 0.14 eV, C_1
m=2
$E_{\text{H-L}}$ = 1.66 eV

e) 0.17 eV, C_1
m=2
$E_{\text{H-L}}$ = 1.72 eV

f) 0.64 eV, C_1
m=2
$E_{\text{H-L}}$ = 1.96 eV

g) 1.16 eV, C_1
m=4
$E_{\text{H-L}}$ = 1.61 eV

h) 1.53 eV, C_1
m=2
$E_{\text{H-L}}$ = 0.66 eV

i) 1.62 eV, C_1
m=4
$E_{\text{H-L}}$ = 1.43 eV

Fig. S64 Low-lying isomers of $Rh_4(CO)_{12}^+$ with relative energies corrected by zero-point vibrations. Also labeled, are symmetry, spin multiplicity (m) and HOMO-LUMO gap ($E_{\text{H-L}}$).

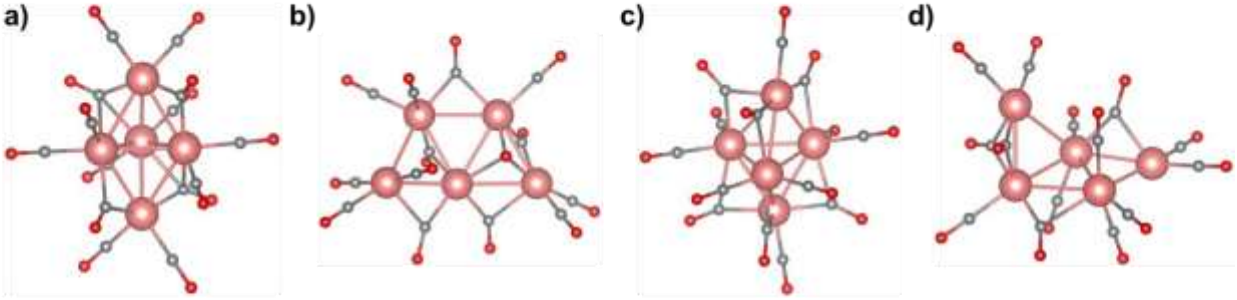

a) 0.00 eV, C_1
m=1
$E_{\text{H-L}}$ = 1.86 eV

b) 0.51 eV, C_2
m=1
$E_{\text{H-L}}$ = 1.36 eV

c) 0.62 eV, C_1
m=1
$E_{\text{H-L}}$ = 1.17 eV

d) 1.12 eV, C_1
m=1
$E_{\text{H-L}}$ = 1.36 eV

Fig. S65 Low-lying isomers of $Rh_5(CO)_{14}^+$ with relative energies corrected by zero-point vibrations. Also labeled, are symmetry, spin multiplicity (m) and HOMO-LUMO gap ($E_{\text{H-L}}$).

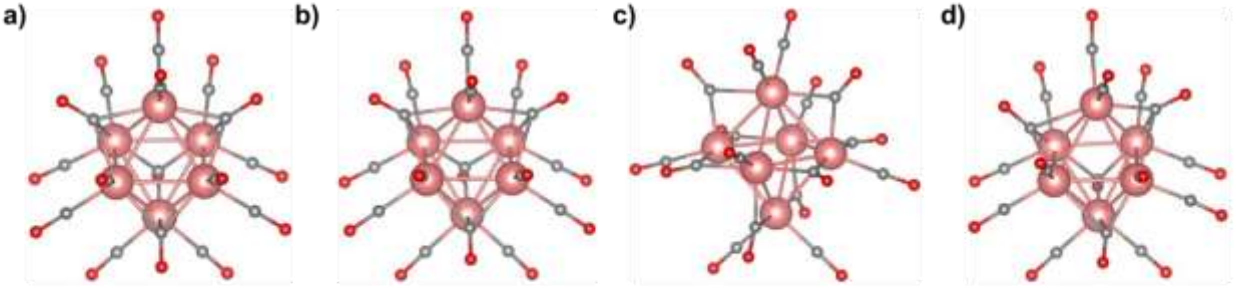

a) 0.00 eV, C_1
m=2
$E_{\text{H-L}}$ = 1.86 eV

b) 0.00046 eV, C_{3v}
m=2
$E_{\text{H-L}}$ = 1.87 eV

c) 1.26 eV, C_1
m=2
$E_{\text{H-L}}$ = 0.83 eV

d) 1.71 eV, C_1
m=4
$E_{\text{H-L}}$ = 0.50 eV

Fig. S66 Low-lying isomers of $Rh_6(CO)_{16}^+$ with relative energies corrected by zero-point vibrations. Also labeled, are symmetry, spin multiplicity (m) and HOMO-LUMO gap ($E_{\text{H-L}}$).

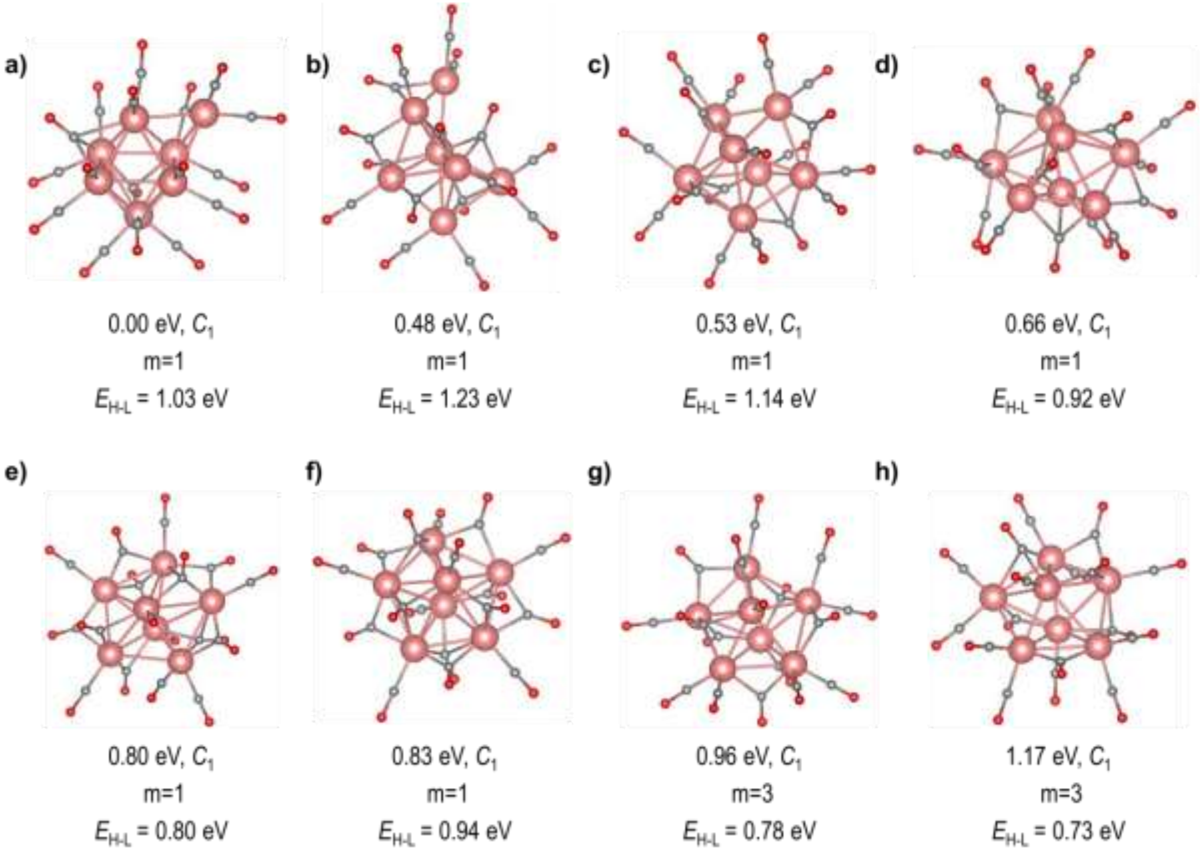

a) 0.00 eV, C_1
m=1
$E_{\text{H-L}}$ = 1.03 eV

b) 0.48 eV, C_1
m=1
$E_{\text{H-L}}$ = 1.23 eV

c) 0.53 eV, C_1
m=1
$E_{\text{H-L}}$ = 1.14 eV

d) 0.66 eV, C_1
m=1
$E_{\text{H-L}}$ = 0.92 eV

e) 0.80 eV, C_1
m=1
$E_{\text{H-L}}$ = 0.80 eV

f) 0.83 eV, C_1
m=1
$E_{\text{H-L}}$ = 0.94 eV

g) 0.96 eV, C_1
m=3
$E_{\text{H-L}}$ = 0.78 eV

h) 1.17 eV, C_1
m=3
$E_{\text{H-L}}$ = 0.73 eV

Fig. S67 Low-lying isomers of $Rh_7(CO)_{17}^+$ with relative energies corrected by zero-point vibrations. Also labeled, are symmetry, spin multiplicity (m) and HOMO-LUMO gap ($E_{\text{H-L}}$).

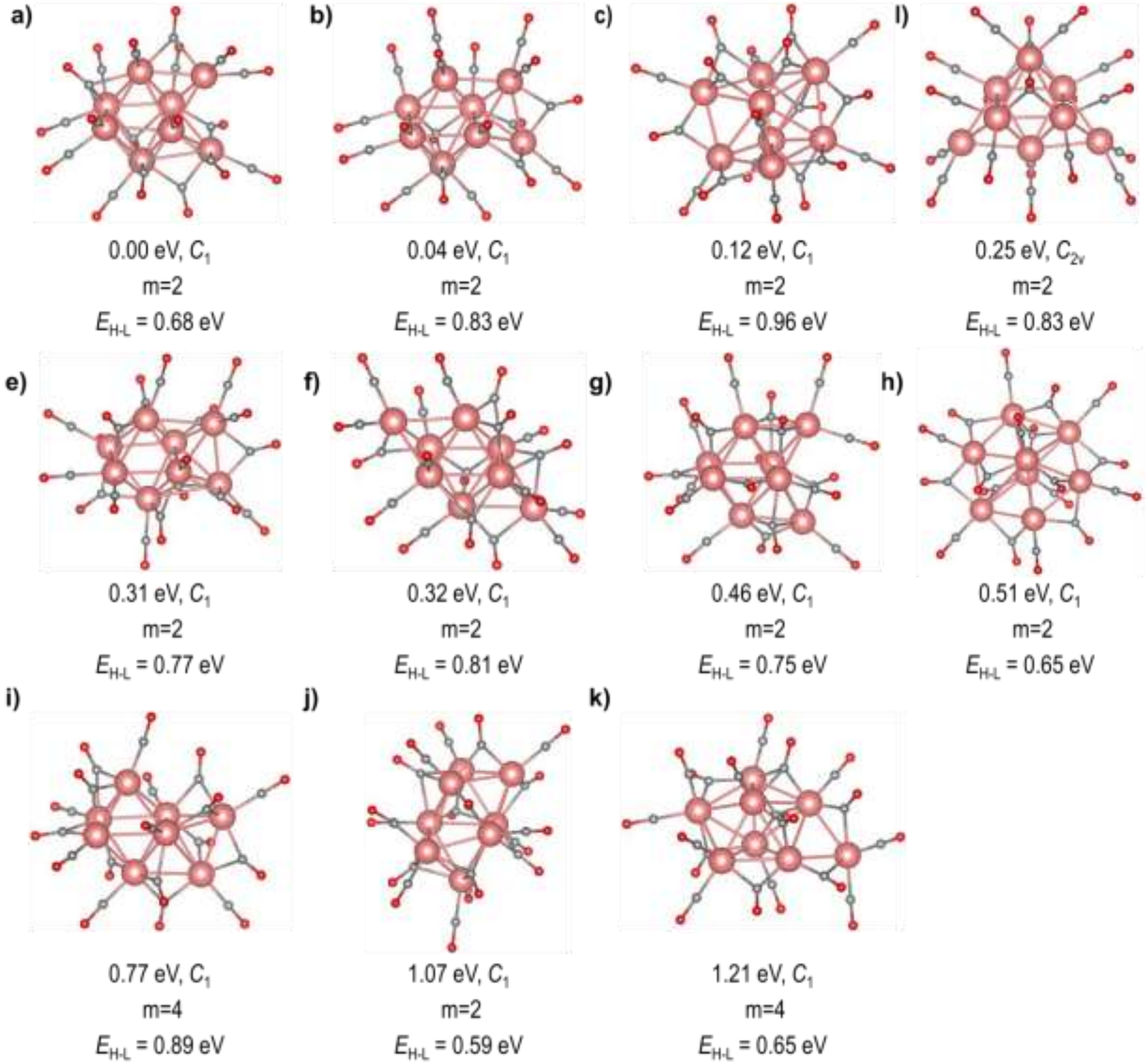

a) 0.00 eV, C_1 m=2 $E_{\text{H-L}}$ = 0.68 eV

b) 0.04 eV, C_1 m=2 $E_{\text{H-L}}$ = 0.83 eV

c) 0.12 eV, C_1 m=2 $E_{\text{H-L}}$ = 0.96 eV

l) 0.25 eV, C_{2v} m=2 $E_{\text{H-L}}$ = 0.83 eV

e) 0.31 eV, C_1 m=2 $E_{\text{H-L}}$ = 0.77 eV

f) 0.32 eV, C_1 m=2 $E_{\text{H-L}}$ = 0.81 eV

g) 0.46 eV, C_1 m=2 $E_{\text{H-L}}$ = 0.75 eV

h) 0.51 eV, C_1 m=2 $E_{\text{H-L}}$ = 0.65 eV

i) 0.77 eV, C_1 m=4 $E_{\text{H-L}}$ = 0.89 eV

j) 1.07 eV, C_1 m=2 $E_{\text{H-L}}$ = 0.59 eV

k) 1.21 eV, C_1 m=4 $E_{\text{H-L}}$ = 0.65 eV

Fig. S68 Low-lying isomers of $Rh_8(CO)_{18}^+$ with relative energies corrected by zero-point vibrations. Also labeled, are symmetry, spin multiplicity (m) and HOMO-LUMO gap ($E_{\text{H-L}}$).

S11. AdNDP analysis of $Rh_n(CO)_m^+$

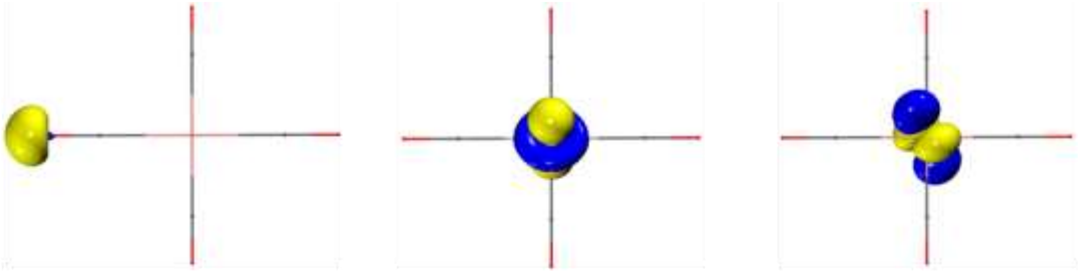

4 × O LPs (ON = 1.98)

d_{z^2} (ON = 1.97)

d_{yz} (ON = 1.82)

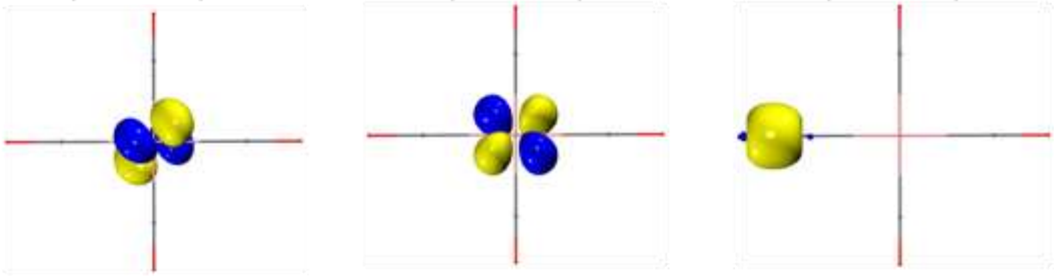

d_{xz} (ON = 1.82)

d_{xy} (ON = 1.75)

4 × 2c-2e C-O σ (ON = 2.00)

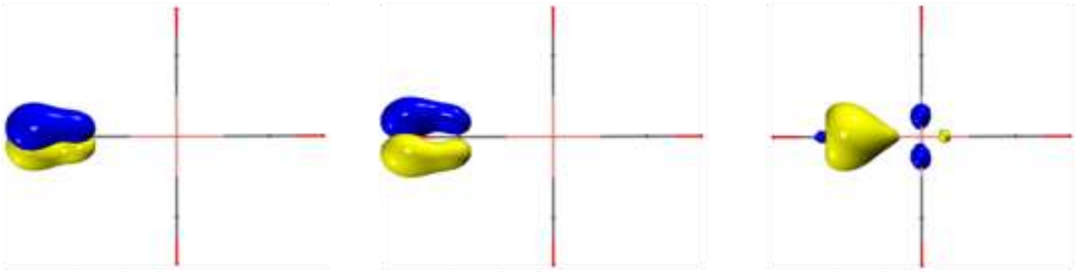

4 × 2c-2e C-O π (ON = 2.00)

4 × 2c-2e C-O π (ON = 1.99)

4 × 2c-2e Rh-C (ON = 1.98)

Fig. S69 AdNDP analysis of $Rh(CO)_4^+$. Only one of the same type of orbitals is given for clarity. ON denotes the occupancy number (|e|). The isovalues are set to 0.05 for all.

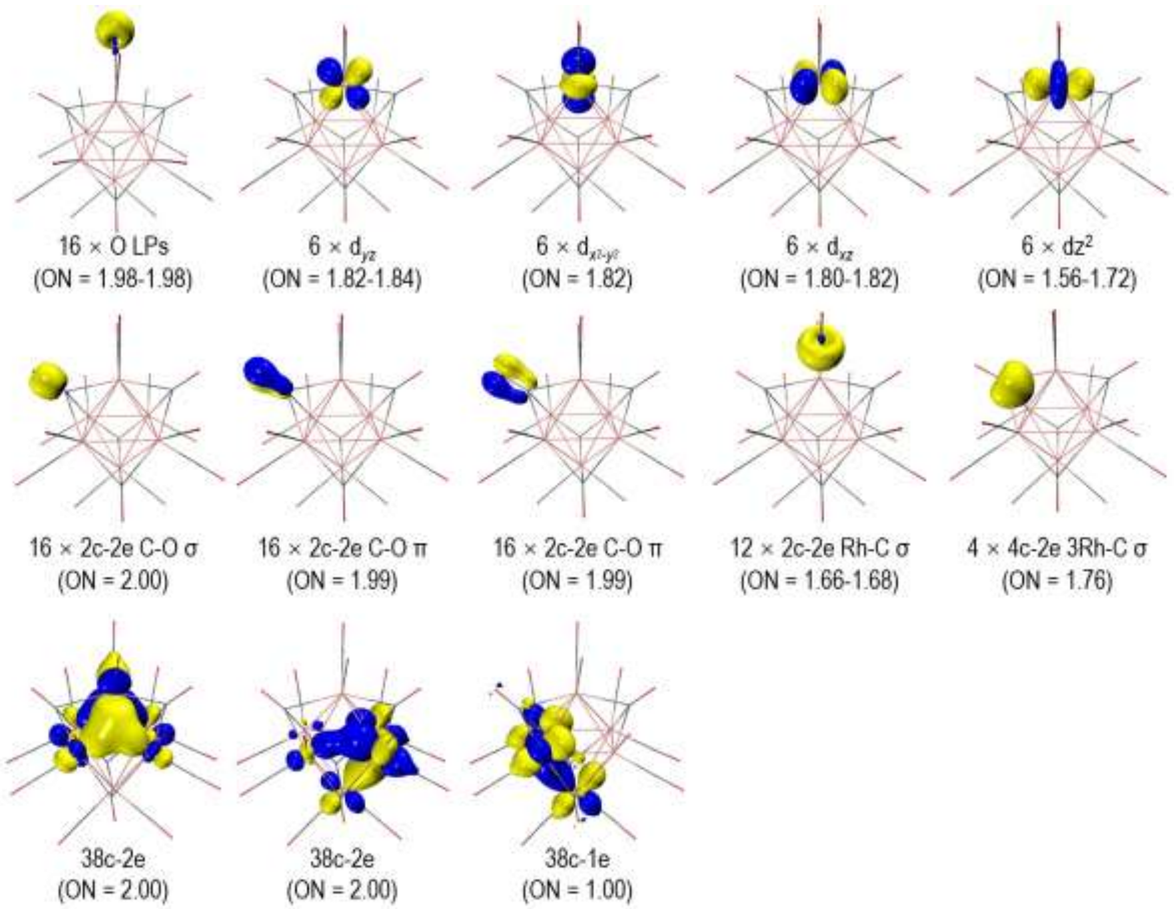

Fig. S70 AdNDP analysis of $Rh_6(CO)_{16}^+$. Only one of the same type of orbitals is given for clarity. ON denotes the occupancy number (|e|). The isovalues are set to 0.05 for all.

AdNDP analysis shows that the $Rh_6(CO)_{16}^+$ cluster exhibit electron delocalization across the whole metal center, showing a clear delocalized electron configuration indicative of superatom feature and aromaticity.

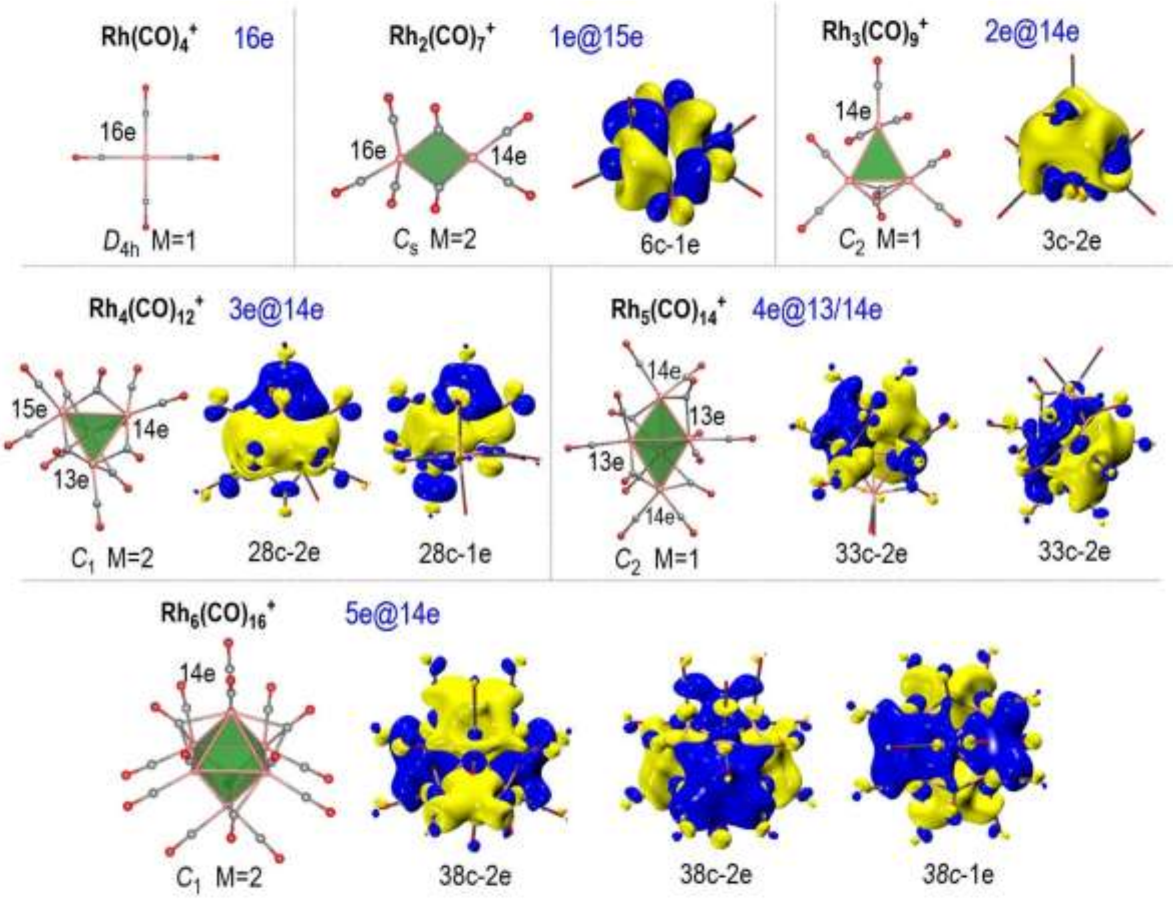

Fig. S71 Geometry and AdNDP analysis of $Rh_n(CO)_m^+$ (n = 1–6). Also labelled are symmetries, spin multiplicities (M), and the electron counting (xe@ne) according to the "$A\bar{a}$" rule which takes into account the itinerant electrons and the average number of localized electrons at surface atoms. The polyhedral patterns of the metallic cores are shown to guide eye. The isovalues for the patterns of AdNDP anayses are set to 0.02.

The AdNDP chemical bonding analysis of $Rh_n(CO)_m^+$ clusters elucidates the electronic distribution pertaining to typical CO coordination on the cluster, showing a triple bond (2 σ and 1 π) between each carbon and oxygen atoms, with each oxygen atom possessing a lone pair of electrons. Each Rh atom has four d-orbital lone pairs of electrons; each terminal CO ligand donates two electrons to the cluster through the establishment of a Rh–C bond, whereas each bridging CO ligand engages in a three-center two-electron (3c-2e) bond with two neighboring Rh atoms.

S12. A comparison of CO and NO complexes

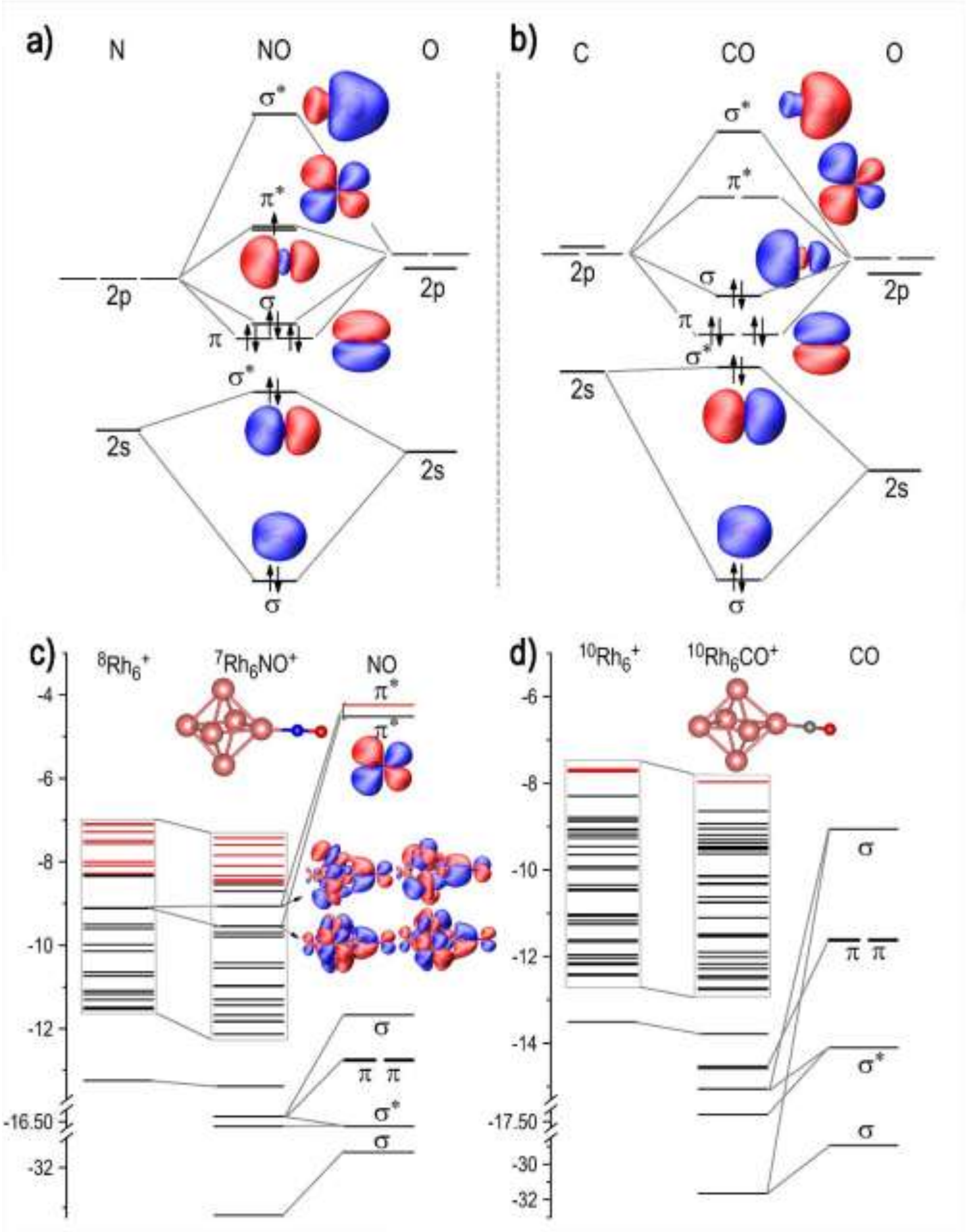

Fig. S72 CO vs. NO. A comparison of the DFT calculated frontier molecular orbitals of CO and NO, as well as the molecular orbital correlation in the Rh_6CO and Rh_6NO clusters.

As shown above, the NO molecule has a half-filled antibonding π* orbital, which differs from that of the CO molecule. Also, for the $Rh_n(CO)_m^+$ system, there is a difference in the bond order of CO as it transitions from μ_1 to μ_2 to μ_3, but the *d* band of Rh_6 core is retained.

The $Rh_6(CO)_{16}^+$ cluster exhibits an octahedral Rh_6 framework, giving rise to superatomic feature of electron delocalization. This is also associated with the inorganic aromaticity of such metal clusters.[17-19] Given this, we also conducted aromaticity analysis on Rh_6-related clusters as a representative case. Research into chemical bonding shows that the $Rh_6(CO)_{16}^+$ cluster has a total of 6 delocalized electrons, distributed across three orbitals. These orbitals are mainly formed by the combination of six d orbitals. This serves as an example of an octahedral aromatic molecule that is largely dominated by the d component.

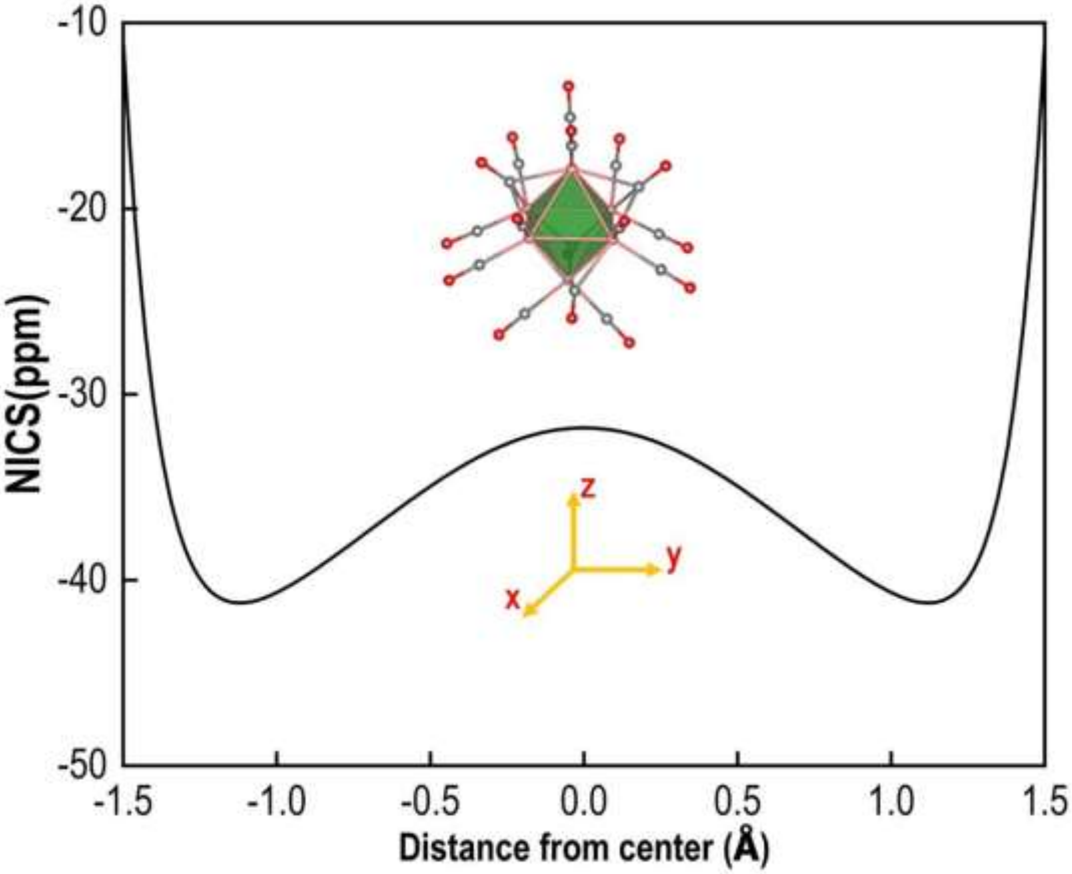

Fig. S73 NICS-scan curve for $Rh_6(CO)_{16}^+$ along the *z* axis (C_2 axis) within the range of -1.5−1.5 Å from the octahedron center. The geometric center is set as the zero point. The inset shows the ground-state structure.

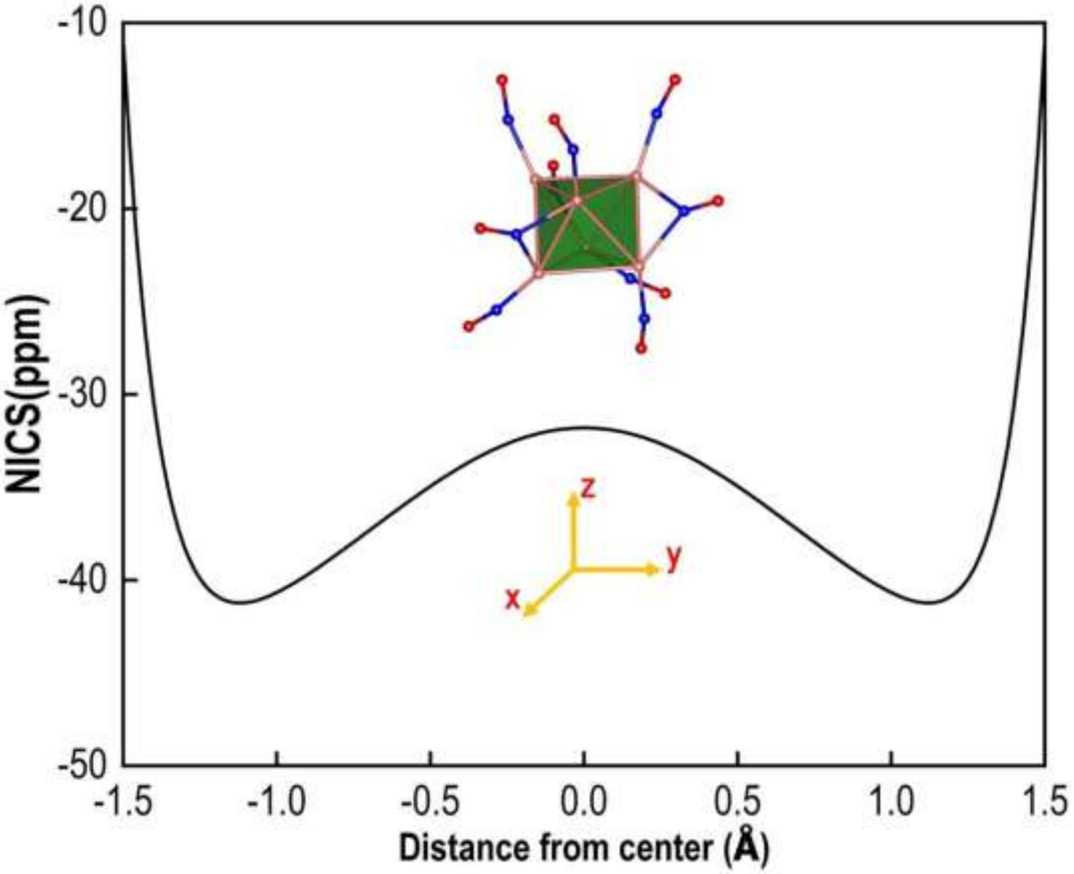

Fig. S74 NICS-scan curve for $Rh_6(CO)_{16}^+$ along the *z* axis (C_3 axis) within the range of -1.5−1.5 Å from the octahedron center. The geometric center is set as the zero point. The inset shows the ground-state structure.

Notably, $Rh_6(CO)_{16}^+$ and $Rh_6(NO)_9^+$ both exhibit an octahedral Rh_6 framework, giving rise to superatomic feature of electron delocalization.

Table S1. Mayer bond order of the $Rh_n(CO)_m^+$ clusters.

Cluster	μ_1-CO	μ_1-C-Rh	μ_2-C-O	μ_2-C-Rh	μ_3-CO	μ_3-C-Rh	Rh-Rh
$Rh(CO)_4^+$	2.48	1.00	--	--	--	--	--
$Rh_2(CO)_7^+$	2.42/2.43	1.00-1.05	2.23/2.26	0.61-0.81	--	--	0.26
$Rh_3(CO)_9^+$	2.22-2.39	1.02-1.10	2.22	0.69/0.82	--	--	0.36/0.43
$Rh_4(CO)_{12+}$	2.35-2.38	1.03-1.13	2.21-2.24	0.45-0.89	--	--	0.24-0.39
$Rh_5(CO)_{14+}$	2.32-2.35	1.13-1.19	2.18-2.20	0.63-0.79	--	--	0.29-0.45
$Rh_6(CO)_{16+}$	2.33-2.34	1.12-1.17	--	--	2.04-2.10	0.36-0.61	0.27-0.35

Note: In the $Rh_n(NO)_m^+$ system, there is also a significant difference in the bond order of NO as it transitions from μ_1 to μ_2 to μ_3, which in turn suggests that the type designation of NO is very facile, and the Rh-Rh reflects that the metalmetal bonding formed between Rh-Rh is not very strong. Compared to CO, the bond order of NO is smaller due to the presence of antibonding electrons on NO, which makes the NO triple bond weaker and the bond order between Rh-O, which are not adjacent to each other, is significantly non-zero, and in the formation of $Rh_n(NO)_m^+$ clusters, a part of this antibonding electrons form delocalized orbitals with π* features, and another part interacts with the delectrons of Rh, rendering increased N-Rh bonding orders.

Table S2. Mayer bond order of the $Rh_n(NO)_m^+$ clusters.

Cluster	μ_1-NO	μ_1-N-Rh	μ_2-NO	μ_2-N-Rh	μ_3-NO	μ_3-N-Rh	O-Rh	Rh-Rh
$Rh(NO)_3^+$	1.97	1.11	--	--	--	--	0.29	--
$Rh_2(NO)_5^+$	1.88/1.91	1.14/1.21	1.79	0.71	--	--	0.19-0.35	0.29
$Rh_3(NO)_6^+$	1.91	1.24	1.79	0.73	--	--	0.19-0.36	0.33
$Rh_4(NO)_8^+$	1.86	1.34	1.73	0.63/0.80	--	--	0.17-0.39	0.27/0.32
$Rh_5(NO)_9^+$	1.83-1.87	1.33-1.41	1.71-1.77	0.65-0.95	1.69	0.40-0.53	0.11-0.40	0.12-0.35
$Rh_6(NO)_9^+$	1.82-1.84	1.39/1.44	1.76	0.73-0.86	--	--	0.20-0.41	0.28-0.51

S13. Geometric structures of $Rh_n(CO)_m^-$

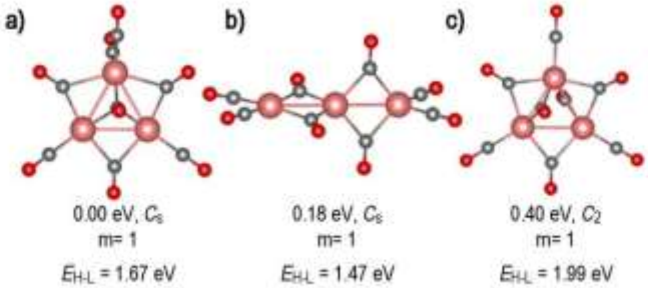

Fig. S75 Low-lying isomers of $Rh_3(CO)_8^-$ with relative energies corrected by zero-point vibrations. Also labeled, are symmetry, spin multiplicity (m) and HOMO-LUMO gap (E_{H-L}).

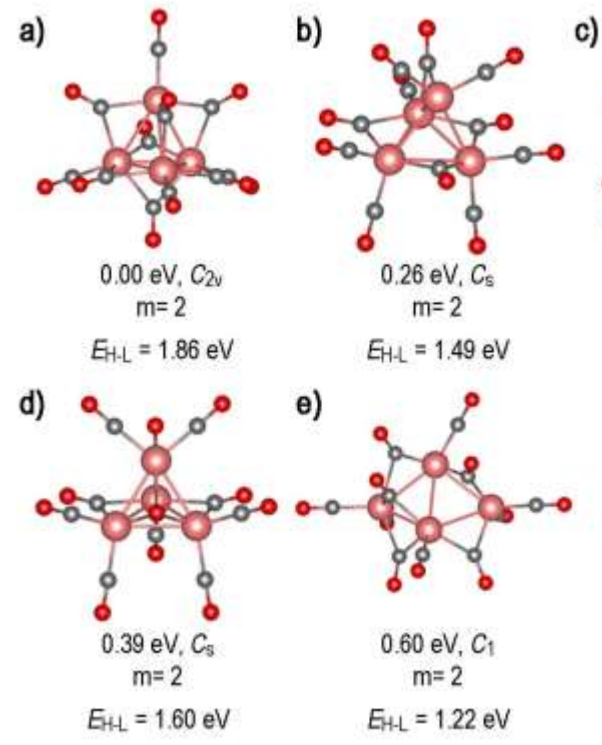

a) 0.00 eV, C_{2v}
m= 2
$E_{\text{H-L}}$ = 1.86 eV

b) 0.26 eV, C_s
m= 2
$E_{\text{H-L}}$ = 1.49 eV

c) 0.38 eV, C_{2v}
m= 2
$E_{\text{H-L}}$ = 1.61 eV

d) 0.39 eV, C_s
m= 2
$E_{\text{H-L}}$ = 1.60 eV

e) 0.60 eV, C_1
m= 2
$E_{\text{H-L}}$ = 1.22 eV

Fig. S76 Low-lying isomers of $Rh_4(CO)_{11}^-$ with relative energies corrected by zero-point vibrations. Also labeled, are symmetry, spin multiplicity (m) and HOMO-LUMO gap ($E_{\text{H-L}}$).

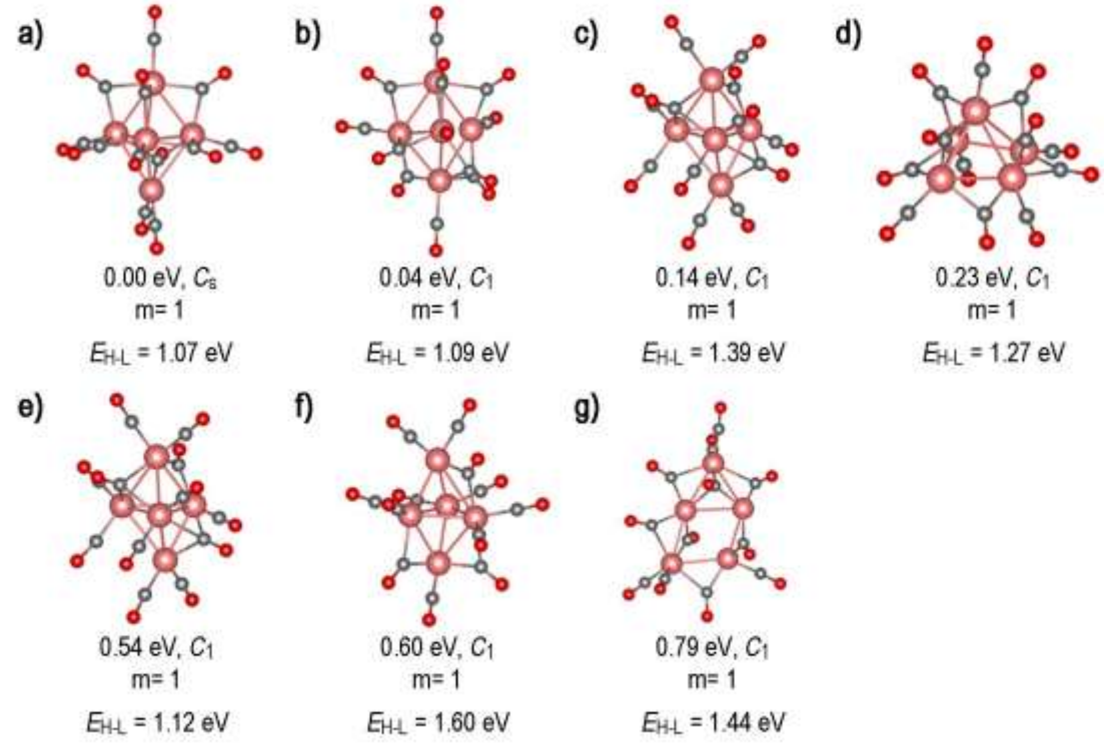

a) 0.00 eV, C_s
m= 1
$E_{\text{H-L}}$ = 1.07 eV

b) 0.04 eV, C_1
m= 1
$E_{\text{H-L}}$ = 1.09 eV

c) 0.14 eV, C_1
m= 1
$E_{\text{H-L}}$ = 1.39 eV

d) 0.23 eV, C_1
m= 1
$E_{\text{H-L}}$ = 1.27 eV

e) 0.54 eV, C_1
m= 1
$E_{\text{H-L}}$ = 1.12 eV

f) 0.60 eV, C_1
m= 1
$E_{\text{H-L}}$ = 1.60 eV

g) 0.79 eV, C_1
m= 1
$E_{\text{H-L}}$ = 1.44 eV

Fig. S77 Low-lying isomers of $Rh_5(CO)_{12}^-$ with relative energies corrected by zero-point vibrations. Also labeled, are symmetry, spin multiplicity (m) and HOMO-LUMO gap ($E_{\text{H-L}}$).

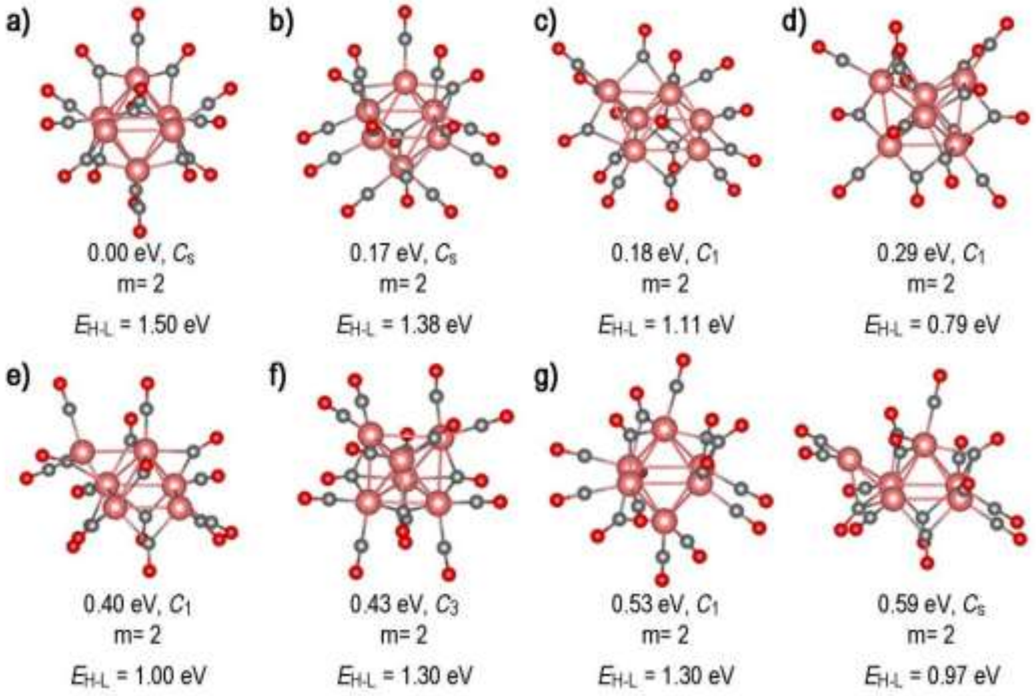

Fig. S78 Low-lying isomers of $Rh_6(CO)_{15}^-$ with relative energies corrected by zero-point vibrations. Also labeled, are symmetry, spin multiplicity (m) and HOMO-LUMO gap ($E_{H\text{-}L}$).

S14. AdNDP analysis of $Rh_n(CO)_m^-$

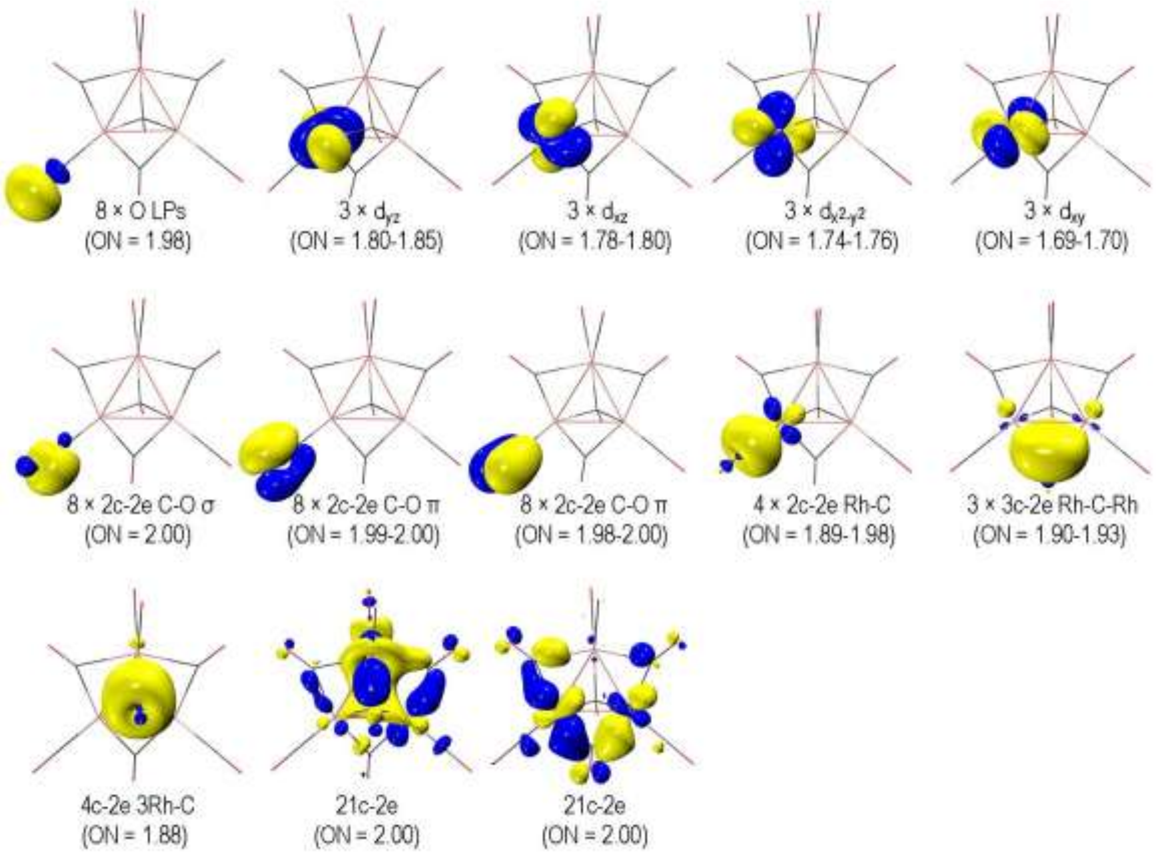

Fig. S79 AdNDP analysis of $Rh_3(CO)_8^-$. Only one of the same type of orbitals is given for clarity. ON denotes the occupancy number (|e|). The isovalues are set to 0.05 for all.

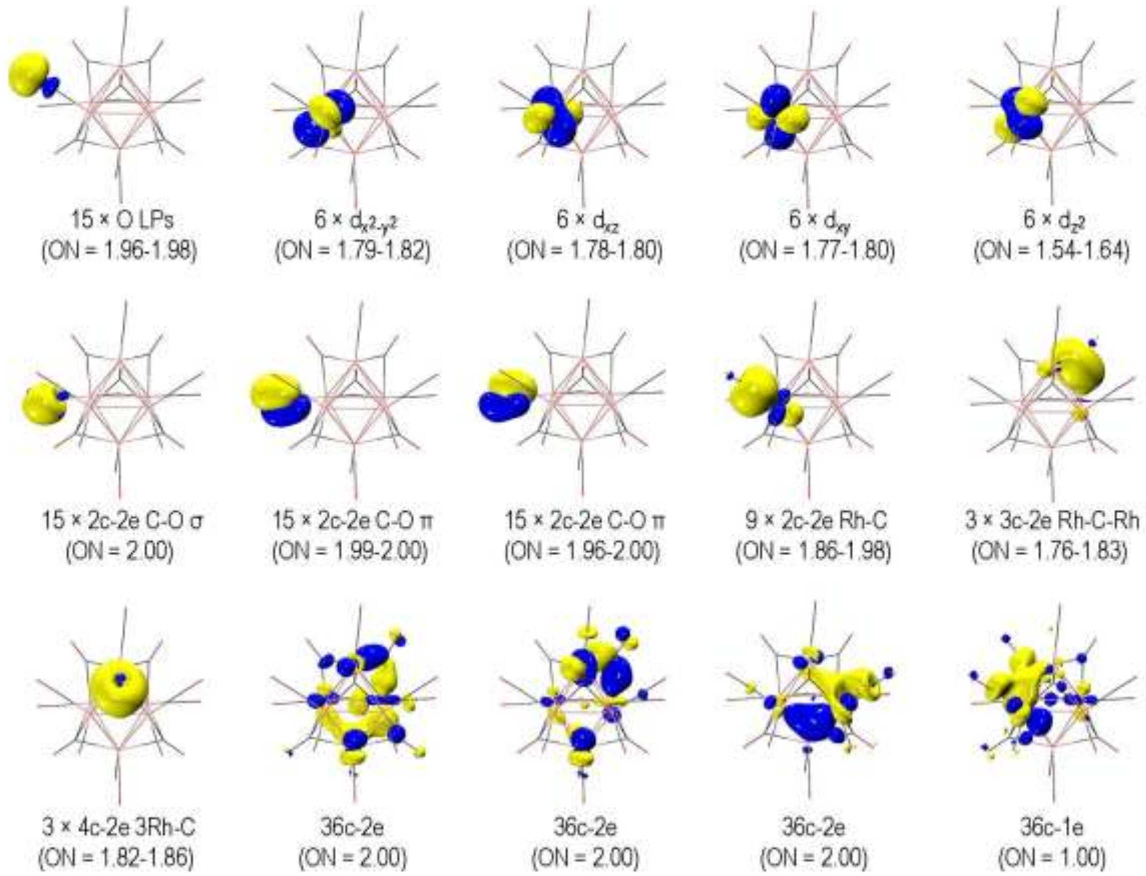

Fig. S80 AdNDP analysis of $Rh_6(CO)_{15}^-$. Only one of the same type of orbitals is given for clarity. ON denotes the occupancy number (|e|). The isovalues are set to 0.05 for all.

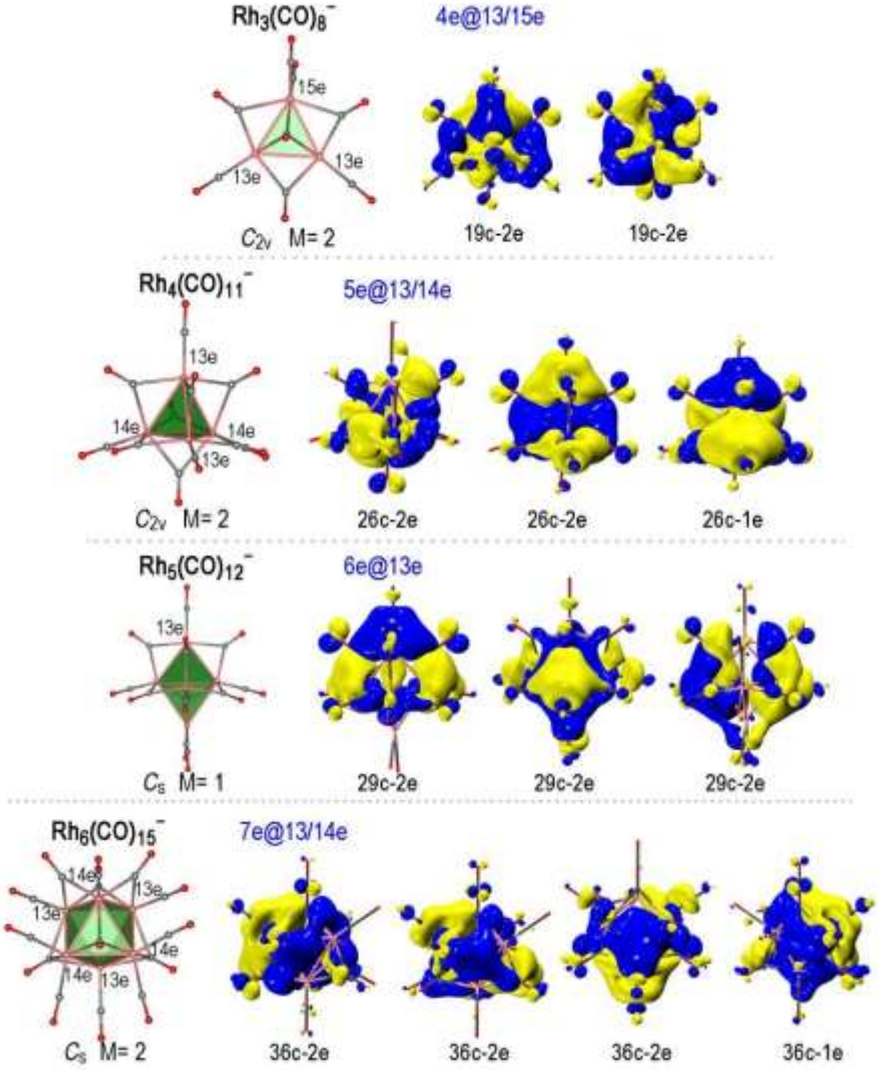

Fig. S81 Geometry and AdNDP analysis of $Rh_n(CO)_m^-$ (n = 3−6). Also labelled are symmetries, spin multiplicities (M), and the electron counting (xe@ne) according to the "*A*ā" rule which takes into account the itinerant electrons and the average number of localized electrons at surface atoms. The polyhedral patterns of the metallic cores are shown to guide eye. The isovalues for the patterns of AdNDP anayses are set to 0.02.

The AdNDP chemical bonding analysis of $Rh_n(CO)_m^-$ clusters elucidates the electronic distribution pertaining to typical CO coordination on the cluster, showing a triple bond (2 σ and 1 π) between each carbon and oxygen atoms, with each oxygen atom possessing a lone pair of electrons. Each Rh atom has four d-orbital lone pairs of electrons; each terminal CO ligand donates two electrons to the cluster through the establishment of a Rh–C bond, whereas each bridging CO ligand engages in a three-center two-electron (3c-2e) bond with two neighboring Rh atoms.

S15. DOS and molecular orbitals of typical $Rh_n(NO)_m^+$ and $Rh_n(CO)_m^+$

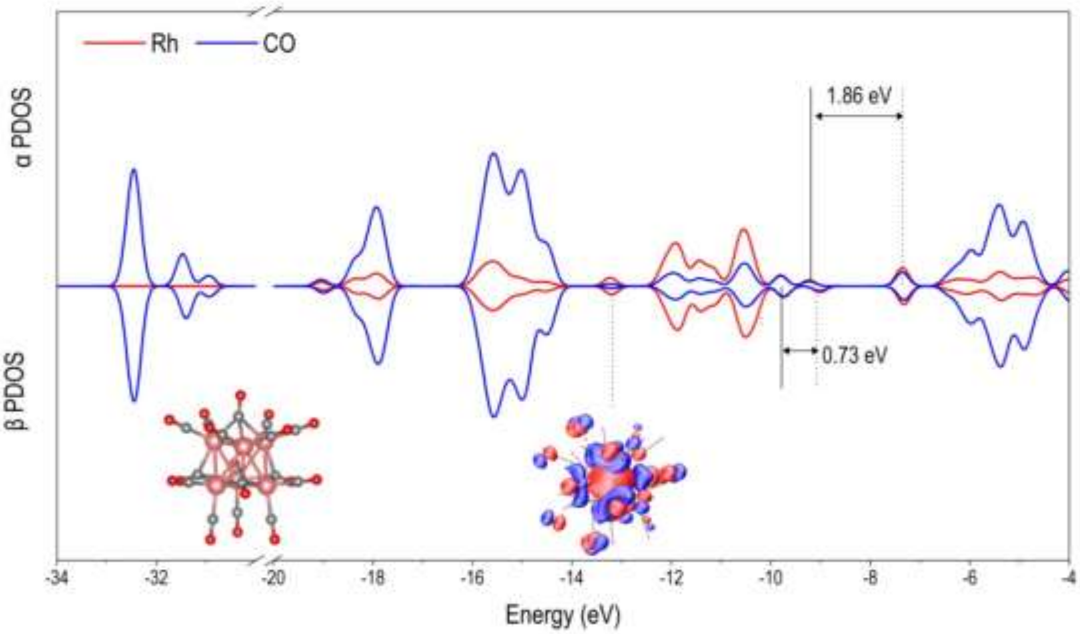

Fig. S82 Partial density of states and selected canonical molecular orbitals of $Rh_6(CO)_{16}^+$. The red and blue curves correspond to PDOS of Rh and CO respectively. The isovalues for orbitals are set to 0.02.

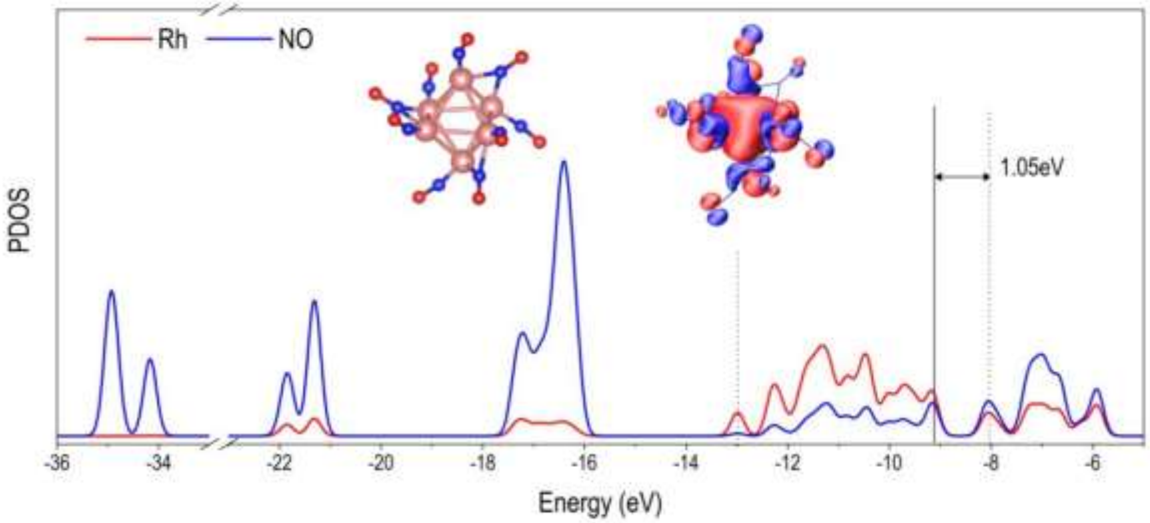

Fig. S83 Partial density of states and selected canonical molecular orbitals of $Rh_6(NO)_9^+$. The red and blue curves correspond to PDOS of Rh and CO respectively. The isovalues for orbitals are set to 0.02.

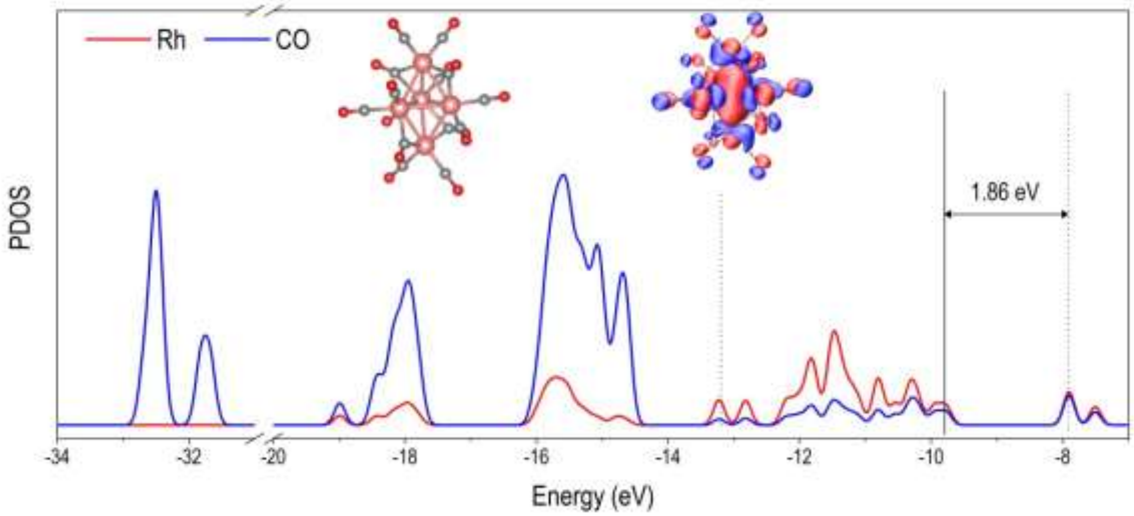

Fig. S84 Partial density of states and selected canonical molecular orbitals of $Rh_5(CO)_{14}^+$. The red and blue curves correspond to PDOS of Rh and CO respectively. The isovalues for orbitals are set to 0.02.

S16. Extending discussion of $Ru_n(CO)_m^+$

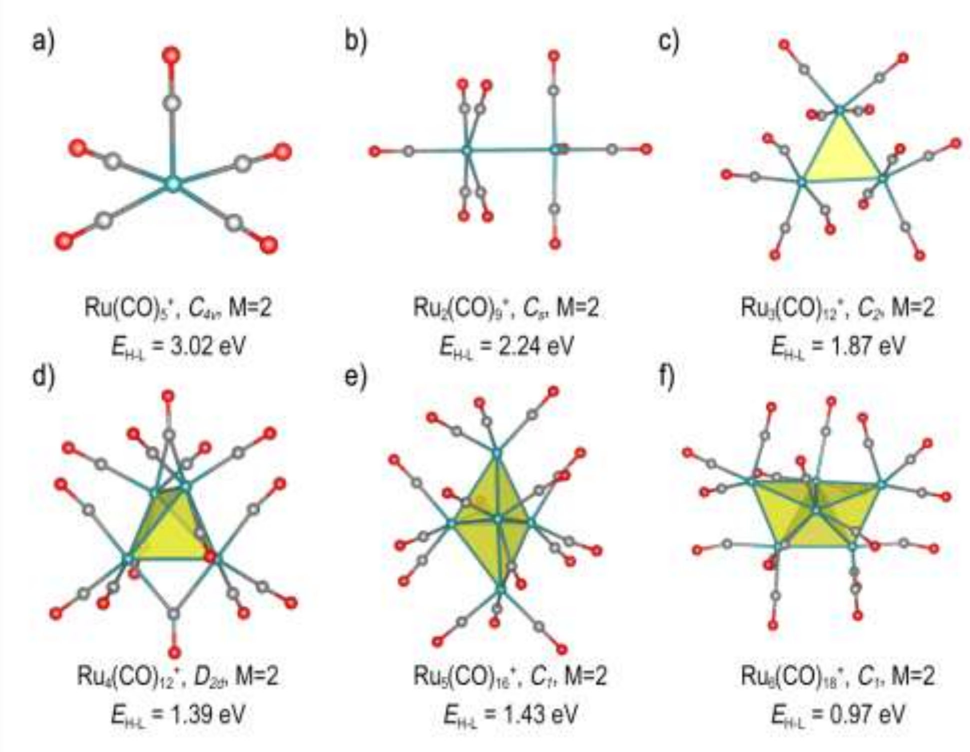

$Ru(CO)_5^+$, C_{4v}, M=2
E_{H-L} = 3.02 eV

$Ru_2(CO)_9^+$, C_s, M=2
E_{H-L} = 2.24 eV

$Ru_3(CO)_{12}^+$, C_2, M=2
E_{H-L} = 1.87 eV

$Ru_4(CO)_{12}^+$, D_{2d}, M=2
E_{H-L} = 1.39 eV

$Ru_5(CO)_{16}^+$, C_1, M=2
E_{H-L} = 1.43 eV

$Ru_6(CO)_{18}^+$, C_1, M=2
E_{H-L} = 0.97 eV

Fig. S85 Ground state of $Ru_n(CO)_m^+$ (n = 1–6), with energies corrected by zero-point vibrations. Also labeled are symmetries, spin multiplicities and E_{H-L} values. The stoichiometric formula referred to the previous findings .

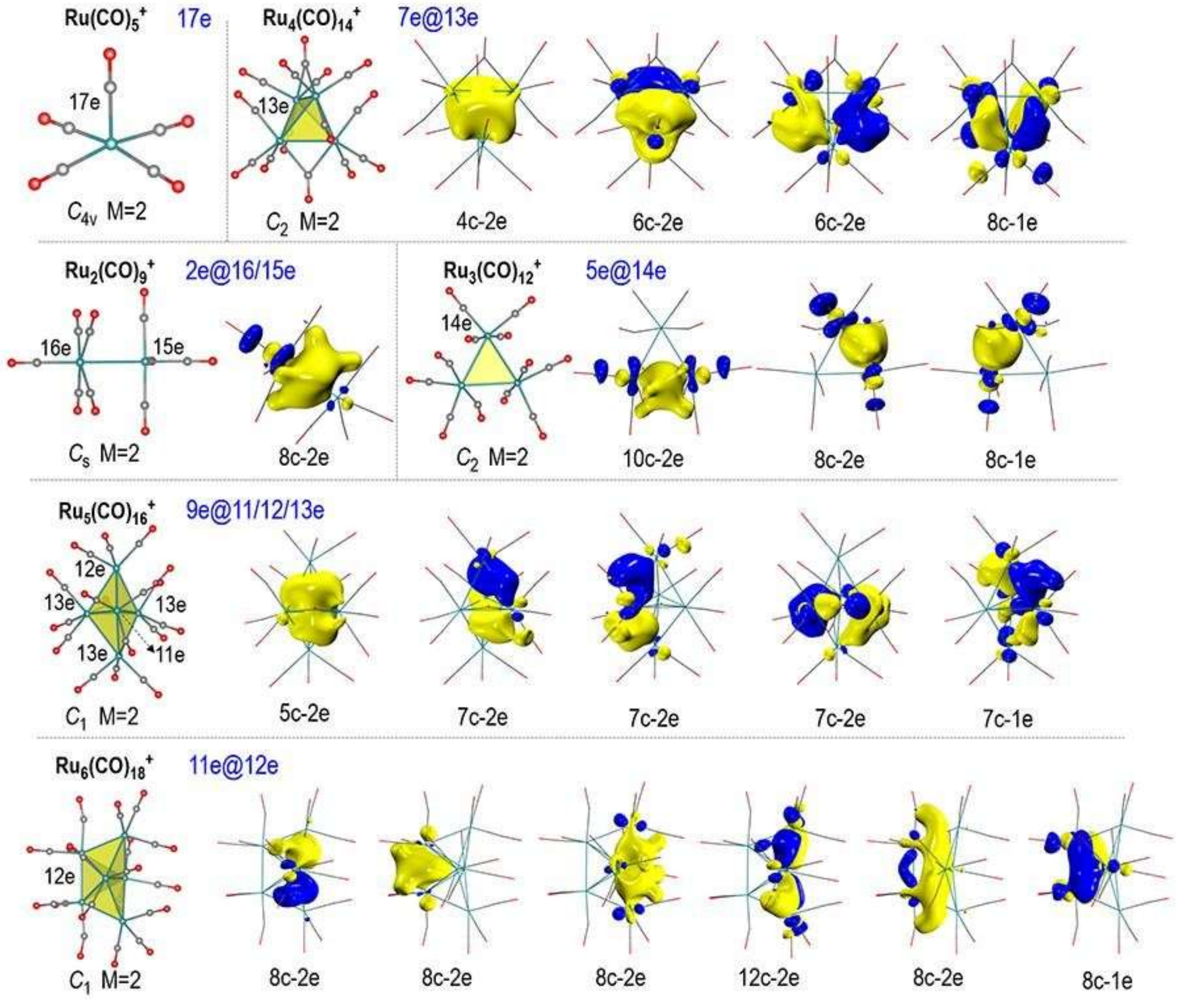

Fig. S86 AdNDP analysis of $Ru_n(CO)_m^+$ (n = 1−6). Only one of the same type of orbitals is given for clarity. ON denotes the occupancy number (|e|). The isovalues are set to 0.05 for all.

S17. Extending discussion of $Co_n(CO)_m^+$

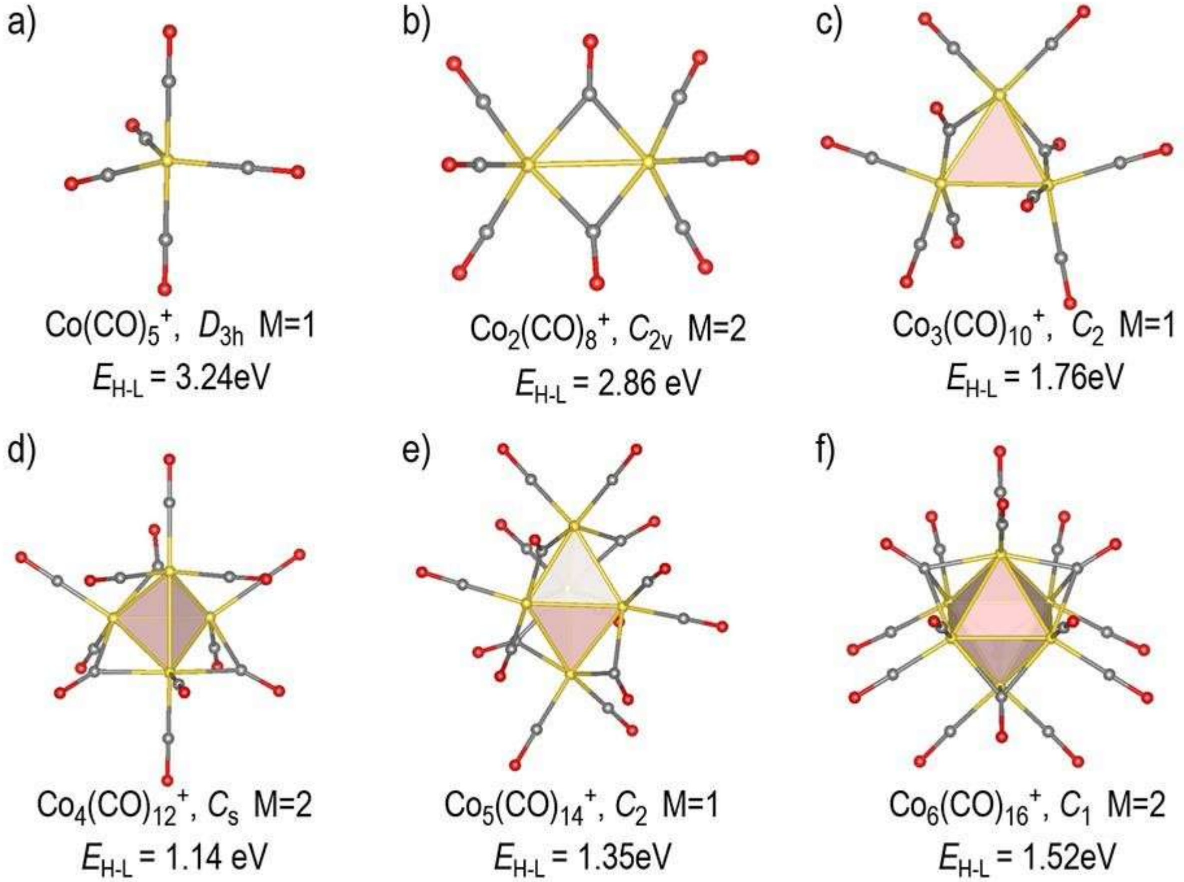

a) $Co(CO)_5^+$, D_{3h} M=1
$E_{H\text{-}L}$ = 3.24eV

b) $Co_2(CO)_8^+$, C_{2v} M=2
$E_{H\text{-}L}$ = 2.86 eV

c) $Co_3(CO)_{10}^+$, C_2 M=1
$E_{H\text{-}L}$ = 1.76eV

d) $Co_4(CO)_{12}^+$, C_s M=2
$E_{H\text{-}L}$ = 1.14 eV

e) $Co_5(CO)_{14}^+$, C_2 M=1
$E_{H\text{-}L}$ = 1.35eV

f) $Co_6(CO)_{16}^+$, C_1 M=2
$E_{H\text{-}L}$ = 1.52eV

Fig. S87 Ground-state structures of $Co_n(CO)_m^+$ (n = 1−6), with energies corrected by zero-point vibrations. Also labeled are symmetries, spin multiplicities and $E_{H\text{-}L}$ values. The stoichiometric formula referred to the previous findings.

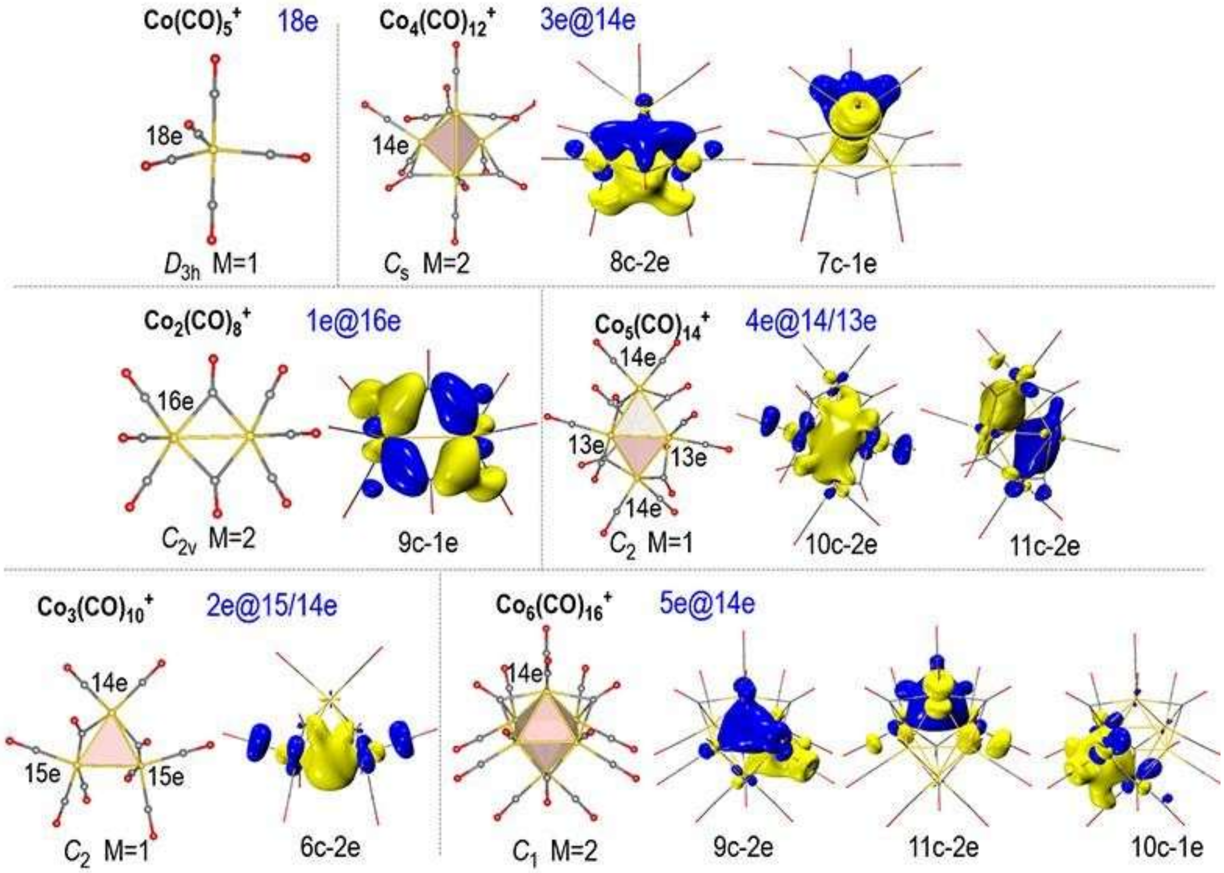

Fig. S88 AdNDP analysis of $Co_n(CO)_m^+$ (n = 1−6). Only one of the same type of orbitals is given for clarity. ON denotes the occupancy number (|e|). The isovalues are set to 0.05 for all.

S18. Extending discussion of $Fe_6C(CO)_{16}$

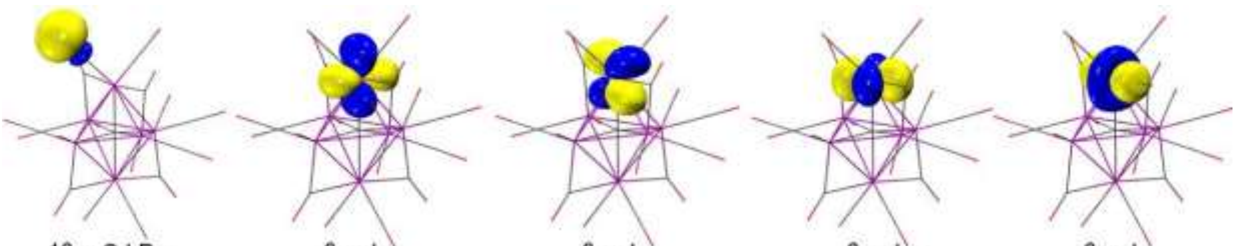

16 × O LPs (ON = 1.98)

6 × d_{xy} (ON = 1.73-1.76)

6 × d_{xz} (ON = 1.72-1.73)

6 × d_{yz} (ON = 1.60-1.71)

6 × d_{z^2} (ON = 1.49-1.50)

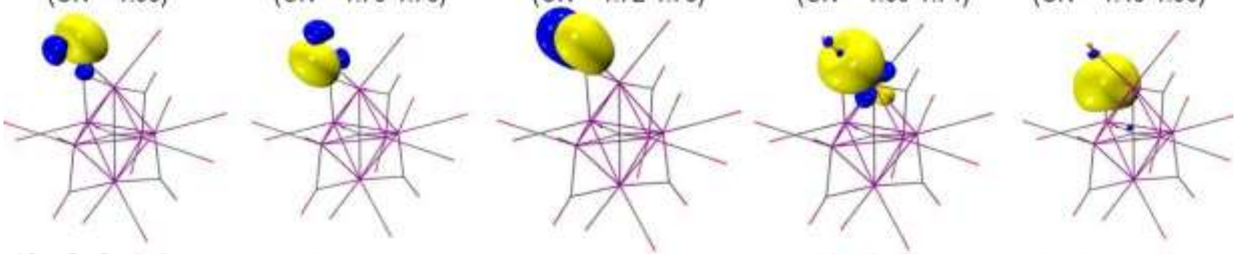

16 × 2c-2e C-O σ (ON = 2.00)

16 × 2c-2e C-O σ (ON = 1.99-2.00)

16 × 2c-2e C-O π (ON = 1.99-2.00)

12 × 2c-2e Fe-C (ON = 1.84-1.94)

4 × 3c-2e Fe-C-Fe (ON = 1.72)

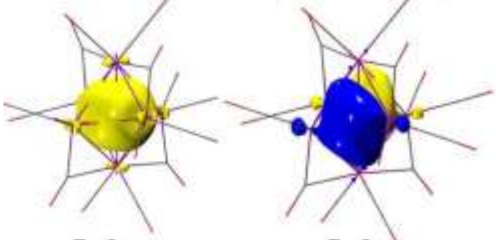

7c-2e (ON = 1.84)

7c-2e (ON = 1.63)

Fig. S89 AdNDP analysis of $Fe_6C(CO)_{16}$. The configuration of this cluster is referenced in the literature.[20] Only one of the same type of orbitals is given for clarity. ON denotes the occupancy number (|e|). The isovalues are set to 0.05 for all.

References

1. H. J. Zhai, B. Kiran, B. Dai, J. Li and L. S. Wang, *J. Am. Chem. Soc.*, 2005, **127**, 12098−12106.
2. H. J. Zhai and L. S. Wang, *J. Chem. Phys.*, 2005, **122**, 051101.
3. H.-J. Zhai, L.-L. Pan, B. Dai, B. Kiran, J. Li and L.-S. Wang, *J. Phys. Chem. C*, 2008, **112**, 11920−11928.
4. J. T. Lyon, P. Gruene, A. Fielicke, G. Meijer and D. M. Rayner, *J. Chem. Phys.*, 2009, **131**, 184706.
5. X. N. Wu, J. B. Ma, B. Xu, Y. X. Zhao, X. L. Ding and S. G. He, *J. Phys. Chem. A*, 2011, **115**, 5238−5246.
6. M. Mayer, M. Rohdenburg, S. Kawa, F. Horn, H. Knorke, C. Jenne, R. Tonner, K. R. Asmis and J. Warneke, *Chem. Eur. J.*, 2021, **27**, 10274−10281.
7. X. G. Zhang and P. B. Armentrout, *Organometallics*, 2001, **20**, 4266−4273.
8. C. Chi, J. Cui, Z. H. Li, X. Xing, G. Wang and M. Zhou, *Chem. Sci.*, 2012, **3**, 1698−1706.
9. G. Wang, J. Cui, C. Chi, X. Zhou, Z. H. Li, X. Xing and M. Zhou, *Chem. Sci.*, 2012, **3**, 3272−3279.
10. J. Cui, X. Zhou, G. Wang, C. Chi, Z. H. Li and M. Zhou, *J. Phys. Chem. A*, 2014, **118**, 2719−2727.

11. P. Ferrari, J. Vanbuel, N. M. Tam, M. T. Nguyen, S. Gewinner, W. Schollkopf, A. Fielicke and E. Janssens, *Chem. Eur. J.*, 2017, **23**, 4120−4127.
12. A. Fielicke, G. von Helden, G. Meijer, B. Simard, S. Dénommée and D. M. Rayner, *J. Am. Chem. Soc.*, 2003, **125**, 11184−11185.
13. A. Fielicke, G. von Helden, G. Meijer, D. B. Pedersen, B. Simard and D. M. Rayner, *J. Am. Chem. Soc.*, 2005, **127**, 8416−8423.
14. I. Swart, F. M. F. d. Groot, B. M. Weckhuysen, D. M. Rayner, G. Meijer and A. Fielicke, *J. Am. Chem. Soc.*, 2008, **130**, 2126−2127.
15. Q. Xu, S. Inoue, Y. Souma and H. Nakatani, *J. Organomet. Chem.*, 2000, **606**, 147−150.
16. M. L. Anderson, M. S. Ford, P. J. Derrick, T. Drewello, D. P. Woodruff and S. R. Mackenzie, *J. Phys. Chem. A*, 2006, **110**, 10992−11000.
17. Y.-H. Xu, W.-J. Tian, A. Muñoz-Castro, G. Frenking and Z.-M. Sun, *Science*, 2023, **382**, 840−843.
18. I. A. Popov, A. A. Starikova, D. V. Steglenko and A. I. Boldyrev, *Chem. Eur. J.*, 2018, **24**, 292−305.
19. A. I. Boldyrev and L.-S. Wang, *Chem. Rev.*, 2005, **105**, 3716−3757.
20. C. R. Cobb, R. K. Ngo, E. J. Dick, V. M. Lynch and M. J. Rose, *Chem. Sci.*, 2024, **15**, 11455−11471.